



DIPLOMARBEIT

Downcomer design in multistage fluidized bed systems

ausgeführt zum Zwecke der Erlangung des akademischen Grades eines
Diplom-Ingenieurs unter der Leitung von

Univ.Prof. Dipl.-Ing. Dr.techn. Hermann Hofbauer

und

Dipl.-Ing. Egon Zehetner

Dipl.-Ing. Dr.techn. Gerhard Schöny

E166

Institut für Verfahrenstechnik, Umwelttechnik und technische Biowissenschaften

eingereicht an der Technischen Universität Wien
Fakultät für Maschinenwesen und Betriebswissenschaften

von

Dominik Lovric

Matrikelnummer: 1125317

Ferdinand Raimundgasse 1a/6/5, 2000 Stockerau

Wien, am 18.06.2017

.....

Danksagung

An dieser Stelle möchte ich mich bei all denjenigen bedanken, die mich während meines Studiums sowie bei der Anfertigung dieser Arbeit unterstützt und motiviert haben.

Zuerst gebührt mein Dank Dr. Gerhard Schöny sowie allen Mitarbeitern der Arbeitsgruppe „Zero Emission Technologies“, für die hilfreichen Anregungen, die konstruktive Kritik bei der Erstellung dieser Arbeit und insbesondere für die gemeinsame Zeit.

Ein besonderer Dank gilt meinem Betreuer Dipl.-Ing. Egon Zehetner, für die hervorragende Betreuung und Unterstützung während der Anfertigung dieser Arbeit.

Des Weiteren bedanke ich mich bei allen Professoren, die mich während des gesamten Studiums gelehrt haben und mir meinen Bildungsweg ermöglicht haben.

Meiner gesamten Familie und all meinen Freunden, möchte ich für den loyalen Rückhalt in den letzten Jahren ebenfalls danken. Danke auch an Ilona und an ihre Familie, die mich stets unterstützt hat. Ihr habt es mir ermöglicht meinen Weg zu gehen.

Danke...

Abstract

In the past years the climate change resulting from the emission of greenhouse gases, especially CO₂, has become an omnipresent issue and also the risks of global warming for people, economies as well as the ecosystems across sector and regions. More and more measures are being defined and new technologies developed to counter this problem. Carbon capture and sequestration technologies (CCS) are seen as one of the key measures to counteract the ongoing climate change. For this reason, more and more scientists and universities worldwide are working on the development of CCS technologies, including the research group "Future Energy Technology" at the Vienna University of Technology. At the Institute of Chemical Engineering, TU Wien, a fully integrated temperature swing adsorption bench scale unit (TSA-BSU) for continuous capture of about 35 kg of CO₂ per day was designed, constructed and put into operation. It is based on a dual multistage fluidized bed system, whereby 5 stages were built on top of each other in the adsorber and the desorber column. After successful operation of the constructed bench scale unit, the feasibility of the proposed double loop multi-stage fluidized bed system via temperature swing adsorption was proved. The next planned step of the, is the process scale-up to pilot scale with the development of a pilot unit (PSU) for continuous capture of about 1000 kg of CO₂ per day. Therefore, a cold flow model study was conducted in order to de-risk and improve the reactor design from a fluid- dynamic point of view, especially, the downcomers in the adsorber column. The present work contributes partly to the elaboration of a suitable reactor design for the planned pilot unit. Overall scope of this work was to study the operability of different downcomer configurations within multi-stage fluidized bed columns by determination of the solid flux as a reference. These design variations included tests with internal and external (aerated) downcomers. These variations included the variation of the entrance height between the downcomer and lower stage, geometry of the downcomer as well as the applied area of several downcomers. Furthermore, experiments with external downcomers were carried out to investigate a possible application of them on the planned PSU.

The experimental campaign, carried out in the first half of 2016, is analyzed. In conclusion, the results of the experiments with internal downcomers can be expressed as follows. The maximum possible solid flux within the process changes in the following way relative to the mentioned operating parameters. Through reduction of the fluidization within the downcomer, an increase of the maximum possible solid flux is resulting. A higher entrance height between the downcomer and lower stage, results in a higher maximum possible solid flux. Through variation of the geometry with regard to the length and width, and thus reducing the wall friction effects, a higher maximum possible solid flux is reached. For external downcomers a higher solid flux was determined compared to internal ones. One aspects that should be considered, is the required aeration of external downcomer.

Comparing between the two different downcomer designs it is clear to see that choice of the used downcomer design leading to both, advantages and disadvantages. Which downcomer design is finally used in the PSU depends on many factors: costs, space requirements, handling and implementation. A recommended solution is the installation of internal downcomers in the desorber column and external downcomers in the adsorber column.

Zusammenfassung

Die steigende CO₂ - Konzentration in der Atmosphäre bleibt auch in Zukunft ein omnipräsentes Thema weltweit, die daraus resultierenden Gefahren für das Ökosystem somit auch. Um den Klimawandel entgegenzuwirken werden stetig neue alternative Technologien entwickelt. Carbon capture and sequestration (CCS) –Technologien werden als eine der Schlüsselmaßnahmen im Kampf gegen den Klimawandel angesehen. Diesbezüglich forschen immer mehr Wissenschaftler und Universitäten an CO₂- Abscheidungsprozessen, unter anderem auch die Forschungsgruppe „Future Energy Technology“ an der TU Wien. Die Forschungsgruppe entwickelte in der Vergangenheit ein Reaktordesign und eine voll-integrierte Laboranlage (bench scale unit/BSU) zur Abscheidung von 35 kg CO₂ /Tag aus Abgas, basierend auf einer Temperatur –Wechsel Adsorption. Die Adsorberkolonne der BSU wurde als mehrstufige Wirbelschicht mit 5 Stufen realisiert, welche übereinander angeordnet sind. Nach erfolgreicher Beendigung der Versuchskampagnen ist in weiterer Folge ein Scale up geplant, mit dem Ziel eine Pilotanlage zu entwerfen welche 1000 kg CO₂/ Tag abscheiden kann.

Um ein besseres Verständnis über den Betriebseigenschaften der Pilotanlage zu erhalten, wurde ein Kaltmodell der Pilotanlage an der Technischen Universität Wien entworfen und gebaut. Eine Vielzahl von Versuchen wurde an diesem Kaltmodell durchgeführt, um die Zusammenhänge zwischen den Downcomer und dem Materialfluss, bezogen auf die Downcomer-querschnittfläche, zu untersuchen. Diese Arbeit stellt die Ergebnisse der Versuche dieser Kaltmodellkampagne vor. Die Parameter, welche variiert wurden, sind unter anderem die Fluidisierung innerhalb der Downcomer, die Eintauchtiefe der Downcomer in das darunterliegende Wirbelschichtbett, sowie die Geometrie der Downcomer selbst. In weiterer Folge wurde neben internen Downcomer auch externe Downcomer untersucht. Aus der Versuchskampagne für interne Downcomer wurde geschlossen, dass bei einer Reduzierung des Gasflusses durch die Downcomer, höhere Materialflüsse, bei identer Downcomer-querschnittfläche, erreicht werden können. Durch Anpassung der Geometrie und der dadurch resultierenden Reduzierung der Wandreibungseffekte, konnten auch höhere Materialflüsse, bei identer Downcomer-querschnittfläche, erreicht werden.

Zuletzt, dass durch die Reduzierung der Eintauchtiefe der internen Downcomer, höhere Materialflüsse, bei identer Downcomer-querschnittfläche, erreicht werden können. Aus der Versuchskampagne für externe Downcomer wurde geschlossen, dass höhere Werte für den Materialfluss pro Strömungsfläche erreicht werden können als bei Versuchen mit internen Downcomer. Jedoch benötigen externe Downcomern eine zusätzliche Fluidisierung, was zu zusätzlichen Kosten bei der Implementierung in die Pilotanlage führen kann. Welches Design der Downcomern schlussendlich für die geplante Anlage verwendet wird, hängt von vielen Faktoren ab, wie beispielsweise: Kosten, Platzbedarf sowie der Handhabung im Prozess. Die Festlegung und Wahl der verwendeten Downcomer Design für die geplante Pilotanlage war nicht das Augenmerk dieser Arbeit. Eine empfehlenswerte Lösung wäre jedoch die Installation von externen Downcomern in der Adsorber-Kolonne, wobei interne Downcomern für die Desorber-Kolonne vorteilhaft wären.

Declaration of honor

I hereby confirm on my honor that I personally prepared the present master thesis and carried out myself the activities directly involved with it. I also confirm that I have used no resources other than those declared. All formulations and concepts adopted literally or in their essential content from printed, unprinted or Internet sources have been cited according to the rules for academic work and identified by means of footnotes, indices or other precise indications of source.

The support provided during the work, including significant assistance from my supervisor has been indicated in full. The academic work has not been submitted to any other examination authority. The work is submitted in printed and electronic form. I confirm that the content of the digital version is completely identical to that of the printed version.

I am aware that a false declaration will have legal consequences.

Vienna _____

Dominik Lovric, 1125317

Table of Contents

Danksagung	II
Abstract	III
Zusammenfassung	IV
Declaration of honor	VI
1. Introduction and motivation	- 1 -
1.1. Motivation.....	- 1 -
1.2. Introduction.....	- 5 -
1.3. Temperature swing adsorption- bench scale unit	- 9 -
1.4. Problem definition	- 12 -
1.4.1 Aim of this work	- 12 -
1.4.2 Organization.....	- 12 -
2. Theoretical background	- 13 -
2.1. Fundamentals of fluidized bed systems.....	- 13 -
2.2. Multistage fluidized bed systems.....	- 31 -
2.2.1. General aspect.....	- 31 -
2.2.2. Gas distributor designs	- 33 -
2.2.3. Downcomer designs.....	- 36 -
3. Methodology	- 39 -
3.1. Experimental setup	- 39 -
3.1.1. Cold flow model setup.....	- 41 -
3.1.2. Measuring equipment.....	- 45 -
3.2. Determination of the bed material properties.....	- 48 -
3.2.1. Characterization of the bed material	- 48 -
3.2.2. Determination of the minimum fluidization velocity – U_{mf}	- 49 -
3.2.3. Determination of the solid circulation rate	- 52 -
3.3. Experimental procedure	- 54 -
3.3.1. Cold flow model start up	- 54 -
3.3.2. Stable operation	- 56 -
3.3.3. Shut down.....	- 58 -

4. Results	- 59 -
4.1. Internal downcomer.....	- 59 -
4.2. External downcomer	- 69 -
5. Summary & conclusion.....	- 70 -
List of Figures	- 73 -
List of Tables.....	- 76 -
Notation	- 78 -
List of Abbreviations.....	- 78 -
List of Symbols.....	- 78 -
List of Greek symbols.....	- 79 -
List of Indices.....	- 79 -
References/ Bibliography	- 80 -
Appendix.....	- 85 -

" We are the first generation that can end poverty, and the last one that can take steps to avoid the worst impacts of climate change. With the adoption of a new development agenda, sustainable development goals and climate change agreement, we can set the world on course for a better future. This must be a time for global action. Future generations will judge us harshly if we fail to meet our obligation."

- **Ban Ki-moon, 8th Secretary-General of the United Nations (2015)**

1. Introduction and motivation

1.1. Motivation

In the past years the climate change resulting from the emission of greenhouse gases, especially CO_2 , has become an omnipresent issue. Already in 1990 the IPCC (Intergovernmental Panel on Climate Change) published, that globally the surface air temperature has increased by 0.3°C to 0.6°C over the last 100 years, whereby the five global-average warmest years being in the 1980s. Over the same period global sea level has increased by 10-20cm. *“These increases have not been smooth with time, nor uniform over the globe”* [30]. Despite the frightening warning, the temperature in Austria (Europe) has risen by 2.0°C since 1880, with half of the warming occurring from 1980 on and globally, the average temperature in the northern hemisphere has increased by about 0.85°C [3]. In *Figure 1.1.*, the globally observed surface temperature change can be seen.

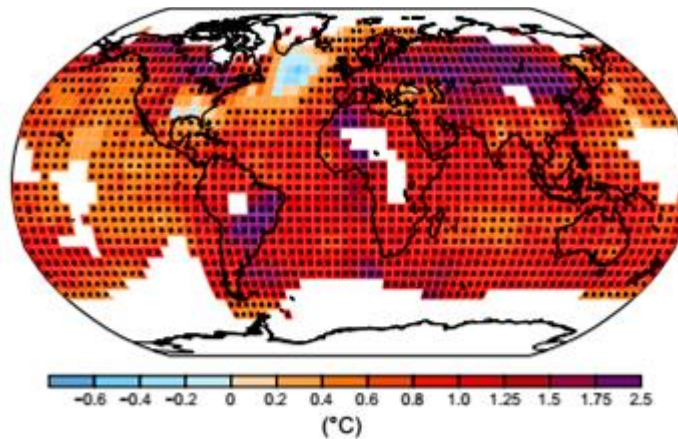


Figure 1.1. Map of the observed surface temperature change from 1901 to 2012 [33]

In nature, CO_2 is continuously exchanged between atmosphere, plants, and animals by photosynthesis, respiration and decomposition, as well as between the atmosphere and the ocean via gas exchange. A very small amount of CO_2 (about 1%) is also present in volcanic eruptions. The CO_2 emissions in 2012 were about 40% higher than in the 19th century. The bulk of this increase in CO_2 has occurred since 1970, when global energy consumption accelerated by the industrial revolution [50]. Since the industrial revolution, CO_2 emissions have steadily increased, making an important contribution to the greenhouse effect, as it has been known since the 19th century that the heat absorption capability of the atmosphere is strongly influenced by the concentration of greenhouse gases such as CO_2 . In *Figure 1.2.*, the so-called Keeling curve can be seen. The Keeling curve is a graph that represents the ongoing change in the concentration of carbon dioxide in the Earth's atmosphere since 1958 [8]. It is based on continuous measurements conducted at the Mauna Loa Observatory in Hawaii.

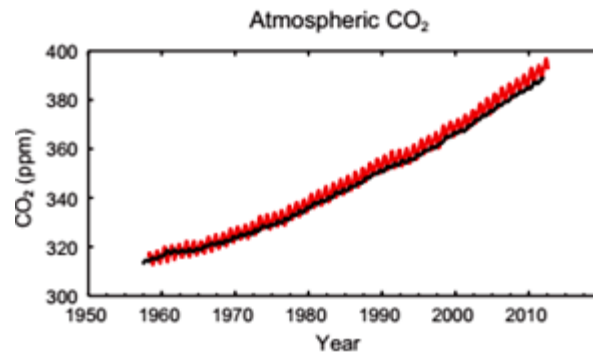


Figure 1.2. Atmospheric concentrations of carbon dioxide (CO₂) [33]

On 9th May 2013, for the first time, more than 400 parts per million of CO₂ were measured in the Earth's atmosphere, according to the US National Oceanic and Atmospheric Administration (NOAA) [56]. Considering the Keeling curve, and determines the linear increase one recognizes the drastic changes. While in the interval from 1960 to 1980 the gradient of increase was still 1.25, it is 2.33 during the interval of 2000-2015. The ascending trend of the gradient should already be an indicator that a rethink is necessary.

In the IPCC Special Report on Emission Scenarios future CO₂ emissions are predicted using six illustrative scenarios in which the global CO₂ emissions in 2020 are between 29 and 44 GtCO₂ and 23 to 84 GtCO₂ per year in 2050. It is projected that the number of CO₂ emission sources from the electricity and industrial sectors will increase significantly by 2050, especially in South and East Asia [31]. A study published in Science in the autumn of 2016 was able to establish a linear relationship between the CO₂ emitted and the melting-off of Arctic ice: "One ton of CO₂ is equal to minus 3 square meters of summer sea ice"[12]. At present (2016) humanity releases about 35 Gt of carbon dioxide annually. This would theoretically lead to a melting rate of 105000km² per year. In fact, the National Snow & Ice Data Center published: "Through 2016, the linear rate of decline for November is 55.400km² per year, or 5.0 percent per decade" [66].

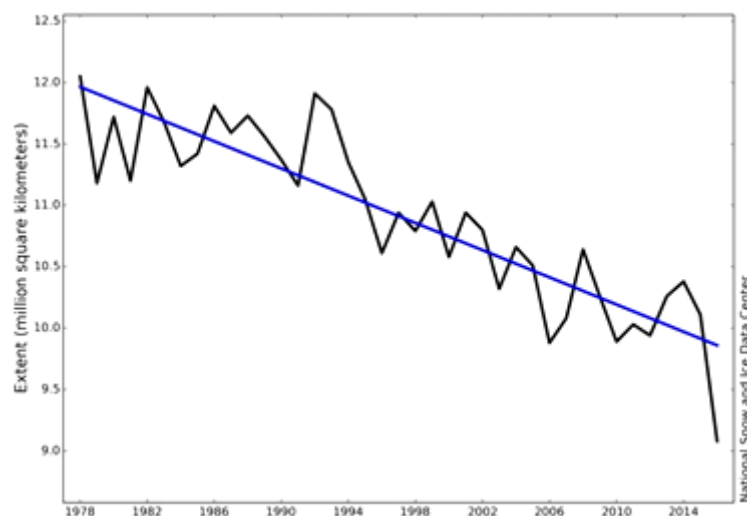


Figure 1.3. Average monthly Arctic sea ice extent from 1978-2016 [66]

Resulting consequences could be: Through loss of ice more heat is absorbed in the atmosphere, since sea ice reflects nearly 85% of the sunlight. Open water reflects just 7%, as it is darker. The melting ice adds freshwater to the ocean causing sea level to rise. However, the expansion of water by heating is the driving effect for the rise of the sea levels. Furthermore, another impact of ice melt could result in disruption of the ocean circulation with unimaginable consequences for living beings

Five Reasons for Concern (RFCs) have summarized the key risks of global warming for people, economies as well as the ecosystems across sector and regions. The RFC's provide a starting point for the evaluation of expected anthropological changes and impairment within the climate system. The five reasons are as follows [32]:

1. Unique and threatened systems:

Climate change is a genuine threat for many ecosystems and cultures, which are already highly exposed to climate change. The number of unique and threatened systems increases with an additional warming of +1°C. Already at an additional warming of 2°C, many systems with limited adaptability, especially those associated with Arctic sea ice and coral reefs, are highly at risk. In addition marine species are sensitive to these irregular temperature changes. Hence, an extinction of marine species is likely as well as a further sea level rise.

2. Extreme weather events:

Heat waves, heavy rainfall and droughts are already visible today. Further warming will result in an increase in the frequency of extreme climate events. With +1°C warming, the risks are high to lead to an extreme scenario.

3. Distribution of impacts:

There are major differences across regions and so risks are unevenly distributed between regions and people. Often, those in the weakest economic positions are at high risk compared to people in a stable economic situation. It is to be presumed that in Africa between 75 and 250 million people will be exposed to increased water scarcity and droughts and yields from agriculture may fall by up to 50%. Furthermore, in Latin America the number of people at risk of hunger will increase, through the extinction of species and loss of biodiversity. In addition, there is also the fact that water available for human consumption and agriculture is likely to be affected. Certain areas worldwide, particularly coastal areas in Asia will be at a high risk from increased flooding [7].

4. Global aggregate impacts:

Under additional warming between 1°C and 2°C, the risk of global aggregate impacts will rise. The economical costs of impacts of increased warming are projected to increase over time, as well as the previously mentioned loss of biodiversity leading to an associated loss of ecosystem goods.

5. Large-scale singular events:

With uncontrolled increasing warming, physical and ecological systems are threatened. Irreversible changes are the result. The risk is already present, since warm-water coral reefs as well as Arctic ecosystems already show irreversible changes. The risk of additional contributions to the sea level rise from Greenland and the Antarctic ice sheets can be greater than projected by the various ice sheet models. The complete loss of Greenland ice sheet could possibly contribute up to 7 m global sea level rise.

In order to keep the average warming at a maximum of 1.5 ° C, within the levels defined by the Paris Climate Convention of 2015, according to the calculations of the World Climate Council IPCC, "negative emissions" – i.e the withdrawal of CO₂ from the atmosphere- are necessary [27]. For this reason, the interest in global CO₂ reduction is increasing. More and more measures are being defined and new technologies developed to counter this problem. As an example, only the subject of *carbon capture and sequestration*, or also known as *carbon capture and storage* (CCS), is briefly explained in this portfolio.

If CO₂ emissions are interrupted completely, it would take many thousands of years for atmospheric CO₂ to return to "preindustrial" levels due to its very slow transmission into the deep ocean and the final burial in ocean sediments [50]. Although some sources clearly demonstrate that it is a long process, it is the responsibility of humans to stop climate change or at least counteract it. There has been great criticism of climate change research recently, through media, politicians and governments. But should we take risks and stand idly or see it as our obligation to set the world on course for a better future?

1.2. Introduction

Carbon capture and storage

CCS involves the use of technology, first to collect and concentrate the CO_2 produced in industrial and energy related sources, transports it to a suitable storage location, and then stores it away from the atmosphere for a long period of time. The capture step involves separating CO_2 from other gaseous products. The emissions, in form of CO_2 are captured before, during or after combustion processes [41].

CCS would most likely be applied to large point sources of CO_2 , such as power plants or large industrial processes. The use of CCS on biomass energy sources could lead to the separation of CO_2 from the atmosphere, often referred to as "negative emissions" since biomass is known as a CO_2 neutral combustible. As shown in *Figure 1.4*, there are currently three different methods of carbon capture processes which allow the separation of carbon dioxide from gases produced in electricity generation and industrial processes. The commonly used methods are: Oxyfuel, pre-combustion and post-combustion. The fourth mentioned method, industrial process, covers all methods that are not among the main methods and relates in this case to the steel production.

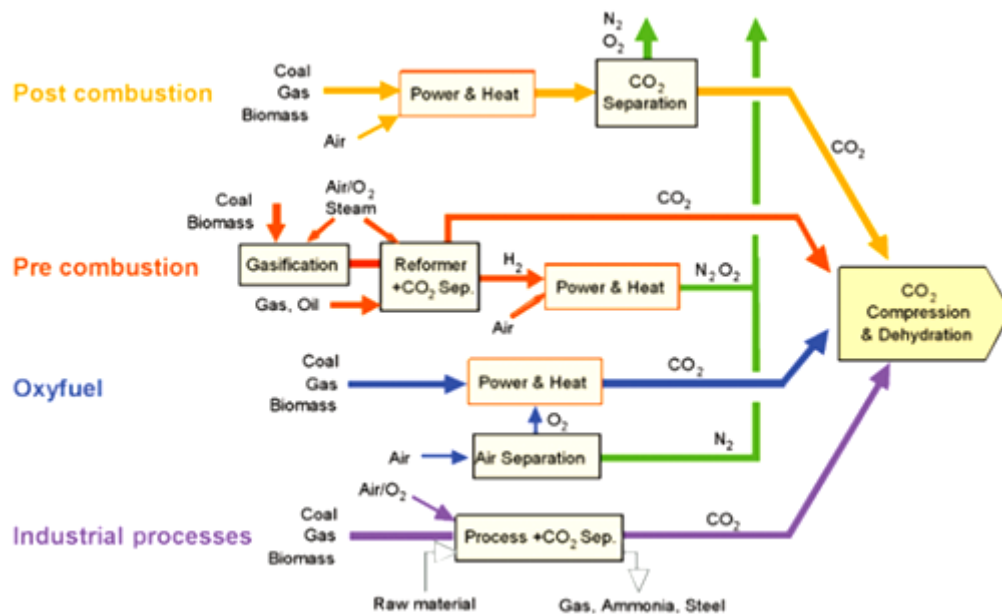


Figure 1.4. CO_2 Capture Systems – flowsheet [31]

In the *pre-combustion* process, a fuel/combustible is first gasified by a gasification agent to produce syngas gas. In this case, the fossil fuel is partially oxidized, for instance in a gasifier. The resulting syngas (CO and H_2) is shifted into CO_2 and H_2 . After the shift reactor, the CO_2 concentration is relatively high, which allows for CO_2 capture with relatively low effort from this stream. The H_2 can now be used as fuel for example in a gas turbine [31].

In **oxyfuel and chemical looping combustion** the combustible is burned in a reducing atmosphere instead of air. This oxygen-rich, nitrogen-free atmosphere results in final flue-gases consisting mainly of CO₂ and H₂O (water), the latter of which is condensed by cooling, thereby producing a more concentrated CO₂ stream for easier purification. The almost pure carbon dioxide stream can be transported to the sequestration site and stored. The technique is promising, due the fact of the purity of the flue gas but it cannot be left out of account, that the initial air separation step of oxygen from air, to a purity of 95-99% O₂, demands energy. Oxygen-fueled combustion processes are sometimes referred to as "zero emission" cycles, because the stored CO₂ is not a fraction removed from the flue gas stream (as in pre-combustion and post-combustion), but rather the flue gas stream itself [31].

Post combustion capture is an often used technique in research because existing fossil fuel power plants can be retrofitted to include CCS technology in this configuration. In post-combustion processes the CO₂ is removed after combustion of the fossil fuel. The flue-gas resulting from the combustion of fossil fuels mainly consists of N₂, CO₂, H₂O, O₂. The emitted carbon dioxide can be captured, after pretreatment by means of elimination of SO_x and NO_x, from the exhaust of a combustion process by absorbing it in a suitable solvent (gaseous, liquid or solid). The absorbed CO₂ is released from the solvent and compressed for transport and storage. Various CO₂ capture technologies have been proposed in the past but chemical absorption and adsorption are currently believed to be the suitable ones for power plants [9]. The methods used for CO₂ separation include: absorption as well as adsorption/desorption processes, high pressure membrane separation processes and cryogenic separation [28]. Below the commonly used three methods are mentioned.

Membrane Process

In this method the decisive factor is the selectivity of the membrane used. The carbon dioxide that needs to be transported must first be dissolved in the membrane (solution-diffusion model) before it can permeate through. Depending on the selectivity of the membrane, multiple membrane stages may be needed in order to obtain sufficiently high CO₂ purity. In some cases, chemical reagents are also added to the membrane, which react selectively with CO₂ in order to increase the selectivity of the membrane for CO₂. CO₂ diffuses through a membrane only when its partial pressure on one side of the membrane is higher than the other. Thus, the operating costs are given by the energy demand of the compressor used to induce a pressure difference across the membrane [18].

Chemical Absorption Process

Separation of CO₂ by chemical absorption is a well-known technology, and the basic process had already been patented in 1930 [6]. A typical chemical absorption process consists of an absorber and a stripper in which the solvent is thermally regenerated. In a chemical absorption process, the flue gas containing CO₂ enters a packed bed absorber, typically filled with packings, from the bottom and contacts counter-currently with a CO₂-lean solvent. The packaging material must allow a large specific surface with lowest possible flow resistance in order to minimize the pressure drop and the corresponding power requirement of the gas blower. After absorption, the solvent flows into a stripper for thermal regeneration and the CO₂ released from the stripper is compressed for the subsequent transportation. Solvent regeneration is typically conducted at 100-140 ° C and marginally above atmospheric pressure [10].

This technology has several disadvantages including a low CO₂ loading capacity and a high equipment corrosion rate [9]. Usually alkanolamines are used as the solvent. These alkanolamines could be primary, secondary, tertiary amines consisting of at least one OH and an amine group, for example, monoethanolamine (MEA), diethanolamine (DEA) and N-methyldiethanolamine (MDEA) [9].

Adsorption Process

Due to the fact that aqueous amine absorption processes boast some disadvantages, for example, low CO₂ capacity because of the low contact area between absorbent and flue gas, the solid adsorption process could be an alternative worth considering for CO₂ capture [9].

Adsorption is the adhesion of atoms, ions, or molecules from a gas, liquid, or dissolved solid to a surface. The basis of chemisorptions is a chemical reaction, where the adsorptive chemically reacts with the solid's surface, whereas in physisorption van-der-Waals forces or dipole-dipole interactions act between the adsorbate and the adsorbent surface. Adsorption processes are usually cyclic processes, in which adsorption and desorption of used material alternate periodically.

The adsorption equilibrium is given by specific operating conditions like composition, temperature and pressure [14]. Hence, through variation of one of these parameter the adsorption and desorption is possible.

Temperature swing adsorption (TSA) is a process for separating gas mixtures, using thermal energy by means of adsorption, and is mainly used for flue gas purification. The TSA process makes use of the temperature dependence of the adsorption as shown in *Figure 1.5*. (Whereby q is the number of occupied adsorption sites). The adsorbent is loaded with the adsorbate and it is largely freed from the adsorbate in a subsequent step via the supply of thermal energy. This step is called

desorption. Therefore, for the continuous operation of a temperature swing adsorption system, at least two columns are necessary (Adsorber/desorber column), whereby for batch operation a single column is sufficient. As a heating agent for desorption, steam or a preheated inert gas can be used [57].

If the regeneration is performed by reducing the pressure of the system, the process is referred to as pressure swing adsorption (PSA). The pressure of the system switch between high pressure in the adsorption step and low pressure during the regeneration step. Through reduction of the pressure the regeneration of the adsorbent is resulting by desorption of loaded adsorbent in the column. PSA is known as the “heatless” process and was patented after the TSA, in 1932 [14].

In contrast to pressure swing adsorption, the temperature swing adsorption requires thermal energy, which is less cost-intensive than mechanical energy.

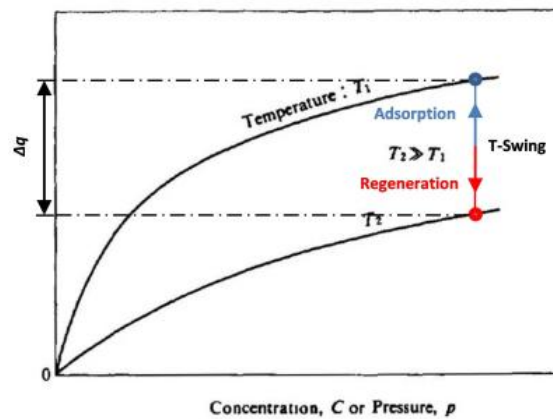


Figure 1.5. Example for temperature swing adsorption [57]

The commonly used adsorbents are carbonaceous adsorbents and zeolites. Furthermore, metalorganic frameworks, or so-called MOFs can be used. Although carbonaceous adsorbents such as activated carbon [47] are widespread due to their broad availability, low cost, high thermal stability, their range of application is limited due to the nonpolar characteristics. The adsorption efficiency of zeolites is largely influenced by their size, charge density, and chemical composition of the cations in their porous structures [61]. In recent years, metalorganic frameworks (MOF) have attracted great interest due to their high surface area, pore structures, and controllable pore surface characteristics, which can be adjusted by altering the metal clusters or the organic ligands [9].

Many studies have been developed to improve the selectivity and CO₂ adsorption capacity, through chemical modification of the surface of solids. Of particular interest are the basic organic group (amine) and inorganic metal oxide [9]. Amine-based adsorbents have as advantage a lower heat requirement for the regeneration compared to aqueous amines due to the low heat capacity

of solids used. As disadvantages high cost should be noted. Wang et al., proposed following approaches for an improvement of amine-based adsorbents: a high amine loading of the carrier material, an application of amines with higher nitrogen content and more effective methods for the amine introduction on the sorbent material [61].

The amine-based adsorbents can be differentiated as amine-impregnated and amine-grafted materials [9]. Since the amount of amine on a carrier material depends on the surface, amine-grafted leads often to a lower amine loading compared to amine-impregnated ones. However, amine-grafted adsorbents show a higher stability in process and a higher adsorption rate of CO₂ although the amine loading is higher in impregnated ones. Through the impregnation, also a larger diffusion resistance occurs [34].

As already mentioned, the adsorption equilibrium is given by specific operating conditions like the composition, temperature and pressure and through variation of these parameters a continuous adsorption process can be accomplished. The adsorption of CO₂ by temperature swing adsorption using solid adsorption materials has been proposed as a promising alternative to amine scrubbing technologies.

1.3. Temperature swing adsorption- bench scale unit

At the institute of chemical engineering, TU Vienna, a fully integrated temperature swing adsorption bench scale unit (TSA-BSU) for continuous capture of about 35 kg of CO₂ per day was designed, constructed and put into operation [67]. Further information about the BSU campaign can be found in the Master Thesis *“A novel system for continuous temperature swing adsorption: parameter study at bench scale”* written by Dipl.-Ing. Florian Dietrich, directed by Prof. Hermann Hofbauer (TU Vienna, Austria) [13].

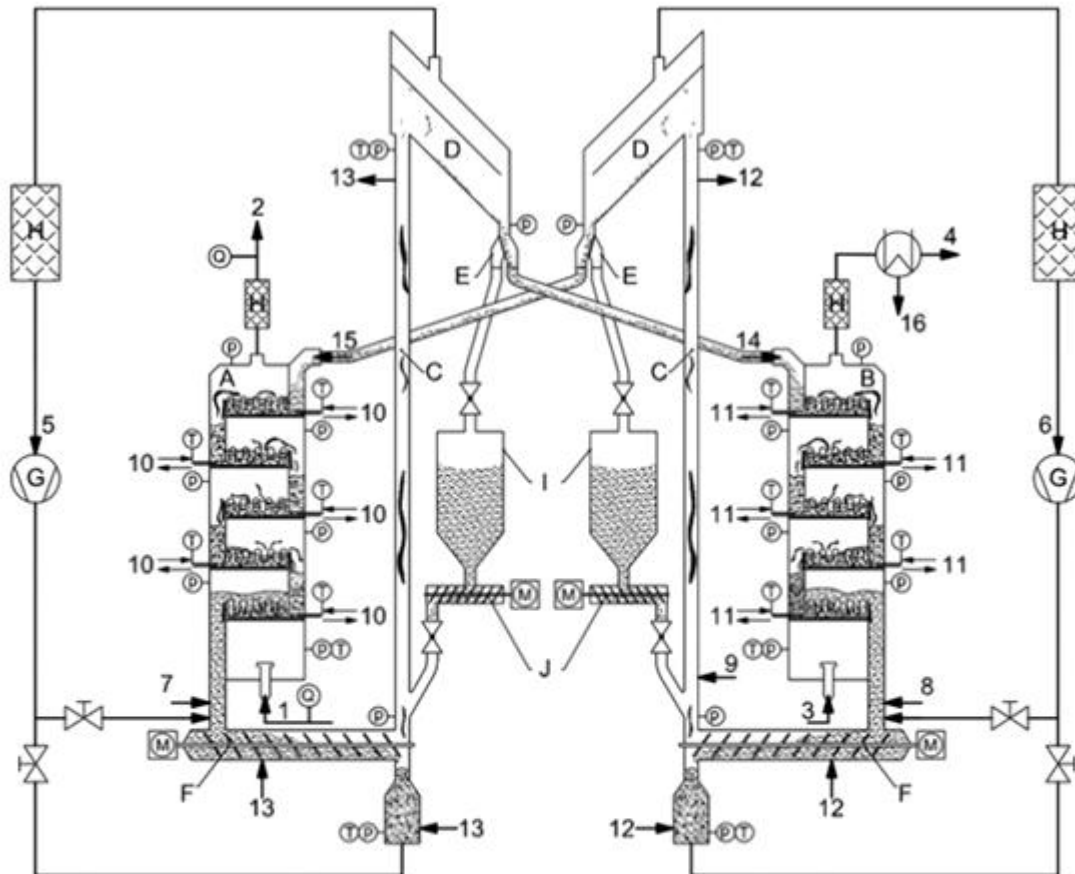
Figure 1.6. shows the design of the TSA bench scale unit (BSU). It is based on a dual column multistage fluidized bed system. The walls of the adsorber are made of glass, while the desorber is entirely made of steel in a double wall design. Each stage (adsorber & desorber) consists of a distributor plate, to ensure an optimal gas distribution, a copper heat exchanger, immersed in the bed of sorbents in order to supply and discharge heat, a weir over which it is possible to adjust the height of the fluidized bed, and an internal downcomer to allow a mass flow of the sorbent. As a sorbent an amine functionalized material is used. In each stage a bubbling fluidized bed is formed. The sorbent flows counter-currently to the fluidization gas, with a certain known and adjusted CO₂ concentration. As the sorbent in the adsorber column is transported by the downcomers from one stage to the next, the sorbents get loaded with CO₂, while the CO₂ concentration

in the fluidization agent decreases from bottom to top. After the loaded sorbent reaches the lowest stage it is fed into the desorber column by means of a screw conveyor via the riser. Similar to the adsorber, the sorbent is transported from the top of the column to the bottom, and again fed back into the adsorber column. The fluidization agent in the desorber column is steam or N_2 [54].

Table 1.1. Table of construction design parameter of the BSU, adapted from [67] and [13]

Adsorber column		
column diameter	150	[mm]
design operating temperature	75	[°C]
feeding gas components	N_2, CO_2, H_2O, Air	[-]
gas flow rate ($y_{N_2} = 95 \%_{Vol.}, y_{CO_2} = 5 \%_{Vol.}$)	46.8	[Nm ³ /h]
design CO ₂ capture efficiency	90	[%]
design CO ₂ capture rate	35	[kg/day]
Fluidization number	10	[-]
Desorber column		
column diameter	110	[mm]
design operating temperature	120	[°C]
feeding gas components	N_2, H_2O, Air	[-]
design gas feeding rate (steam)	6.5	[kg/h]
design gas feeding rate (N_2)	8	[Nm ³ /h]

After successful operation of the constructed bench scale unit, the feasibility of the proposed double loop multi-stage fluidized bed system via temperature swing adsorption was proved. In 2016, a continuous operation of 120 hours was carried out. The next planned step of the “Future Energy Technology”-group, in collaboration with other partners, is an upscale to a pilot scale unit (PSU). Therefore, a cold flow model was designed in order to de-risk and improve the reactor design from a fluid- dynamic point of view, especially, the downcomers in the adsorber column . Based on this idea, the following work was written.



- | | | |
|-------------------------------|---|--|
| A ... adsorber | 1 ... syn. flue gas (N ₂ , CO ₂ , air, steam) | 11... desorber stage heating |
| B ... desorber | 2 ... clean flue gas | 12... transport line cooling |
| C ... riser | 3 ... stripping gas (N ₂ , steam) | 13... transport line heating |
| D ... gas-solids separator | 4 ... CO ₂ product (+ N ₂) | 14... CO ₂ loaded adsorbent |
| E ... solids directing flap | 5 ... recirculation gas | 15... regenerated adsorbent |
| F ... bottom screw conveyor | 6 ... recirculation gas | 16... strip. steam condensate |
| G ... recycle-gas blower | 7 ... purge gas (N ₂ , CO ₂) | ⊙ ... pressure sensor |
| H ... particle filter | 8 ... purge gas (N ₂ , steam) | ⊙ ... temperature sensor |
| I ... adsorbent storage | 9 ... dilution stream (N ₂) | Ⓜ ... driving motor |
| J ... adsorbent feeding screw | 10... adsorber stage cooling | Ⓞ ... gas analytics |

Figure1.6. .Basic scheme of a double loop staged fluidized bed system for continous TSA [67]

1.4. Problem definition

1.4.1 Aim of this work

Extensive testing on a multistage fluidized bed cold flow model (MStFB-CFM), designed at TU Vienna, was carried out. The experiment includes variations of internal downcomers, in terms of entrance height between the downcomer and the lower stage, geometry by means of length and width adjustment, applied area, as well as experiments with external downcomers. In this work the experimental campaign, which was carried out in the first half of 2016, is analyzed.

The objective of this work was the determination of the solid flux as a reference, depending on the entrance height, geometry and applied area of several downcomers to further optimize the downcomers of the adsorber column of the planned pilot scale unit (PSU) and to gain more experience regarding to the stable operation parameter. Furthermore, experiments with external downcomers were carried out to investigate a possible application of them in the planned PSU.

1.4.2 Organization

Chapter 1 combined a brief motivation for this research area as well as a short introduction into carbon capture and storage. Chapter 1.3, was a brief introduction of the TSA-Bench scale unit, which was designed at the TU Vienna, and a short outlook of the future pilot scale unit. In Chapter 2, “*Theoretical Background*”, the fundamentals of fluidized bed systems, and multistage fluidized bed systems, will be briefly introduced in order to provide the necessary theoretical background for the practical parts and discussion within this thesis. A brief insight into the general design of the cold flow model (CFM) used in this study is shown in Chapter 3, followed by a detailed description of the experimental setup, as well as the evaluation used for the experiments in this work. Results obtained during the experimental campaign are shown in Chapter 4. Chapter 5, “*Summary & Conclusion*” also comprises the interpretation of the results, highlights the main conclusion that can be derived from this thesis, and gives an outlook on further developments.

2. Theoretical background

The second Chapter “Theoretical Background” will present the fundamentals of fluidized bed systems. It should be kept in mind that fluidized bed applications are not limited to gas-solid systems but can instead be realized in all different kinds of gas-liquid-solid phase combinations [4]. Nevertheless, this chapter covers only on gas-solid fluidized bed systems, since this thesis was based on gas-solid systems.

2.1. Fundamentals of fluidized bed systems

2.1.1. Historical background

In the course of the Haber-Bosch process optimization, the German chemist, Fritz Winkler, developed the first fluidized bed gasification, with the objective to produce synthesis gas from lignite. In those days he worked for the German company “*Badische Anilin und Soda-Fabrik*”(BASF). His discoveries led to his own patent, which he registered in 1922, and furthermore to the fundamentals of the fluidized bed technologies [64]. The world’s first fluidized bed system was implemented in 1926 for the purposes of coal gasification [22]. This unit was 13m high and 12 m² in cross section. The desired reaction, simply represented, is as follows [37].



In 1929, an additional four new plants were commissioned. Thirteen years later, in 1942, the first industrial-scale circulating fluidized bed reactor was first put into operation by the Standard Oil Company of New Jersey (now Exxon), in order to crack heavy kerosene [1]. At the beginning, they were plagued by problems due to the excessive pressure drop in long tubes. Exxon engineers concentrated on the idea of Professor Lewis (Massachusetts Institute of Technology) and Professor Gilliland (Massachusetts Institute of Technology) and verified that a standpipe was crucial for smooth circulation, and came up with a large up flow pilot-plant (*Figure 2.1. (b)*). This was the start of fluid catalytic cracking (FCC).

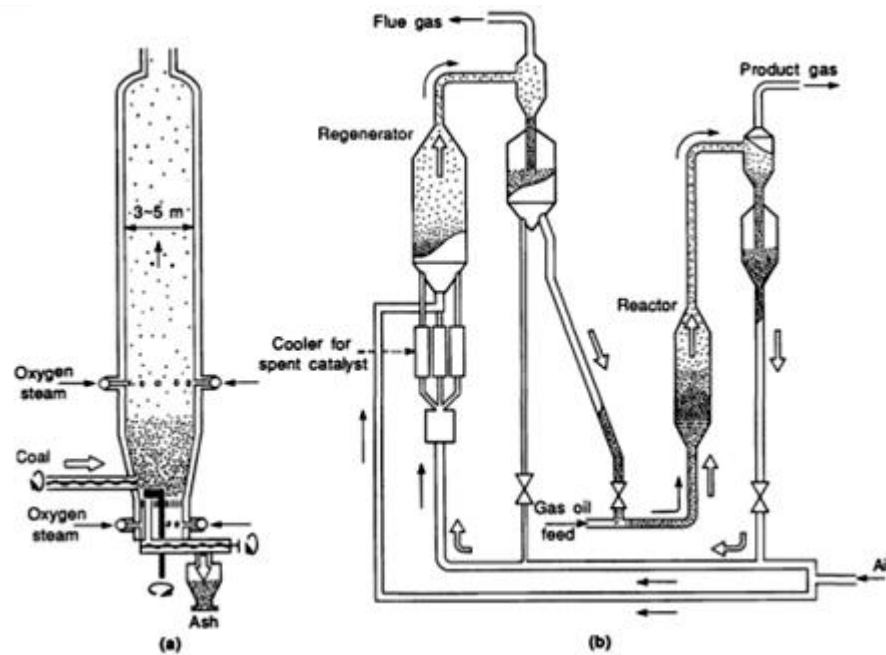
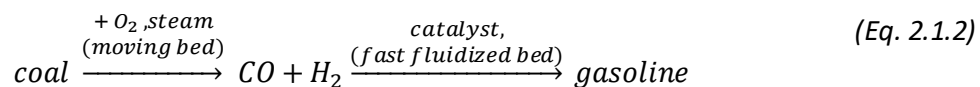


Figure 2.1. (a) The Winkler gas Generator; (b) the first large-scale pilot plant for fluid catalytic cracking. [37]

Shortly after the first pilot plant was put in operation, it has aroused interest for many scientists. This resulted in a new thematic focus in the mid-1940s. One of the most vigorous attempts was made in the United States to use the fluidized bed for the Fisher-Tropsch reaction. In simple terms, the mode of reactions is as follows [37]:



Independently in 1945, the German company BASF had begun to develop fluidized bed roasters based on experience acquired with the Winkler gas producer. Finally, they constructed their first roaster in 1950, which went in operation at Ludwigshafen with a capacity of 30 tons of ore per day [37]. Nowadays, fluidized bed technology is common practice in many process engineering sectors and covers a wide range of applications, such as fluidized-bed drying, fluidized bed blending, heat-exchange systems, adsorption, granulation/agglomeration, combustion plants, gasification plants, roasting of ores, reduction of metal oxides, thermal and catalytic cracking, synthesis, and so on [37].

2.1.2. Fluidized bed existence range

In order to provide a better understanding of a fluidized bed, a simplification is given as: A stationary bed of solids of equal size and density is placed on a porous plate in a cylindrical vessel. The gas flows upwards through the bed at a superficial velocity of U , whereby the superficial gas velocity U is defined as the ratio between the total volumetric gas flow rate and the cross section of the empty vessel [63].

$$U = \frac{\dot{V}_{\text{Fluidization agent}}}{A_{\text{reactor cross-section}}} \quad (\text{Eq. 2.1.3})$$

The gas, or fluidization agent, is flowing through the bed and exerts a certain drag force to the particles. The impact of the drag force thereby depends on the gas flow rate. The pressure drop Δp along the bed can be expressed as the drag force divided by the cross section of the cylindrical vessel. A typical course of the curve, whereby the volume flow is plotted on the abscissa and the pressure drop on the ordinate of the diagram, is shown in Figure 2.2.

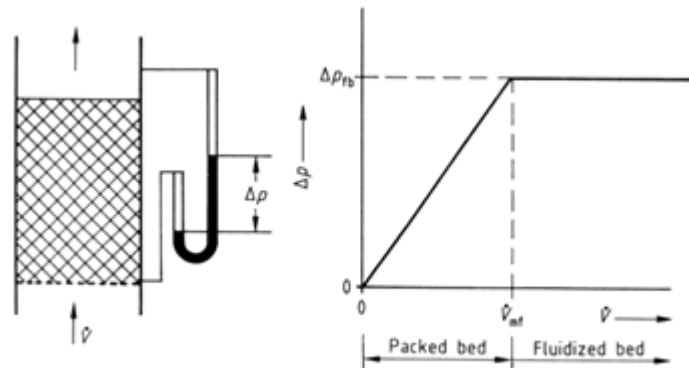


Figure 2.2. Pressure drop induced by a gas flowing through a bed [63]

Depending on the gas velocity, different flow regimes can arise as shown in Figure 2.3. As shown in Figure 2.3., the gas velocity increases rightwards to a certain point, till pneumatic transport occurs.

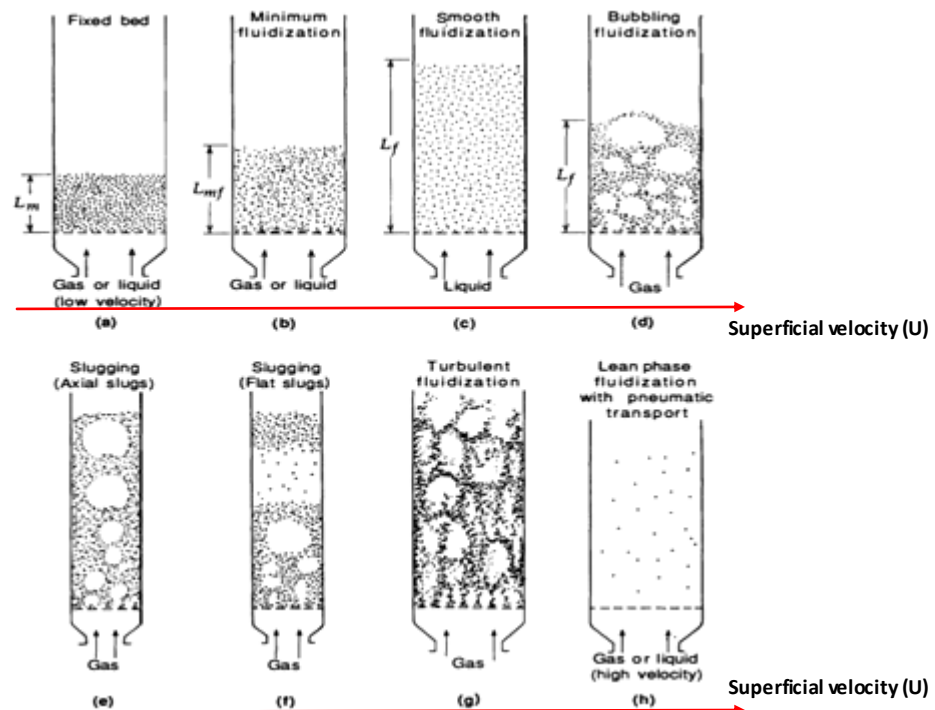


Figure 2.3. Schematic representation showing the appearance of flow regimes relevant to gas-solid fluidization [37]

Fixed bed ($0 < U < U_{mf}$)

A fixed bed occurs, if the gas velocity is kept at a low value [Figure 2.3 (a)]. In a fixed bed all particles have a fixed position and no movement. The pressure drop increase nearly linear or quadratic. If the velocity is increased gradually, the bed expansion begins and the particle starts to move. This point is defined as the minimum fluidization velocity U_{mf} [Figure 2.3 (b)] and the start point of a fluidized bed system. In a liquid-solid system an increase results in a smooth fluidization [Figure 2.3 (c)], whereas in solid-gaseous systems this phenomenon is unlikely.

Bubbling fluidization ($U_{mb} < U < u_t$)

If the superficial gas velocity gas reaches the minimum bubbling velocity (U_{mb}) bubbles occur near the distributor [Figure 2.3 (d)]. Bubbles grow by coalescence and rise to the bed surface [11]. The minimum bubbling velocity can be evaluated by equation Eq. 2.1.4 [42]:

$$U_{mb} = 33 \cdot d_p \cdot \left(\frac{\rho_g}{\mu_g} \right)^{0.1} \quad (\text{Eq. 2.1.4})$$

It should be noted, that three different flow phenomena may arise. Homogeny fluidized bed (solid particles are evenly distributed in the gas flow), heterogenic fluidized bed (solid particles are not evenly distributed) or a bubbling fluidized bed (especially if gas is used as the fluid). The expansion of bubbles can lead to slugging phenomena [Figure 2.3. (e)/(f)] (bubbles achieve the same diameter as the vessel). Slugging phenomena should be avoided, since a stable operation is no longer ensured. Fluidized bed systems can be stable over a wide range of gas velocities, until the terminal velocity u_t [Figure 2.3. (h)] is reached. Before the terminal velocity is reached, the flow structure of bubbling fluidized beds can change to a turbulent fluidized bed [Figure 2.3. (g)]. At the turbulent regime the porosity further increases and particles build clusters which float up and down. Furthermore, the upper surface of the bed disappears and instead of bubbles, turbulent motions are recognizable. A characteristic phenomenon of a turbulent fluidized bed is low fluctuations in pressure (the system makes a calmer impression). After the terminal velocity is reached, the pneumatic transport dominates [24]. In most applications, fluidized bed systems operate at a multiple rate of the minimum fluidization number. At these high gas velocities, particles are blown from the bed into the freeboard arranged above. This phenomenon is called entrainment. The higher the gas velocity, the more powerful is this process. If the gas velocity reaches the terminal velocity of the particle classes, they get discharged from the reactor regardless of the height of the freeboard above. Larger particles, whose terminal velocity is not reached, stay in the dense phase.

Normally, a fluidized bed consists of particles with a wide particle size distribution. As shown in Chapter 2.1.6, particles with a greater diameter also have a higher terminal velocity. Therefore,

small particles which have reached the terminal velocity are discharged first. Larger particles are also thrown into the freeboard, through the bubble explosion at the surface, but fall back into the bed. Resulting from this effect, one can see the typical particle concentration distribution for fluidized beds in *Figure 2.4*.

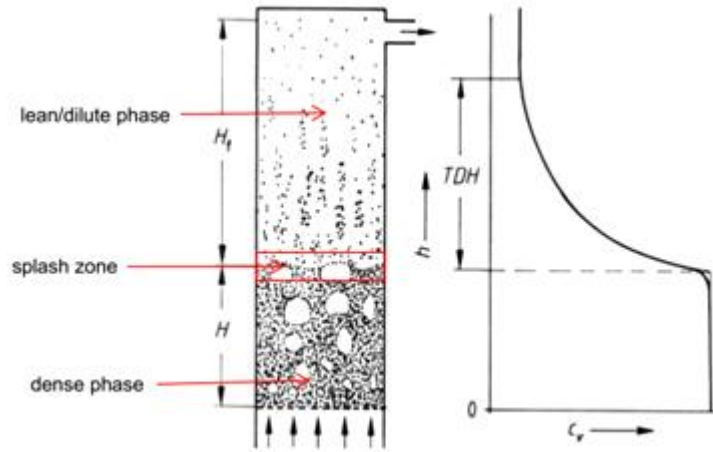


Figure 2.4. Solids distribution in bubbling fluidized bed reactors, adapted from [63]

A "dense phase" is present in the fluidized bed. At the surface of fluidized beds, the particle concentration decreases rapidly and transfers into a "lean phase". The transition between fluidized bed and freeboard is called "splashzone". The splash zone is formed by the ballistic movement of particles and cluster and is characterized by vigorous solid-gas mixing [63].

The concentration along the freeboard height shows a characteristic exponential decay. There is agreement on the fact that the mass flow exponentially decreases in relation to the height. Even in a fluidized bed without large particles (with $u_t < U$), this exponential decrease is present [63]. The height where the particle concentration reaches a constant value is determined as the "transport disengaging height" (TDH). Above the TDH only particles are located, whose terminal velocity is smaller than the local superficial gas velocity (i.e. with $u_t < U$). However, larger particles and particle clusters are also located in the Freeboard, but fall back into the fluidized bed if the height of the freeboard is higher than the TDH.

2.1.3. Particle size definition and characteristic

The characteristics of a single particle in a fluidized bed system are mostly defined by the following physical parameters:

- Particle size [d]
- Particle shape or sphericity [ϕ_s]
- And hydrodynamic particle density [ρ_p]

Generally, the solid is in the form of aggregate material with a certain particle size distribution (PSD). Therefore, these parameters come into effect:

- Particle size distribution – PSD $d_i, x_i (d_m, \sigma)$
- Porosity or voidage [ϵ]
- And bulk density ρ_b

The essential parameter for the specification of the particle size is the diameter. For all practical purposes and technical application, the form of the particles differ to an ideal spherical shape, therefore an equivalence diameter must be defined. As described in other sources, like in the Handbook of Fluidization [65], there are a large variety of definitions. The commonly used in fluidization technology, are outlined in the table (Table.2.1.) below:

Table 2.1. Table of several diameters for particle size definition [52]

Designation	Description	Formula
sieve diameter d_p	width of the minimum square aperture that permits passing of the particle	
volume diameter d_v	diameter of a sphere with equivalent volume as the particle	$d_v = \sqrt[3]{\frac{6 \cdot V}{\pi}}$
surface diameter d_s	diameter of a sphere with equivalent surface area as the particle	$d_s = \sqrt{\frac{A}{\pi}}$
Sauter's diameter d_{SV}	diameter of a sphere with equivalent volume to surface area ratio as the particle	$d_{SV} = \frac{6 \cdot V}{A} = \frac{d_v^3}{d_s^2}$
median diameter of the volumetric PSD d_{50} or $d(0.5)$	50% of the particles within the bed material have a smaller diameter than d_{50}	

Several equivalence diameters are intertwined by the “sphericity” [φ_s].

$$\varphi_s = \left(\frac{\text{surface of a sphere}}{\text{surface of the particle}} \right)_{\text{of same volume}} = \left(\frac{d_v}{d_s} \right)^2 \quad (\text{Eq. 2.1.5})$$

According to Eq. 2.1.5, φ_s equals 1 if the particle has an ideal spherical shape or lies between $0 < \varphi_s < 1$ for all other forms of particle shapes. It is referred to as a sphere, since a sphere shows the minimum possible surface to volume ratio.

Particle sphericity values of technical relevant materials are usually within the range of $0.6 < \varphi_s < 1$.

Table 2.2. Table of sphericity of technical relevant materials [52]

Material	Sphericity [φ_s]
Crushed coal	0.75
Crushed glass	0.65
Crushed sandstone	0.8 to 0.9
Mica flakes	0.28
Common salt	0.84
Glass beads (used for sandblasting)	0.92 to 0.98

To simulate a bulk of non-spherical particles with the same particle surface and voidage as a layer with spherical particles, an assumption is required. This assumption should show similar pressure drop characteristics. Consequently, an equivalence diameter called Sauter’s diameter can be defined:

$$d_{sv} = \varphi_s \cdot d_v \quad (\text{Eq. 2.1.6})$$

One approach to determine φ_s is to measure the pressure drop over a fixed bed of solids and further use this value to calculate d_{sv} from the Ergun equation (see Eq. 2.1.12). The volume diameter d_v can be determined by measuring the mass (M) of a known number (N) of the same particles, in case the particle density (ρ_p) is known.

$$d_v = \left(\frac{6 * M}{N * \pi * \rho_p} \right)^{1/3} \quad (\text{Eq. 2.1.7})$$

Usually a sieve analysis is performed to determine the diameter of the particle d_p . The Sauter’s diameter has been selected as representative diameter for fluid-dynamic calculations in this work, even though the Sauter diameter is typically used for aggregates of non-spherical and non-uniform particles. Even if there is no valid relation between the Sauter’s diameter and the sieve diameter, the following approximations are commonly used [24]:

- a.) Close to spherical particles: $d_{SV} \approx \varphi_s * d_p$
- b.) Particles, where one length is dominating, but less than 2:1 (ovoid partide) $d_{SV} \approx d_p$
- c.) Particles, where one length is smaller than the others, but not less than 1:2 (disc-shaped particle): $d_{SV} \approx \varphi_s^{2*} d_p$

As a rule of thumb, for almost spherical particles exist the valid relation [24]: $d_{SV} \approx d_p \approx d_v$

2.1.4. Porosity and bulk density

The voidage [ε] is defined as the relative amount of the free space between the particles, and can thus be calculated according to equation (Eq. 2.1.8):

$$\varepsilon_{mf} = \frac{\text{solids free bed volume}}{\text{total bed volume}} = \frac{V_{FB} - V_P}{V_{FB}} = 1 - \frac{V_p}{V_{FB}} = 1 - \frac{\rho_b}{\rho_p} = 1 - \frac{M}{\rho_p * V_{FB}} \quad (\text{Eq. 2.1.8})$$

The Parameters in the equation above are the mass of the entirety partides (M), the particle density (ρ_p) and the total bed volume (V_{FB}).The bulk density can be determined by solving the equation:

$$\rho_{FB} = \frac{M}{V_{FB}} \quad (\text{Eq. 2.1.9})$$

The voidage should be determined in the same conditions as in operation and essentially depends on the characteristics of the used bed material, whereas the following general aspects can be stated:

- Particle form: The lower the sphericity, the higher the voidage of the fixed bed .
- Particle size: The bigger the particles, the lower the voidage of the fixed bed.
- Particle size distribution: The narrower the partide size distribution, the higher the voidage of the fixed bed.

2.1.5. Particle classification according to Geldart

Depending on the mean size and density of the bed material used, different fluidization characteristics can be expected. These phenomena result from inter-particle adhesion and cohesion forces, which are acting in the bed. For very fine particles these forces can exceed the viscous forces from the gas flow and directly affect the fluidization behavior so that it will be different from the be-

havior of denser and bigger particles. The classification of bulk-material fluidization behavior was done by Geldart in 1973 [19], who differentiated four different groups (Geldart A-D particles) based on their particle size, and density difference between particles and the fluidization agent ($\rho_p - \rho_f$). As shown in Figure 2.5., these groups are typically visualized within a diagram having the particle diameter d_p drawn on the abscissa and the density difference ($\rho_p - \rho_f$) on the ordinate.

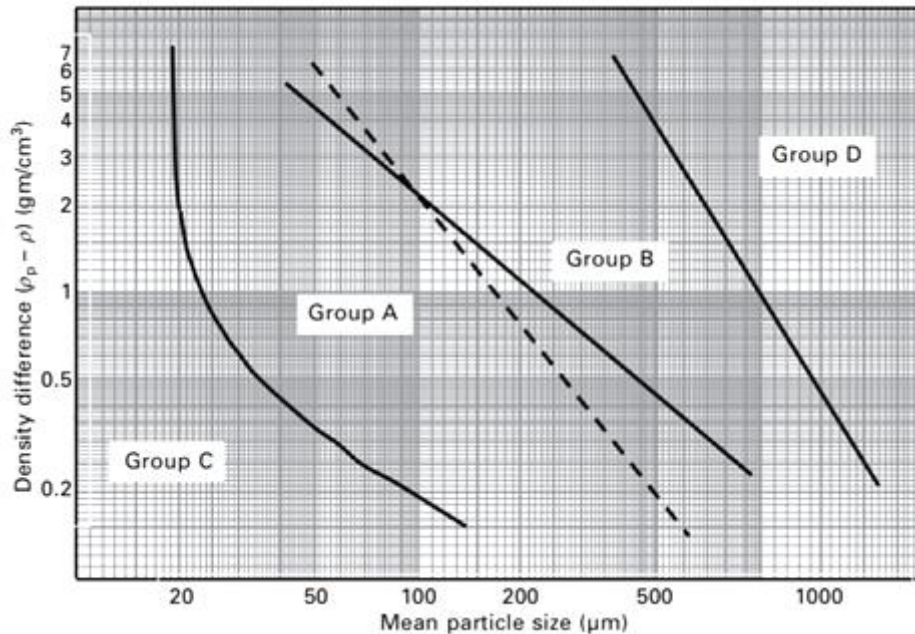


Figure 2.5. Geldart classification of particles for air at ambient conditions [52]

- Geldart group C particles:

This group of particles includes all bulk materials that are cohesive in any way. The fluidization of these materials is extremely difficult, since they tend to form gas channels and plugs. This effect is explainable by the inter-partide adhesion forces, which are higher than the viscous forces from the gas flow, acting on a single particle, which causes the particles to dump together. The practical importance of this group in fluidized bed systems is insignificant. The solids are very fine-grained and often cannot be fluidized without a fluidization aid. In cases where a fluidization of the particles is needed, the fluidization behavior can be improved through mechanical equipment such as mechanical vibrator units or chemical additives [63]. Typical powders that belong to this particle group are flours, starch and face powder [37]

- Geldart group A particles:

Particles belonging to this group have a small mean size and/or low density ($<1.4 \text{ g/cm}^3$), such as FCC catalysts [63]. Fluidized bed systems with particles belonging to this group are characterized in that when the minimal fluidization velocity is exceeded, first the bed starts to expand homogeneously and uniformly, then the bubble formation starts. Bubble formation occurs at a specific fluidization velocity, the minimum bubbling velocity U_{mb} (Eq. 2.1.4). The formed bubbles, howev-

er, do not grow significantly but instead stay small. The reason for this is that the particles are slightly cohesive. They are easy to fluidize and can be transported well, especially using pneumatic transport. These materials are primary used for expanding, circulating fluidized bed systems [37]. If the gas flow is stopped, the bed collapses rather slowly [63].

- Geldart group B particles:

Particles that belong to this group are characterized by moderate particle sizes (40-500 μm) and densities (1.4 - 4g/cm³) [37]. Typical representatives of this group are sands.

In contrast to particles belonging to Geldart group A, the inter-particle forces are not significant. Bubble formation occurs right after transition from fixed to fluidized bed regime, or in other words, after exceeding the minimal fluidization velocity U_{mf} . It is necessary to consider, that a homogenous bed expansion is not valid. The dominating phenomenon of this group is the bubbling formation, which causes a good intermixing of the material. Bubbles can grow very large due to coalescence since growth is not limited by bubble splitting [63]. In deep beds and small vessels, slugging regime can be observed and bubble eruption can be vigorous in this regime. If the gas flow is stopped, the bed collapses quickly [63].

- Geldart group D particles:

This group of particles includes large (>0.5mm) and dense particles such as coffee beans, grains and peas. Some roasting metal ores belong to this group too. Hence, the main practical applications of this group are the agricultural, pharmaceutical and the food sectors. Deep beds of these solids are difficult to fluidize. Typically, bubbles formation occurs slowly compared to group B solids. Large exploding bubbles, severe channeling, or spouting behavior if the gas distribution is very uneven, can be observed [37].

2.1.6. Pressure drop

Pressure drop in the fixed bed

Usually a model concept is used, which describes the flow through a fixed bed with parallel, connected channels with changing cross-sectional areas. For $Re < 1$ (Eq. 2.1.11), the Carman-Kozeny equation proved to be useful [65]:

$$\frac{\Delta p_{Fix}}{H} = 180 \cdot \frac{(1-\varepsilon)^2}{\varepsilon^3} \cdot \frac{\mu \cdot U}{d_{sv}^2} \quad (\text{Eq. 2.1.10})$$

With:

$$Re = \frac{U^* d_{sv}^* \rho_g}{\mu_g} \quad (\text{Eq. 2.1.11})$$

(Note: $d_p \approx d_{sv}$ for almost spherical particles)

For $Re > 1$ the turbulent term must also be considered. Therefore, the Equation according to Ergun is practically relevant, whereby the left term in (Eq. 2.1.12) describes the laminar flow and the right term considers the turbulent flow [16].

$$\frac{\Delta p_{Fix}}{H} = 150 \cdot \frac{(1-\varepsilon)^2}{\varepsilon^3} \cdot \frac{\mu \cdot U}{d_p^2} + 1.75 \cdot \frac{1-\varepsilon}{\varepsilon^3} \cdot \frac{\rho_g \cdot U^2}{d_p} \quad (\text{Eq. 2.1.12})$$

According to Eq 2.1.12., it is recognizable that in the case of a laminar flow ($Re < 1$) the pressure drop referred to the bed height has to be proportional to:

$$\frac{\Delta p_{Fix}}{H} \text{ prop } \frac{\mu \cdot U}{d_p^2} \quad (\text{Eq. 2.1.13})$$

In the case of turbulent flows ($Re > 1000$) the pressure drop referred to the bed height has to be proportional to:

$$\frac{\Delta p_{Fix}}{H} \text{ prop } \frac{\rho_g \cdot U^2}{d_p} \quad (\text{Eq. 2.1.14})$$

Hence, the second term of the Equation is dominant. As shown in Figure 2.6., the pressure drop after Eq.2.1.10 is linear, while the pressure drop according to Eq. 2.1.12 has a quadratic path over the superficial velocity.

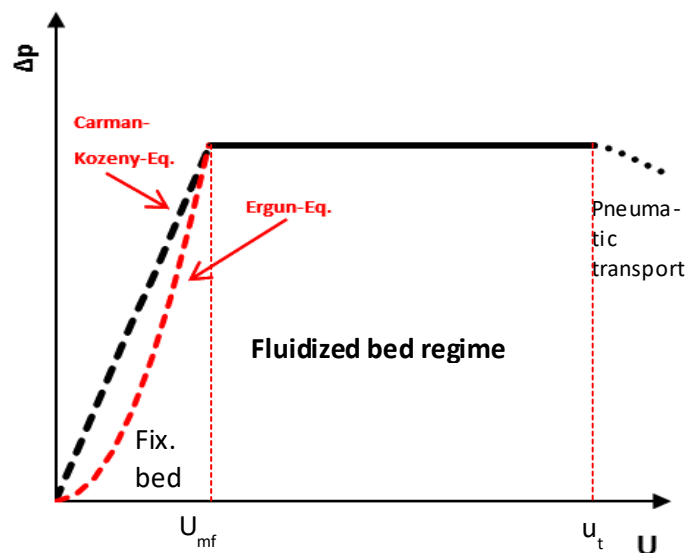


Figure 2.6. Pressure drop induced by a gas flowing through a bed, adopted from [24]

Pressure drop in the fluidized bed

The fixed bed changes into the fluidized bed when the resistance force of the gas flow is equal to the weight of particles reduced by the buoyancy. This equilibrium of forces can be expressed as:

$$A \cdot \Delta p_{FB} = (1 - \varepsilon_{mf}) \cdot (\rho_p - \rho_g) \cdot g \cdot H \cdot A \quad (\text{Eq. 2.1.15})$$

Divided by the cross section of bed, the fundamental fluidization equation results:

$$\Delta p_{FB} = (1 - \varepsilon_{mf}) \cdot (\rho_p - \rho_g) \cdot g \cdot H \quad (\text{Eq. 2.1.16})$$

The first term in the equation includes the bed voidage at minimum fluidization conditions ε_{mf} which is defined according to Eq. 2.1.8.

This pressure drop is independent of the gas velocity. Hence, the pressure drop is constant in the range between the minimum fluidization velocity U_{mf} and the terminal velocity u_t (see Figure 2.6.)

2.1.7. Minimum fluidization velocity and single particle terminal velocity

The minimum fluidization velocity U_{mf} represents the transfer between a fixed bed and a fluidized bed. The pressure drop increases in fixed bed according to the Carman- Kozeny equation (Eq. 2.1.10) or Ergun equation (Eq. 2.1.12) and remains constant in fluidized bed. Even if the superficial gas velocity is further increased, the pressure drop along the bed stays constant since the mass of fluidized solids stays constant until entrainment occurs, after reaching the terminal velocity u_t (Figure 2.6. and Figure 2.7.). The pressure drop in solid/gas-systems can be approximately expressed as [37]:

$$\Delta p_{FB} = \frac{M \cdot g}{A} \quad (\text{Eq. 2.1.17})$$

First, particles with the smallest diameter start to move and whirl, whereas particles with larger diameters stay in their basic state. In order to determine the minimum fluidization velocity U_{mf} , the linear course of the pressure drop in fixed beds and fluidized beds is extended to a point of intersection of the two lines. In the case of an experimental determination of U_{mf} it must be ensured that in the fixed bed the loosest possible bulk exists. Compacted bed material could result in higher measured values of the pressure drops. A simple and commonly used method of determination is to take the pressure course starting with a point in the fluidized bed regime and then gradually reduce the gas velocity.

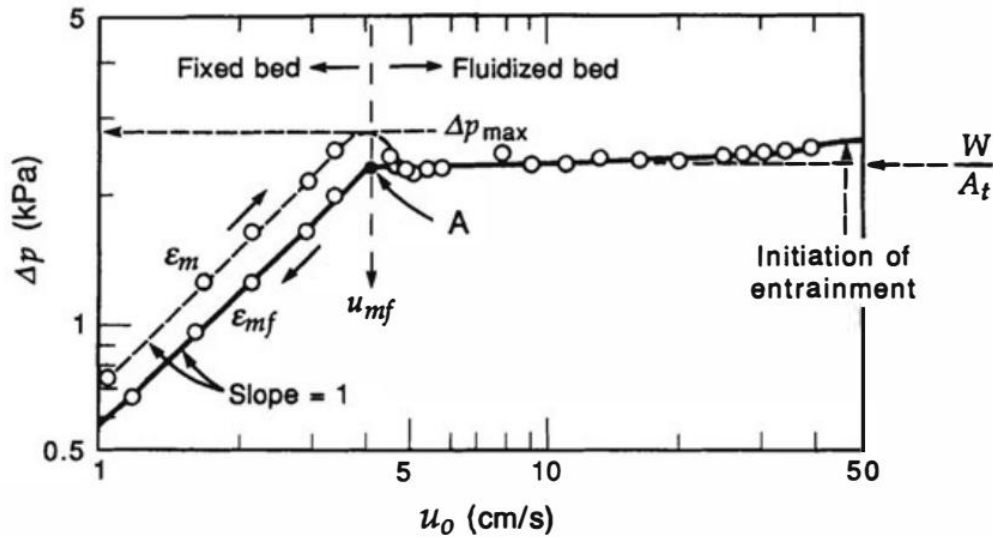


Figure 2.7. Pressure drop across a bed of particle as a function of gas velocity [37]

An equation for the minimum fluidization velocity can be derived by equating the pressure drop in a fixed bed according to Eq 2.1.12, and the pressure drop in fluidized bed according to Eq.2.1.16, since the pressure drop of the fixed bed must equal the pressure drop in the fluidized bed at minimum fluidization conditions. By equating these two equations, Eq 2.1.18 results:

$$\frac{d_p^3 \cdot (\rho_p - \rho_g) \cdot \rho_g \cdot g}{\mu^2} = 150 \cdot \frac{(1-\varepsilon)}{\varepsilon^3} \cdot \frac{U \cdot d_p \cdot \rho_g}{\mu} + 1.75 \cdot \frac{1}{\varepsilon^3} \cdot \frac{U^2 \cdot d_p^2 \cdot \rho_g^2}{\mu^2} \quad (\text{Eq. 2.1.18})$$

The term on the left side shows the dimensionless Archimedes number, which is defined as:

$$Ar = \frac{d_p^3 \cdot (\rho_p - \rho_g) \cdot \rho_g \cdot g}{\mu^2} \quad (\text{Eq. 2.1.19})$$

An equation for the minimum fluidization velocity can be derived by introducing the Reynolds number (Eq. 2.1.11), that reads as follows

$$Ar = C1 \cdot Re_{mf}^2 + C2 \cdot Re_{mf} \quad (\text{Eq. 2.1.20})$$

Or:

$$Ar = \frac{1.75}{\varepsilon_{mf}^3} \cdot Re_{mf}^2 + \frac{150 \cdot (1 - \varepsilon_{mf})}{\varepsilon_{mf}^2} \cdot Re_{mf} \quad (\text{Eq. 2.1.20b})$$

If the bed voidage and particle diameter is already experimentally determined, then this equation can be used to calculate U_{mf} from Re_{mf} directly. Based on experimental results, Wen and Yu [62] found that the coefficients in front of the Reynolds-Numbers in Eq. 2.1.20 remain constant for a

very broad operating range ($0.001 < Re < 4000$). They thus introduced constant values for these which led to the following correlation that can be used to estimate the minimum fluidization velocity :

$$U_{mf} = \frac{\mu}{d_p \cdot \rho_g} \cdot \left(\sqrt{33.7^2 + 0.0408 \cdot Ar} - 33.7 \right) \quad (\text{Eq. 2.1.21})$$

This equation has proved to be a good choice for various materials and particle diameter. Years later, Grace [22], introduced different coefficients and ended up at the following equation :

$$U_{mf} = \frac{\mu}{d_p \cdot \rho_g} \cdot \left(\sqrt{27.2^2 + 0.0408 \cdot Ar} - 27.2 \right) \quad (\text{Eq. 2.1.22})$$

In this work, the minimum fluidization velocity was determined experimentally. However, to obtain a comparison, the Eq.2.1.22 according to Grace was used.

One important parameter in this work, which is directly linked to the minimum fluidization velocity, is the fluidization number. The fluidization number is defined as the ratio between the actual superficial gas velocity inside the vessel and the minimum fluidization velocity of the particles.

$$\text{Fluidization number} = \frac{U}{U_{mf}} \quad (\text{Eq. 2.1.23})$$

Another important gas velocity in fluidized bed systems is called the terminal velocity u_t , which limits the area of fluidized bed upwards. The terminal velocity marks the transition from fluidized bed regime to pneumatic transport. Considering a free falling single (spherical) particle through a fluid, the equilibrium of forces can be expressed as [35] (Figure 2.8.):

The acceleration force is equal to the gravitational force reduced by buoyancy- and drag force, or expressed as a general equation:

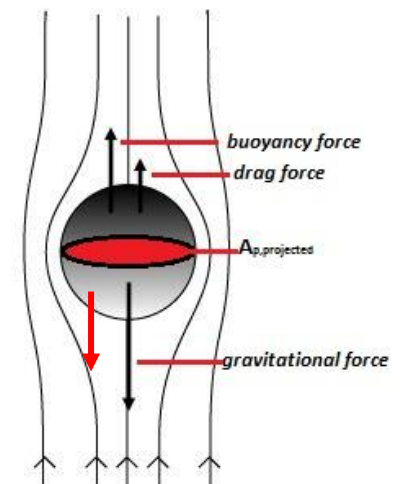


Figure 2.8. The equilibrium of forces

$$\frac{d_p^3 \cdot \pi}{6} \cdot (\rho_p - \rho_g) \cdot g - C_D \cdot A_{p,projected} \cdot \frac{\rho_g \cdot U^2}{2} = M_p \cdot a_p = \frac{d_p^3 \cdot \pi}{6} \cdot \rho_p \cdot \frac{dU}{dt} \quad (\text{Eq. 2.1.24})$$

In the case that the single (spherical) particle with diameter d_p has reached its final velocity or, even more concretely, the terminal velocity u_t , the acceleration term on the right side of the equilibrium of forces equals zero, since no further acceleration is possible.

By rearranging the (Eq. 2.1.24), finally the terminal velocity of single spherical particles can be expressed as:

$$u_t = \sqrt{\frac{4}{3} \cdot \frac{\rho_p - \rho_g}{\rho_g} \cdot \frac{d_p \cdot g}{C_D}} \quad (\text{Eq. 2.1.25})$$

The drag equation for the sphere is generally expressed as a function of the Reynolds number (see Eq.2.1.11) The drag coefficient C_D for a sphere can be approximately calculated from one of the following equations under consideration of the respective range of validity [17]:

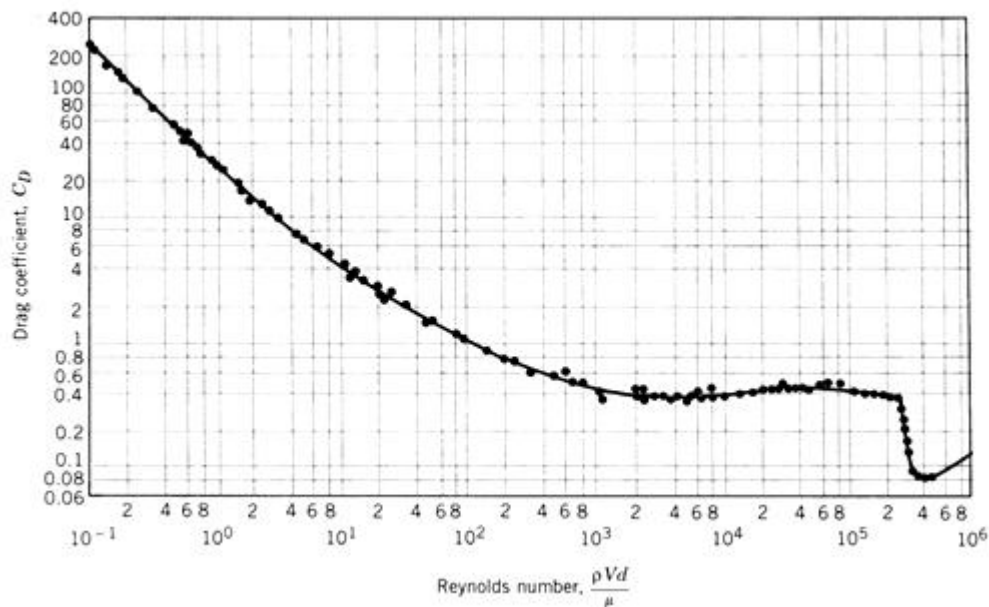


Figure 2.9. Development of the drag coefficient for a sphere with the Reynolds number [35]

Table 2.3. Table of drag coefficient in three Areas

$C_D = \frac{24}{Re}$	$Re \leq 0.11$
$C_D = \frac{24}{Re} + \frac{4}{\sqrt{Re}} + 0.4$	$0.11 < Re < 19345$
$C_D = 0.43$	$Re \geq 19345$

2.1.8. Fluidized bed regime map

As already mentioned briefly in chapter 2.1.1, depending on the gas velocity, different flow regimes can arise. For the representation of the existence ranges in fluidized bed systems, usually existence range diagrams according to Reh or Grace are used. Both diagrams require a minimum of dimensionless numbers to determine the operating condition of the fluidized bed. The transition between the regimes in both maps is smooth and not sharp [25]. The existence range diagram according to Reh can be used to estimate the required gas velocity for setting a particular regime and the width of this operating range. As single particles have a significantly different behavior than particles which belong to Geldart group A and B, Reh considered the effect by including the bed porosity.

Reh used in total four axes in his diagram. As shown in *Figure 2.10.*, the Reynolds number (*Eq. 2.1.11*) is plotted on the abscissa and the modified Froude number (*Eq. 2.1.26*) on the ordinate. Further, the Archimedes number (*Eq. 2.1.19*) as well as the Litaschenko number (*Eq. 2.1.27*) represents the axes inside the map. The bed voidage (at minimum fluidization conditions) extend over an interval of 0.4 to 1.

$$Fr^* = \frac{3}{4} * \frac{U^2 * \rho_f}{g * d_p * (\rho_s - \rho_f)} \quad (Eq. 2.1.26)$$

$$\Omega = \frac{3}{4} * \frac{U^3 * \rho_f^2}{g * \mu * (\rho_s - \rho_f)} \quad (Eq. 2.1.27)$$

Based on the existence range diagram according to Reh, Grace [22] determined a regime map that illustrates the expected fluidization regimes in dependence on a dimensionless particle diameter defined as

$$d_p^* = Ar^{1/3} \quad (Eq. 2.1.28)$$

and a dimensionless superficial gas velocity defined as

$$u^* = \frac{Re}{d_p^*} \quad (Eq. 2.1.29)$$

The advantage of the Grace diagram (*Figure 2.11*) over the existence range diagram according to Reh, is the fact that instead of the usually unknown relative velocity between fluid and particles, also known as the "slip velocity", the superficial velocity can be used. The slip velocity is defined as : $U_{slip} = U - U_s$, whereby U represent the superficial velocity and U_s the velocity of solids [37].

However, the superficial velocity can be easily calculated from the volume flow and the geometries of the reactor, and can often be assumed as constant for the entire reactor (as opposed to the relative velocity).

The choice of the axis allows an illustration of the characteristic fluidization gas velocities but on the other hand also a separation between different types of Geldart particle groups. These regime maps are important tools for the design of fluidized bed systems and cold flow modeling (see Chapter 3.1), as they already give a indication of the expected flow regime.

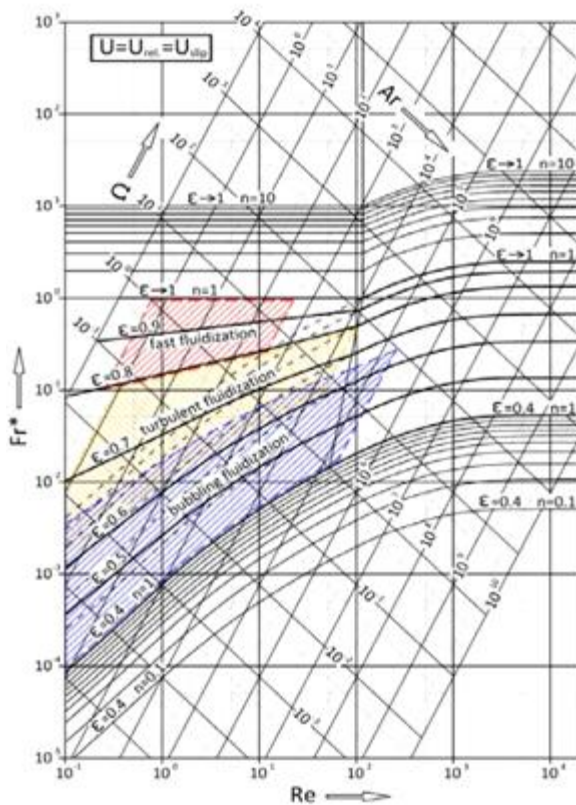


Figure 2.10. Fluidization regime map according to Reh [21]

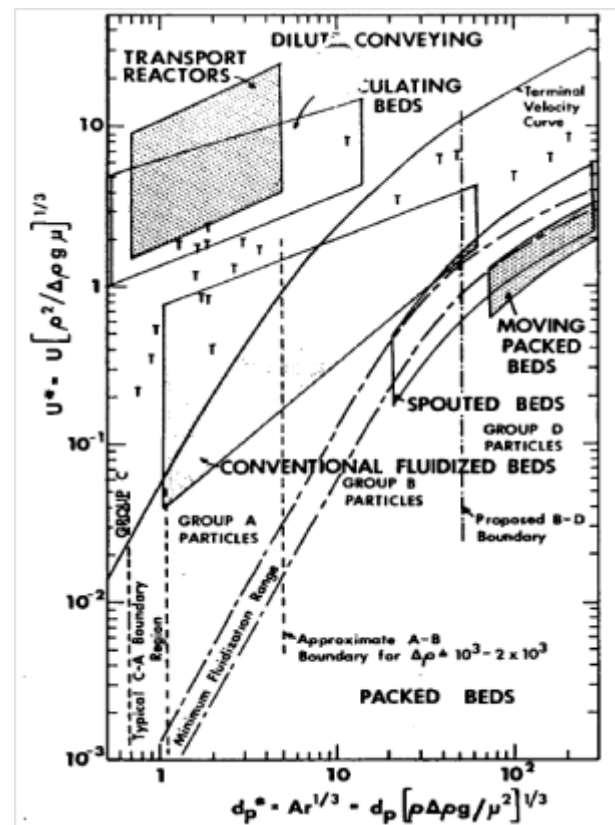


Figure 2.11. Fluidization regime map according to Grace [5]

2.1.9. Heat transfer

Among the many advantageous properties of fluidized beds, the heat-transfer plays an important role. Due to the small porous particles, a giant surface results, with an excellent heat and mass transfer. Therefore, a cubic meter of particles ($d_p = 100 \mu\text{m}$) has a surface of about $30,000\text{m}^2$. As a result of the bubble movement, the fluidized bed has a high effective thermal conductivity in vertical direction. Further, a fluidized bed has a high heat storage capacity. Due to these properties, fluidized bed systems are used for many thermal processes, like in adsorption processes, where

heat exchange control either the adsorption or desorption. In some processes, the heat transfer between gas and particles is significant, in others, the focus lies on the exchanged heat between an immersed heat exchanger (HEX) surface and a fluidized bed [63]. The average heat transfer coefficient is generally affected by three different heat transfer phenomena:

- Particle convective heat transfer
- Gas convective heat transfer and
- Radiant heat transfer

It should be noted that the radiant-proportion can be neglected at temperatures below 600°C [63]. The gas convective contribution for particle diameters smaller than 500 μm is comparatively small and has a negligible impact. Therefore, in a stationary/bubbling fluidized bed of small particles, particle convection can be considered as the dominant heat transfer phenomena.

In Figure 2.12, the impacts of particle diameter and fluidization number on the average heat transfer coefficient are plotted. At gas velocities below U_{mf} (fixed bed) the heat transfer coefficient is significantly lower than in a fluidized bed regime. In a fluidized bed regime, above U_{mf} , bubble formation starts within the fluidized bed and consequently the contact time between the HEX surface and the particle packets changes. Therefore a drastically increase of the average heat transfer is resulting.

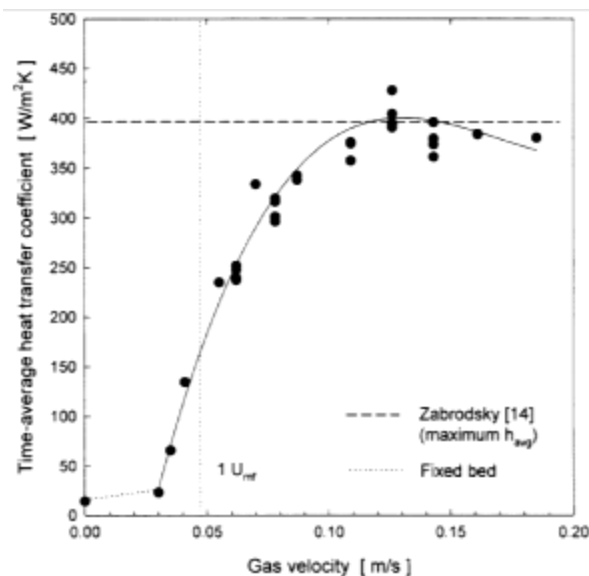


Figure 2.12. Heat transfer coefficient dependency on fluidization number [37].

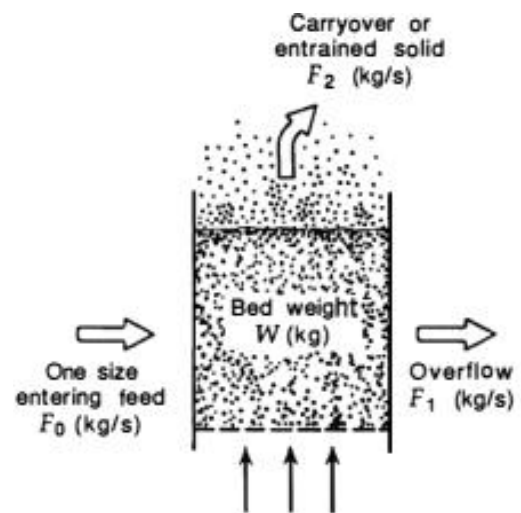


Figure 2.13. Flows in a single-stage fluidized bed with a single-size feed.[37]

2.2. Multistage fluidized bed systems

2.2.1. General aspect

In order to obtain a high product yield, it is necessary that the products, which leave the fluidized bed processes, be uniform, which is only possible if they have spent nearly the same time in the reactor. In order to provide and ensure a long contact time, a multistage fluidized bed column was used in this work. A multistage fluidized bed column has as a basic idea, the conjunction of several fluidized bed systems to one system.

Residence time, is the average amount of time spent in a control volume by the particles of a fluid and is indirectly linked to the uniformity of the bed material in a fluidized bed system [37]. For a given bed weight and flow rate of solids a material balance gives $F_0 = F_1 + F_2$, as one can see in *Figure 2.13*. The residence time (τ) for a single fluidized bed is given as:

$$\tau = \frac{W}{\dot{m}_s} = \frac{W}{F_1 + F_2} \quad (\text{Eq. 2.2.1})$$

The function $E(t)$ or residence time distribution (RTD) for a single fluidized bed, which is seen as a perfectly stirred tank reactor, is [37]:

$$E(t) = \frac{1}{\tau} * e^{-t/\tau} \quad (\text{Eq. 2.2.2})$$

and describes the fraction of solids staying in the bed in the interval between t and $t + dt$. [37]. Looking at a multistage fluidized bed system (MStFB), one can see the multiple control volumes are present. The possible arrangement of the individual stages is shown in *Figure 2.14*. In [*Figure 2.14. (a)*] a countercurrent MStFB – column, as used in this work, is shown. The fluidization agent flows from bottom to top, while the bed material flow downwards, counter-currently to the gas-flow. However, it should be noted that a MStFB- system is not limited to countercurrent systems, even though they are commonly used thanks to their low space requirement. In [*Figure 2.14. (b)*], a crossflow MStFB system can be seen.

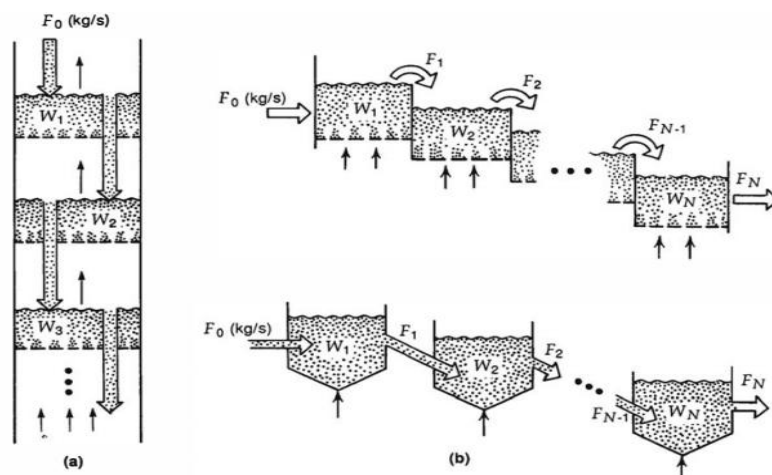


Figure 2.14. Multistage fluidized bed operations, (a) counter- and (b) crossflow operations. [37]

With the assumption that a cascade of ideally stirred tank reactors, with N reactor-stages and a mean residence time (τ_i) in each tank, is used as a model for the calculation of the residence time distribution of multistage bed systems, the equation is obtained [37]:

$$E(t) = \frac{1}{(N-1)! * \tau_i} * \left(\frac{t}{\tau_i}\right)^{N-1} * e^{-t/\tau_i} \quad (\text{Eq. 2.2.3})$$

The mean residence time of solids in each stage (τ_i) is defined as:

$$\tau_i = \frac{W_i}{\dot{m}_s} \quad (\text{Eq. 2.2.4})$$

Figure 2.15., shows the RTD in a multistage fluidized bed. As can be seen, the RTD of multistage bed systems can be improved by increasing the number of stages. Conclusively, the distribution is narrower the more stages are used.

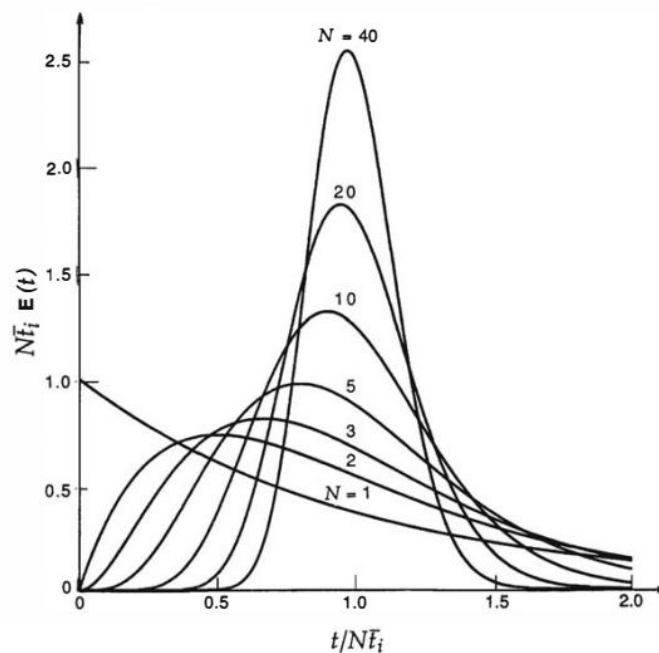


Figure 2.15. Exit age distribution (RTD) for solids in ideal multistaged fluidized beds [37]

On account of this advantage, multistage fluidized bed systems are used in many applications. As can be seen in Figure 2.16, there are various possibilities of designing multistage fluidized beds. In [Figure 2.16 (a)] a multistage bed system with an internal moving bed standpipe is pictured, where the stages are placed above each other. Through the standpipe, material is fed from the upper stage to the lower one. In [Figure 2.16. (b)], a multistage reactor with a countercurrent solid flow is shown, like commonly used as a dryer. In [Figure 2.16. (c)] a MStFB system is shown which was also used in this work, namely, with external downcomers. The downcomers can have

different constructions and different transport mechanisms, which are briefly explained in chapter 2.2.3. The main advantage of this design with external downcomers, is the fact, that no volume of the fluidized bed is used for the transport since they are located outside. Furthermore, the advantage of external downcomers is the solid height regulation in the downcomer during start up and shut down, as well as during operation.

As shown in [Figure 2.16. (d)], the fluidized bed stages can be arranged side by side and separated by weirs, via which solids are transferred from one stage to the next. The notable disadvantage of this construction is the high amount of fluidizing agent required to achieve the required solid transport since the each stage needs to be fluidized by an individual gas flow. The most common designs are those, where the stages are built on top of each other. The structure is similar to a rectification column as used in the distillation of petroleum. In addition to these examples there are many more used in process engineering. For example: fluidized beds with online solid exchange, spouted bed and even centrifugal fluidized beds [65].

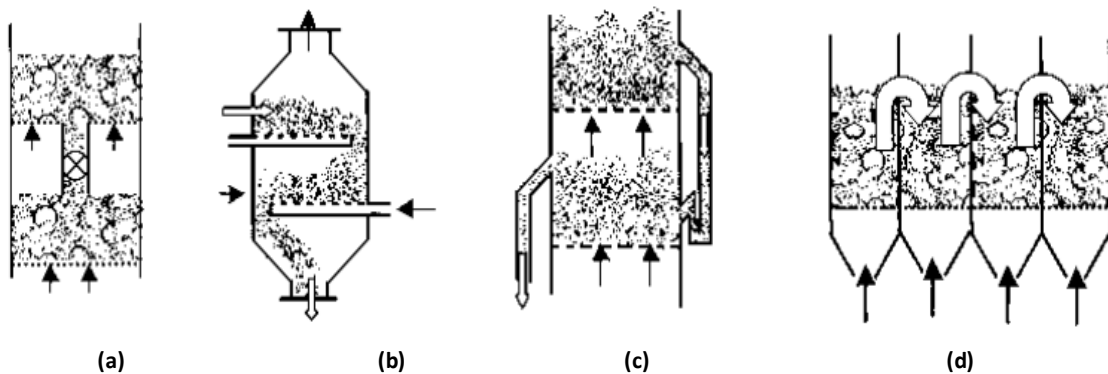


Figure 2.16. Variations of fluidized bed reactor configurations. (a) multi-stage bed, (b) multi-stage with countercurrent solid flow (c) multi-stage with external solid circulation (d) multi-cell bubbling bed [65]

2.2.2. Gas distributor designs

The gas distributor (also referred to as a grid) in a fluidized bed reactor is designed to induce uniform and stable fluidization over the entire bed cross section, over long periods (years) without clogging or breaking, and supports the weight of the bed material during start-up and shut down. There are a variety of distribution plates including: perforated plates, bubble cap, conical grids, and sparger [51]. The choice depends on the process conditions, mechanical workability, and of course on the costs.

For the cold flow model perforated plates (Figure 2.17.) were used with a triangular pitch. The main advantages of perforated plates are the easy manufacturing, the low costs and the possibility to change the hole size easily.

The main advantages of bubble caps (Figure 2.18) are the excellent turndown ratio and the low pressure drop. Notwithstanding, they have some disadvantages like the high costs, stagnant regions are difficult to avoid and they are difficult to modify and clean.

A sparger (Figure 2.19) is commonly used in thermal processes, due to the fact of undergoing thermal expansion without damage. Furthermore, a sparger enables a low pressure drop as well as a good solid flow from above the grid to below. On the basis of the mechanical design, they prohibit a simple modification and lead to defluidized solid regions beneath the grid.

In systems where an excellent solid mixture is required, conical grids (Figure 2.20) can be used. Due to their design they prevent stagnant solid buildups and minimize solid segregation. Even if they promote good solid mixtures, the disadvantages like the high pressure drop required and the difficult construction making them useless for this work [51].

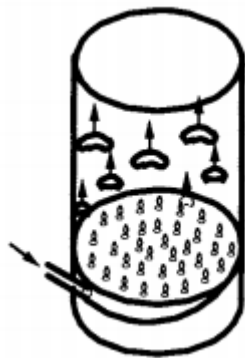


Figure 2.17. perforated plate [51]

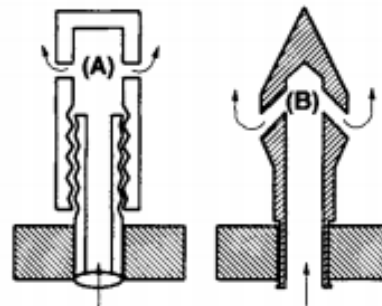


Figure 2.18. bubble caps [51]

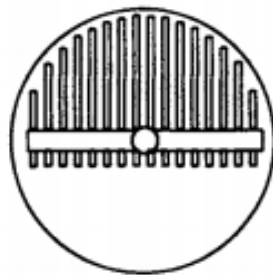


Figure 2.19. sparger [51]



Figure 2.20. conical grids [51]

An adequate gas distributor design is required for all fluidized bed systems. In order to allow uniform gas distribution, a certain pressure drop across the distributor plate is necessary to exceed or equal the maximum value of any unsteady-state pressure fluctuation. According to Agarwal et al [2] the pressure drop for stable operation of a fluidized bed should be in the range of:

$$\Delta p_{distr} = (0.1 - 0.3) \cdot \Delta p_{bed} \quad (Eq. 2.2.5)$$

This range is a rule of thumb. It should be kept in mind, however, that several investigators have found the ratio of distributor pressure drop to bed pressure drop to be in the range of 0.015 to 0.4 [51]. Generally, the pressure drop across a perforated plate is determined as a function of the gas velocity inside the orifice of the distributor plate $U_{g,or}$, the density of the gas ρ_g and the resistance factor of an orifice ζ :

$$\Delta p_{distr} = \zeta \cdot \frac{\rho_g \cdot U_{g,or}^2}{2} = \frac{1}{C_d^2} \cdot \frac{\rho_g \cdot U_{g,or}^2}{2} \quad (Eq. 2.2.6)$$

The orifice discharge coefficient C_d is typically about 0.6 for a gas flowing through an orifice in a pipe, and for a grid hole, the coefficient is about 0.8. The value of C_d depends on the grid plate thickness and the hole pitch, as can be seen in *Figure 2.21*. [51]

In *Figure 2.22*, two different designs of pitches can be seen, whereas the triangular pitch was used for this work since this arrangement provides a flow favor.

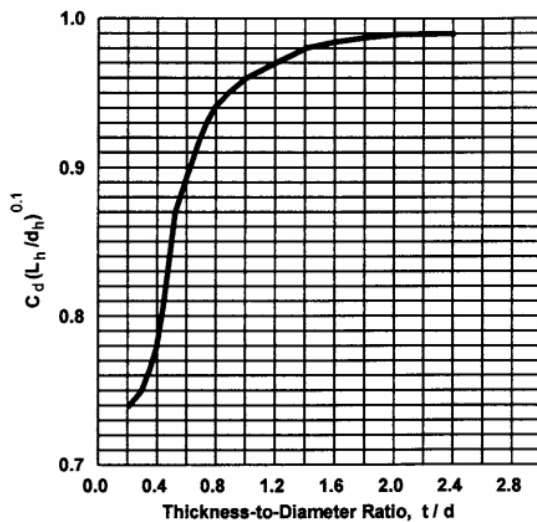


Figure 2.21. Grid hole discharge coefficient design chart [51]

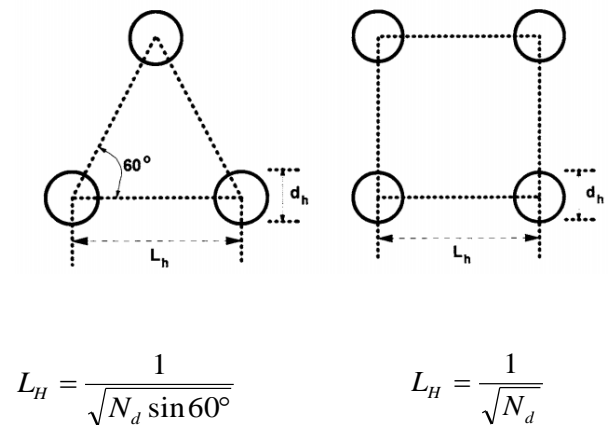


Figure 2.22. The relationship between hole density and grid hole pitch for triangular and square pitch [51]

To increase the gas residence time in the bed, it is recommended to introduce an as high as possible number of gas bubbles, with an as small as possible bubble diameter, into the bed through the holes. A practically proven range of hole sizes should be in the range of three times as large as the particle diameter, to ten times as large. In the case of smaller hole diameters, the particles often block the hole.

$$3 \cdot d_p < d_{or} < 10 \cdot d_p$$

2.2.3. Downcomer designs

The design of the downcomer is essential for stable operation of the multistage fluidized bed column (MFB-column) [54]. The downcomer has the task of ensuring the material transport between the stages, from an upper zone at low pressure to a lower zone of higher pressure. The fluidization agent tries to flow up the downcomer to the low pressure area but the down flowing solid hinders the fluidization agent. Since larger gradients cannot be maintained, longer downcomers must be used, or a restriction at the bottom and top must be ensured to control the pressure drop [37].

[Figure 2.23. (a)], shows three different configurations for the top of the downcomer. Which one is used depends on how the solid enters the downcomer. [In Figure 2.23.(b)] the various types of flow restriction at the bottom sections, in order to control the pressure drop and flow rate, can be seen. Any variation of top and bottom can be used [37].

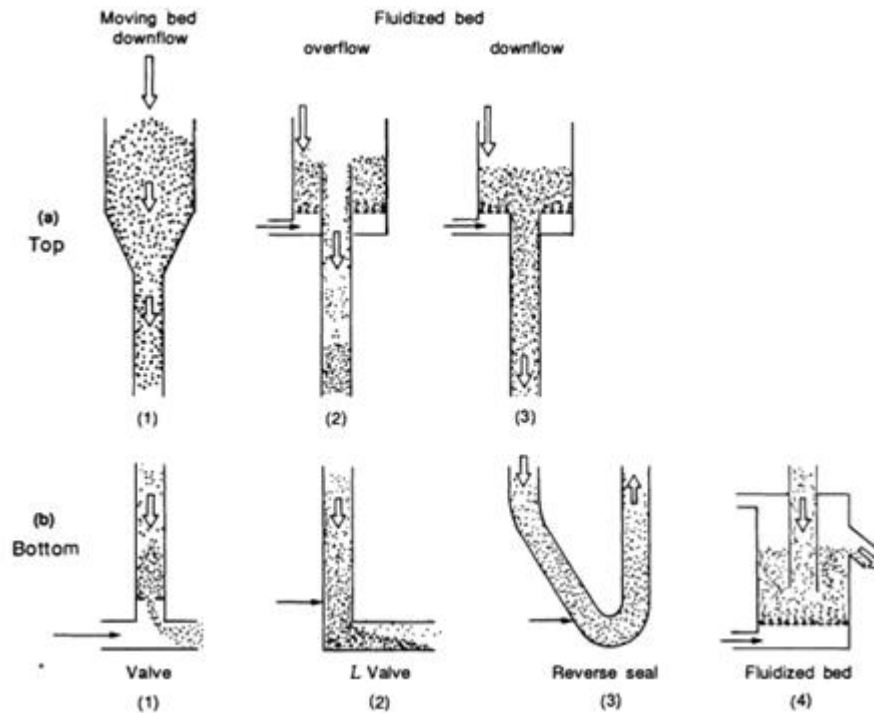


Figure 2.23. Downcomer designs configuration of the top and ends of downcomers [37].

Several studies on the fluid-dynamic behavior of MStFB systems with downcomers exist [45]. In previous studies, overflow standpipes [Figure 2.23.(a-2)] have been used mostly, however in this work a weir plate was used as an internal downcomer, instead of a standpipe. Mohanty et al [45], studied the operating ranges of a counter-current multistage fluidized bed reactor with internal downcomers, in the form of standpipes. As a result of his study, he concluded, that standpipes run between a “lower operation gas velocity”, where solids began to spread and transferred from stage to stage, and an “upper operating gas velocity”, which lead to a decrease of the solid height

in the downcomers and further in instability of the solid flow. As the solid flow rate increases, the range of stable operation decreases, therefore, no standpipes were used in this work since a high solid flow is desired. A proper design of downcomers is important to enable a stable down flow of solids. The solids can be easily disturbed by gas bypassing and slugging, which leads in MStFB-columns to the phenomena, that one stage overfills through the clogged downcomer, while the next stages are practically empty [37].

For stable operation the pressure drop across the fluidized bed formed within the downcomer can be written as:

$$\Delta p_{dc} = 2 \cdot \Delta p_{bed} + \Delta p_{distr} \quad (\text{Eq. 2.2.7})$$

Already in 1978 Eleftheriades and Judd [15] studied the influence of the solid mass flux on the solids flow regime within a downcomer for different superficial gas velocities within a two staged fluidized bed system, with the result that if solid mass flux is increased steadily, a moving bed regime within the downcomer can be preserved even at superficial gas velocities above the minimum fluidization velocity of the bed material. Further increase of the superficial gas velocity led to a switch point, where the moving bed regime turns into a fluidized regime, depending on the size of the downcomer. With the assumption that a fluidized bed regime exists within the downcomer, the pressure drop along the downcomer can be expressed as:

$$\Delta p_{dc} = H_{s,dc} \cdot (1 - \varepsilon_{dc}) \cdot (\rho_s - \rho_g) \cdot g \quad (\text{Eq. 2.2.8})$$

One can assume that gas velocities within the bed stage and the downcomer section are equal, if the downcomer is operated at a stable fluidized regime point, hence, the voidages can be considered as equal, since the voidage in bubbling fluidized bed only depends on the gas velocity. This assumption does not apply to slugging phenomena [40]. The bed voidage can be calculated using for instance the correlation given by Hsiung and Thodes [26]:

$$\varepsilon = \varepsilon_{dc} = \varepsilon_{bed} = \varepsilon_{mf} \cdot \left(\frac{\text{Re} - b'}{\text{Re}_{mf} - b'} \right)^{0.28} \quad (\text{Eq. 2.2.9})$$

Where the constant b' is defined as:

$$b' = 0.216 \cdot \text{Re}_{mf}^{1.2} - 0.35 \quad (\text{Eq. 2.2.10})$$

The downcomer pressure drop will attempt to fulfill Eq. 2.2.7 and Eq. 2.2.8 during operation by adjusting the solid bed height $H_{s,dc}$ and holding the following equation $H_{s,dc} \leq H_{dc}$. (In the case of $H_{s,dc} = H_{dc}$: the pressure drop across the downcomer reaches a maximum, and a stable operation

can no longer be guaranteed) [40]. Considering the dense phase height in the downcomer as the active height, the estimation of the minimum downcomer height can be expressed using the weir height H_w . By merging the above equations, the downcomer solid height can be calculated from:

$$\Delta H_{s,dc} = 2 \cdot H_w + \frac{\Delta p_{distr}}{(1 - \varepsilon) \cdot g \cdot (\rho_s - \rho_g)} \quad (\text{Eq. 2.2.11})$$

As a consequence, a large downcomer height is necessary to provide a stable operation [54]. However, unnecessary large downcomers increase the freeboard height, which are free of solid material and thereby inactive in a thermal process.

3. Methodology

3.1. Experimental setup

Cold flow modeling is an important tool in process design. Cold flow models (CFM) are used for designing and upscaling fluidized bed systems [23]. As can be seen in *Figure 3.1.*, the way to a performing full-scale unit is based upon a system. At the beginning of a scaling procedure, the screening procedure must be done. The screening process, whose purpose is the identification of the parameters, often require mathematical models. As soon as the conditions are generally fixed, a Lab- scale unit , can be designed. The next larger scale is a bench scale unit. After gaining information and experience, the next step is a scale up to a pilot scale unit. Fluidized bed processes are highly scale-dependent, and therefore it is difficult to predict the behavior of industrial-scale reactors from simple evaluation. For this reason, the cold flow model used in this work was designed after the TSA-BSU (see Chapter 1.) went in successful operation, in order to simulate the planned pilot scale unit. The scaled model is an experimental model which is often smaller than the original plant, generally built out of transparent material to allow a direct view on the gas-solid-movement inside the unit. The advantage of a CFM is the reduction of risk, associated with construction of large pilot-scale or even full scale units. The precondition of such a cold flow model is that the hydrodynamic phenomena which occur in the unit are similar to those expected for the hot, full-scale reactor. They operate at ambient temperature, but with the same hydrodynamic behavior, and usually fluidized with air.. Although the idea of scaled cold flow models has been successfully employed many times over the past decades, the proper construction and scaling of a cold flow model is still one of the most challenging aspects of fluidization technology. The scaling of hydrodynamic systems is done with the aid of dimensionless parameters which must be kept equal at all scales in order to be hydrodynamically similar [60].

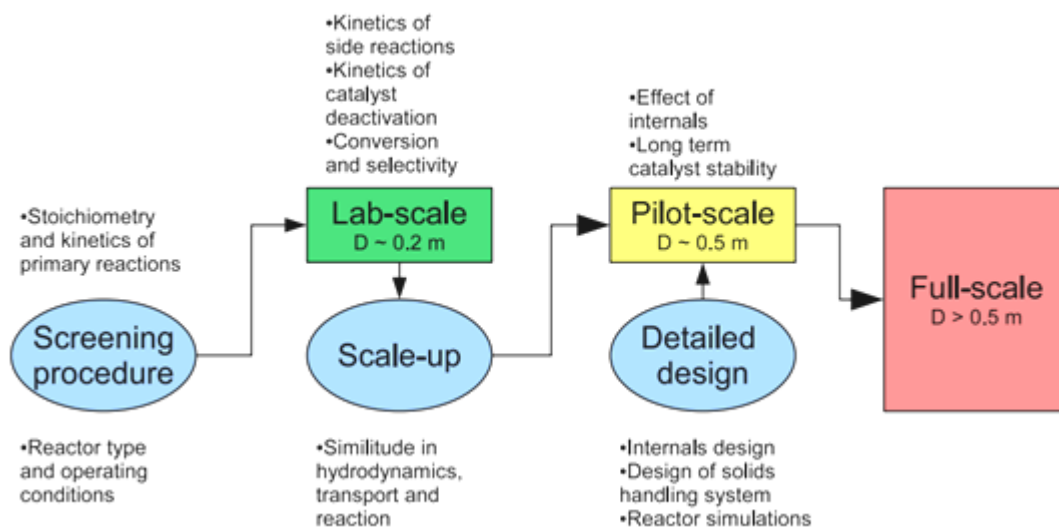


Figure 3.1. Scale up procedure to establish an industrial full-scale catalytic fluidized bed reactor [60]

Scaling relationships by Glicksman

The fundamental idea for deriving scaling laws by empirical analysis was made by Fitzgerald and Crane [58] who claimed that “in principle the motion of a system of particles suspended in a fluid is completely determined by the Navier–Stokes equations with the corresponding continuity equation and the Newtonian equation of motion of each particle to be satisfied at each point of the fluid” Based on this hypothesis, Glicksman [20] deduced the “full set” scaling laws from the reflection that the scaled model has to follow the same equations and boundary conditions as the hot plant. Therefore, he non-dimensionalized the governing equations, which are the conservation of mass, and the equation of motion for fluid and solid phases by Anderson and Jackson [59] with their boundary conditions and the Ergun equation [16]. Furthermore, he assumed the fluid as incompressible and the inter-particle forces are neglected. To reduce the number of fixed parameters, Glicksman et al. [20] modified the full set of scaling laws by simplifying the Ergun equation for situations where the fluid-particle drag is either dominated by viscous forces or by inertial forces. In order to simplify the up-scaling, Glicksman et al. [20] concluded the “simplified set of scaling laws” (Table 3.1.) The simplified set relaxes the constraints on the dimensions of the small-scale reactor and gives a greater flexibility in the reactor design. While the “full set” of scaling laws, takes the ratio between the particle diameter d_p and the reactor diameter D into account, this ratio is for simplified set omitted. Furthermore, the Reynolds number from the “full set” is replaced by the dimensionless fluidization number. Through this simplification, two additional degrees of freedom in the design of the CFM are obtained.

The CFM used in this work, was designed at the TU Vienna, according to these “simplified set of scaling laws” and represent the Adsorber column of the TSA-PSU (Chapter 1.3). Further, it can be used for various fluid dynamic studies.

Table 3.1. Simplified set of Scaling laws by Glicksman [20]

Dimensionless number	Equation (Eq.3.1.1-3.1.6)
Froude number	$Fr = \frac{U_0}{\sqrt{g * d_p}}$
Ratio of fluid to solid density	$\frac{\rho_s}{\rho_f}$
Sphericity	$[\varphi]$
Particle distribution	PSD
Fluidization number	$\frac{U}{U_{mf}}$
Ratio of bed diameter to bed height	$\frac{D}{H}$

3.1.1. Cold flow model setup

In *Figure 3.2.*, a basic scheme of the cold flow model used is shown. The cold flow model (CFM) in *Figure 3.2.* serves as the testing unit of the fluid-dynamic behavior of a multistage fluidized bed system with internal solid circulation, and with external downcomers shown in [*Figure 3.6.(b)*].

As can be seen, the individual stages were built one on top of the other, whereby the stages are numbered from the bottom to the top (highest=4, lowest=1). Further, to allow observation during operation, they are built out of transparent material, in this case Perspex. Each individual stage consists of three basic elements, a bubbling fluidized bed [*Figure 3.2. (5)*], a downcomer [*Figure 3.2.(6)*] and distributor plate [*Figure 3.2. (3)*]. The downcomers are the connection between the stages and provide the transport of solids from an upper to a lower stage. The distributor plates are 2mm thick and perforated with 187 holes, with a hole size diameter of 2.3mm in a triangular arrangement.

A... multistage -column B... solids recirculation system

- 1... windbox
- 2... Bottom gas distributor
- 3...perforated plates
- 4...solids inlet
- 5...fluidized bed
- 6...downcomer
- 7...riser windbox
- 8...pneumatic riser
- 9...gas-solid separator
- 10... vessel
- 11... "bubbler"
- 12... dust collector
- 13...screw conveyer

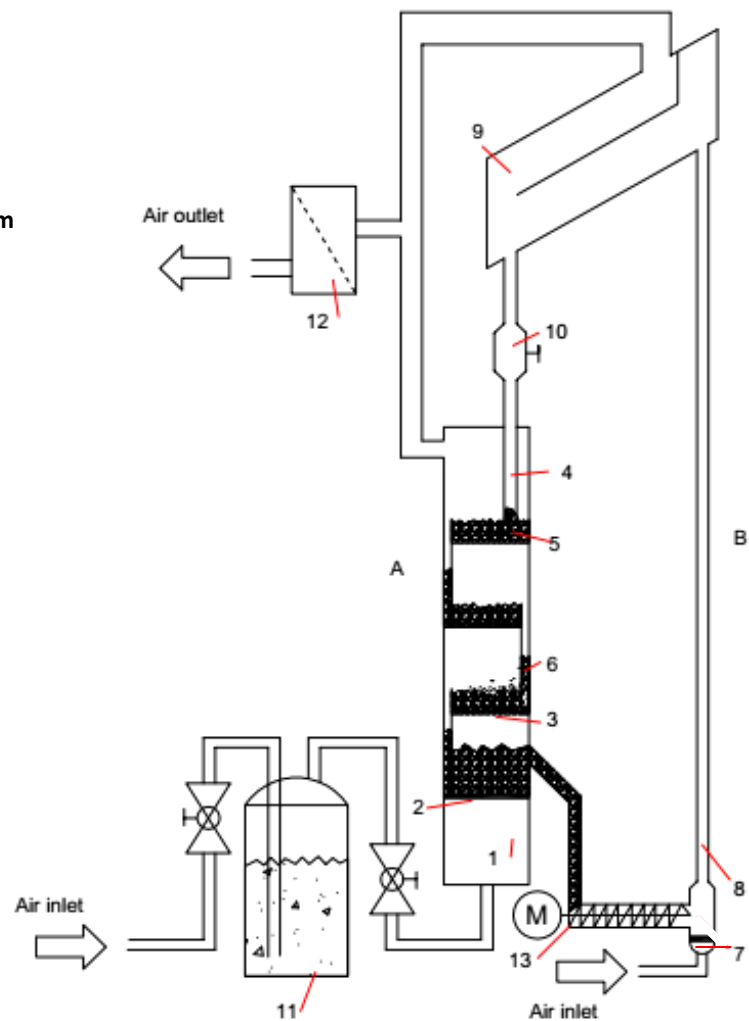


Figure 3.2. Basic scheme of the cold flow model

As early as at the first measurements, it was seen that the bed material was electro-statically charged very quickly by the friction of the particles and the wall friction effects. Electrostatic phenomena arise from the forces that electric charges exert on each other. Such forces are described by Coulomb's law. Even if this effect was known, and for this reason the whole apparatus was grounded, as well as the copper bands and further arrangements, the precautions were still not sufficient to dissipate the electrostatically charge. Each stage was coated inside with anti static-films in order to provide a better view during operation. The actual column is shown in *Figure 3.5.*, whereby the visible copper bands are the grounding of the films and stages. Moisture conditions prevent electrostatic charge generation due to the effect that thin moisture layer accumulating on most surfaces serves to remove electrical charges. Furthermore, with the introduction of vapour, the conductivity of the fluidizing agent is significantly increased. In *Figure 3.3.*, a typical correlation between the relative humidity (%) and the static charge is shown, whereby the relative humidity (RH%) is plotted on the abscissa and the static voltage on the ordinate of the diagram.

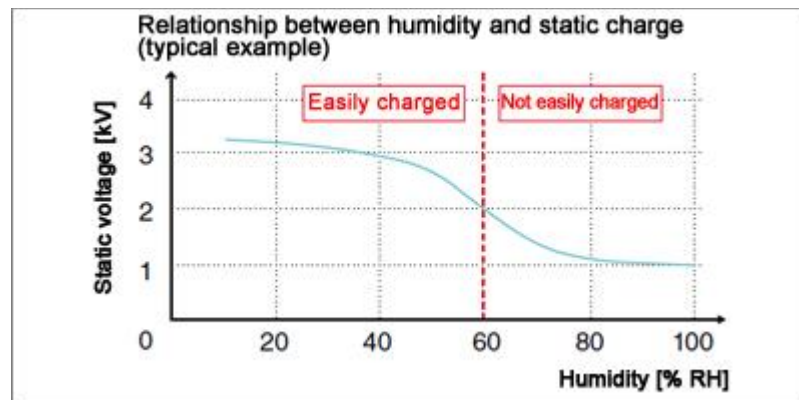


Figure 3.3. Relationship between humidity and static charge [29]

Static charge and humidity are correlated as follows:

If moisture exceeds 60% RH, the static charge is less likely to accumulate. Perrin et al. [39] also came to this conclusion in the investigation of dust explosions and the influence of humidity. Thus the relative humidity had to be increased in the cold flow model of the MStFB-system. This was achieved by passing the fluidization agent, compressed air, through a *bubbler* [Figure 3.2. (1)]. A *bubbler* is a tank which is filled with water. The fluidization agent enters the bubbler at the bottom and had to bubble through the water before the saturated air was then fed into the column. By this measure, the electrostatic charge was significantly reduced.

The windbox [Figure 3.2. (1)] serves as a compensating tank and the bottom gas distributor [Figure 3.2.(2)] has the task to ensure an even gas distribution. Due to the advantageous construction of the bottom gas distributor, the solid from stage 1 cannot trickle into the windbox, since instead of a perforated plates, a plate with nozzles was used. The saturated air is introduced into the

windbox and flows upwards through the column. The column gas feed can be controlled by means of a needle valve.

The used downcomer designs, were a internal (as can be seen *Figure 3.2*) and a external downcomer (as can be seen *Figure 3.4*). An external downcomer consist of an inclined overflow top-part [*Figure 2.20 (a.2)*] and an L-Valve [*Figure 2.20.(b-2)*] as well as an aerated lance in the bottom-part.

Internal downcomers

Bed material enters the column [*Figure 3.2.(4)*] at the highest stage. From there on, it flows counter-currently to the fluidizing gas, through each stage and their individual stationary bubbling beds, through downcomers, down to the lowest stage (Stage=1). In the downcomers, flaps are assembled, as they facilitate the starting process. Internal downcomers need an active control of the empty downcomer pressure drop by means of flaps, otherwise, the fluidization agent will prefer flowing through the empty downcomers. This phenomena finally led to defluidization of the overlying stage Later experiments were carried out without these flaps. After the solid reaches stage 1, it flows in a moving bed regime and is taken out via a screw conveyer [*Figure 3.2.(13)*]. The bottom screw conveyer transports the solid to the riser [*Figure 3.2.(8)*], where the solid is subsequently transported pneumatically to the separator that is situated above the MStFB column [*Figure 3.2.(9)*]. The gas feed of the riser [*Figure 3.2.(8)*] can also be adjusted via a needle valve and a rotameter. Immediately after the separator, a vessel for measuring the solid circulation rate is installed [*Figure 3.2.(10)*] (See *Chapter 3.2.3*). The solid inlet line can be easily disconnected, which means the bed material can either be fed into the column or into a storage hopper. The storage hopper has the advantage of allowing the feeding of the bed material from the hopper into the system also during operation, as well as emptying the column. During operation, the hopper can be isolated from the rest of the CFM through ball valves and has no effect on the operation.

External downcomers

Considering its structure [*Figure 3.6 (b)*] it is possible to differentiate in three components. An inclined part serving as a slide, as well as a vertical and a horizontal part, which serves as a L-Valve. The cold flow model with external downcomers had the advantage of the total usable cross section in each stage, but the disadvantage of a separate required aeration. As external downcomers, pipes with a diameter of 25mm are used. These pipes were attached from the outside. The aerated lance [*Figure 3.4*] is perforated in order to fluidize the solids in the bottom section (Comparable to [*Figure 2.20 (b-4)*]). In contrast to the aerated lance, an L-Valve aerates the vertical part only, whereas the horizontal part is in moving bed regime, driven by the mass of solids.

Thanks to the simple construction of the external downcomers, it was possible to switch between lance and L-Valve by replugging the air supply. The remaining constructive and functional layout does not differ from the one of the CFM with internal downcomers.

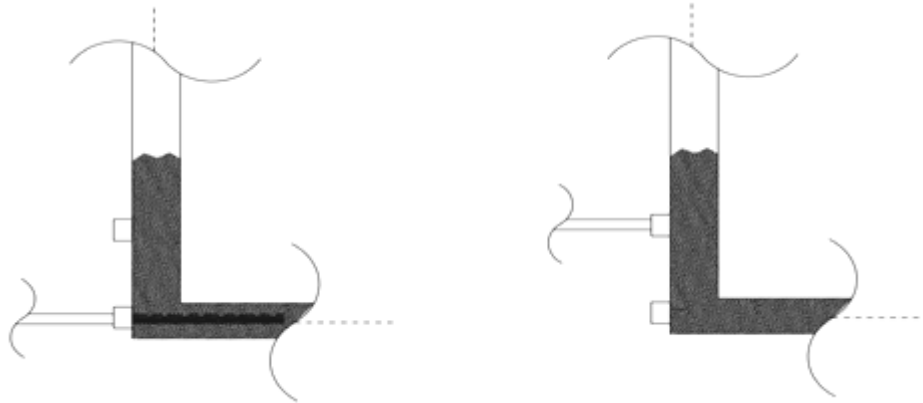


Figure 3.4. Basic scheme of the lance and L-Valve

In conclusion, the solid circulation rate is limited to the rotational speed of the screw conveyor, which depends on the adjusted frequency.

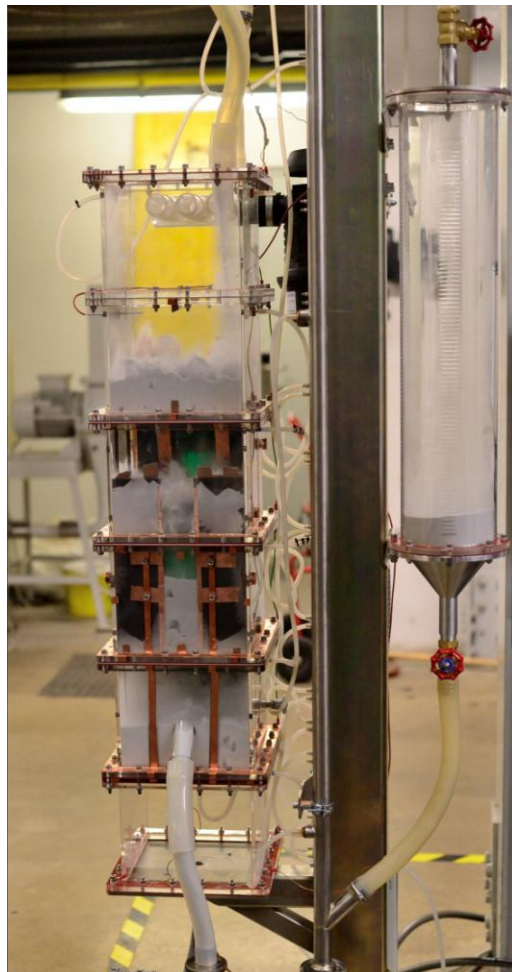


Figure 3.5. Picture of the cold flow model

3.1.2. Measuring equipment

The CFM is equipped with twelve differential pressure gauge, to ensure a continuous monitoring of the pressure drop across the stages. Beneath every distributor plate a differential pressure gauge is installed as well as on the relevant reference points such as the riser pipe or the exit duct. The linearity error for the differential pressure sensors used is less than (or equal to) 1 % of full scale, whereby the used ranges were 0-10mbar, 0-25mbar, 0-50mbar, 0-100mbar and 0-250 mbar. In addition, the process and ambient temperature are recorded using two PT100s. The process temperature was approximate ambient temperature.

[Figure 3.6.] Both, the signals from the differential pressure transmitter and the temperature sensors, are fed into the data acquisition card. From there, the signal is forwarded to a computer and automatically stored.

In order to regulate the flow, a number of rotameters are available, whereby a parallel connection is possible if necessary. All rotameters are connected to the same compressed air supply to ensure the same conditions and have a range between 0-35Nm³/h , 0-9Nm³/h and 0-5Nm³/h. These rotameters were designed for the use of air as the fluid (dynamic viscosity of air 0,018294mPas at 20°C with a density: 1,293kg/Nm³), at 6 bar (gauge pressure). In the case of external downcomers (Figure 3.5), each downcomer is equipped with an air supply line to enable fluidization (*). The setting of the fluidization for external downcomers was carried out by rotameters with a range of 0-0.2 Nm³/h and 0- 1.4 Nm³/h (dynamic viscosity of air 0,018294mPas at 20°C with a density: 1,293kg/Nm³ at 6 bar gauge pressure).

The bottom screw conveyer rotational speed, and thus also the solid circulation rate between the column and riser, are controlled by a frequency converter, with a range of 0-230 kg/h at 0-100Hz.

Table 3.2. Measuring Units of the cold flow model

function	number	name	manufacturer	Type	measuring range	power supply	Output
FCI	100	rotameter	KROHNE				
PDI	101	differential pressure transmitter	KALINSKY Sensor Elektronik	DS 2-420	0-50mbar	24VDC	4....20mA
PI	102	differential pressure transmitter	KALINSKY Sensor Elektronik	DS 2-420	0-250mbar	24VDC	4....20mA
TI	103	temperature sensor				24VDC	4....20mA
FCI*	111	rotameter	KROHNE				
PDI	112	differential pressure transmitter	KALINSKY Sensor Elektronik	DS 2-420	0-25mbar	24VDC	4....20mA
FCI*	122	rotameter	KROHNE				
PDI	123	differential pressure transmitter	KALINSKY Sensor Elektronik	DS 2-420	0-25mbar	24VDC	4....20mA
FCI*	133	rotameter	KROHNE				
PDI	134	differential pressure transmitter	KALINSKY Sensor Elektronik	DS 2-420	0-25mbar	24VDC	4....20mA
PI	140	differential pressure transmitter	KALINSKY Sensor Elektronik	DS 2-420	0-10mbar	24VDC	4....20mA
PDI	145	differential pressure transmitter	KALINSKY Sensor Elektronik	DS 2-420	0-10mbar	24VDC	4....20mA
FCI	150	rotameter	KROHNE				
PDI	151	differential pressure transmitter	KALINSKY Sensor Elektronik	DS 2-420	0-250mbar	24VDC	4....20mA
PDI	152	differential pressure transmitter	KALINSKY Sensor Elektronik	DS 2-420	0-50mbar	24VDC	4....20mA
PDI	153	differential pressure transmitter	KALINSKY Sensor Elektronik	DS 2-420	0-50mbar	24VDC	4....20mA
PDI	154	differential pressure transmitter	KALINSKY Sensor Elektronik	DS 2-420	0-25mbar	24VDC	4....20mA
PDI	155	differential pressure transmitter	KALINSKY Sensor Elektronik	DS 2-420	0-10mbar	24VDC	4....20mA
SCI	156	Frequency converter	Huanyang Electronics Co.,LTD	HY00D423B	0-100Hz	230V/ 50Hz	

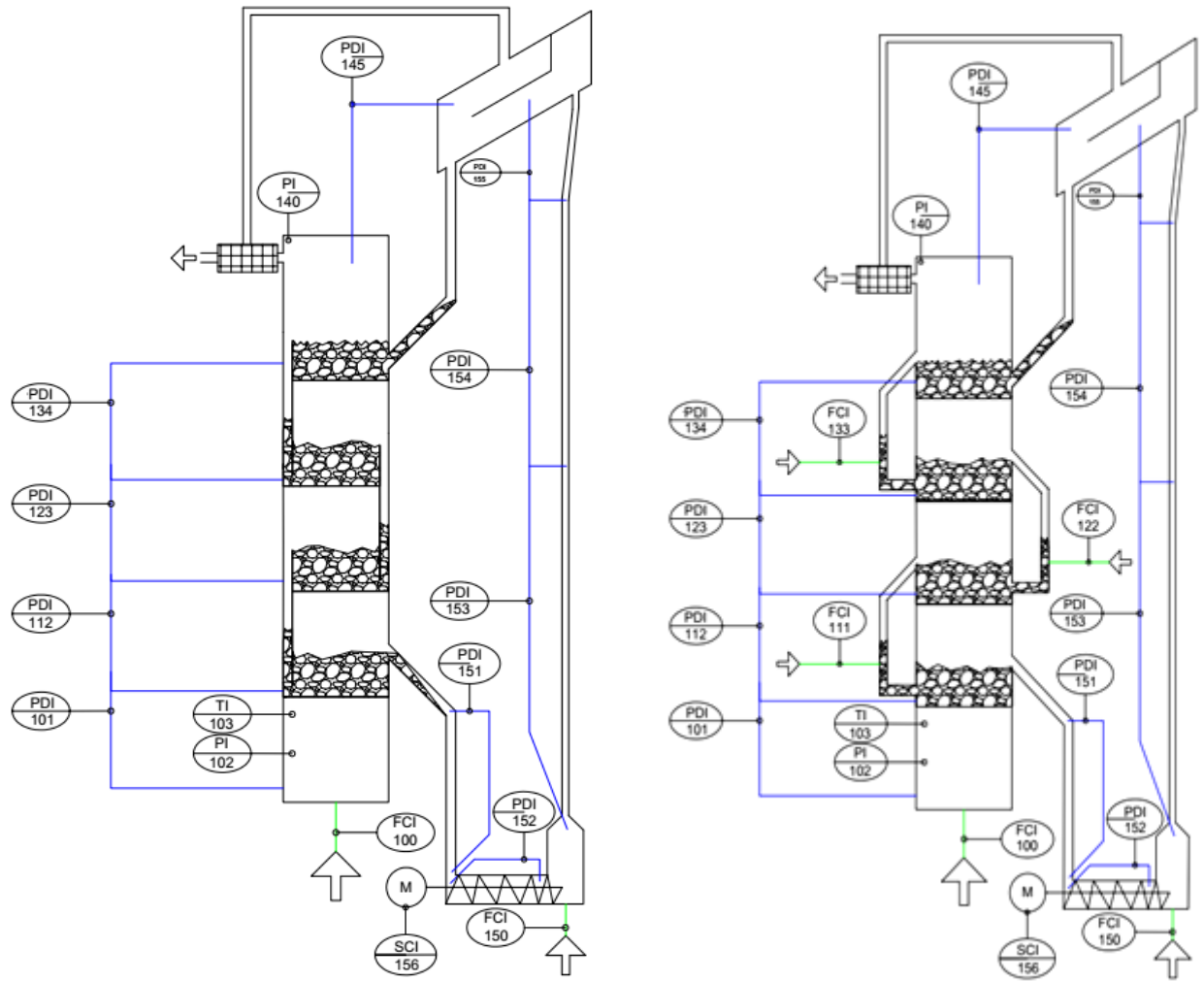


Figure 3.6. P&ID scheme of the CFM with (a) internal downcomers and (b) external downcomers

3.2. Determination of the bed material properties

3.2.1. Characterization of the bed material

The bed material, the glas beads, used for this experiment were analyzed as follows. The particle size distribution and particle diameter were measured by laser diffraction (via a Malvern MasterSizer 2000, report in Appendix). The analysis of the glass beads indicated a mean particle size $d_{p,m}$ of 157.42 μm and a Sauter diameter d_{sv} of 149.64 μm .

In this case, the density was measured with the aid of a measuring cylinder, with a known volume of 433 ml. The measuring cylinder was filled with partides till a heap was formed above the edge. Afterwards, the heap is pulled off, so that the exact volume is filled. The mass is obtained by simple weighing

$$\rho_b = \frac{M}{V_{\text{measuring cylinder}}} = \frac{624.3}{433} * \frac{g}{mL} = 1.442 \text{ g/cm}^3 \quad (\text{Eq. 3.2.1})$$

After the density is calculated, the voidage can be estimated according to Eq. 2.1.8

$$\varepsilon_{mf} = 1 - \frac{V_p}{V_{FB}} = 1 - \frac{\rho_b}{\rho_p} \approx 1 - \frac{1.442}{2.5} \approx 0.4232$$

Taking into account the densities at ambient conditions of the partides (approximately $\approx 2500 \text{ kg/m}^3$) and the fluid (approximately $\approx 1.25 \text{ kg/m}^3$), it can be seen in Figure 2.4., that these particles belong to Geldart group B of partides.

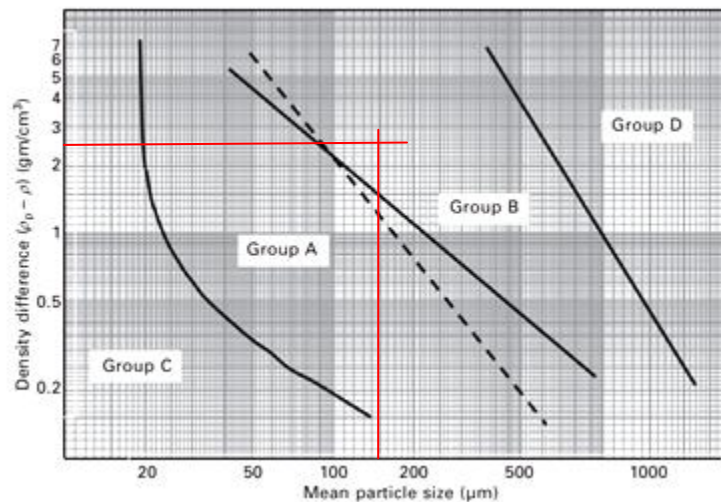


Figure 2.5. Geldart classification of particles for air at ambient conditions [52]

3.2.2. Determination of the minimum fluidization velocity – U_{mf}

The minimum fluidization velocity U_{mf} was determined experimentally by the following experiment.

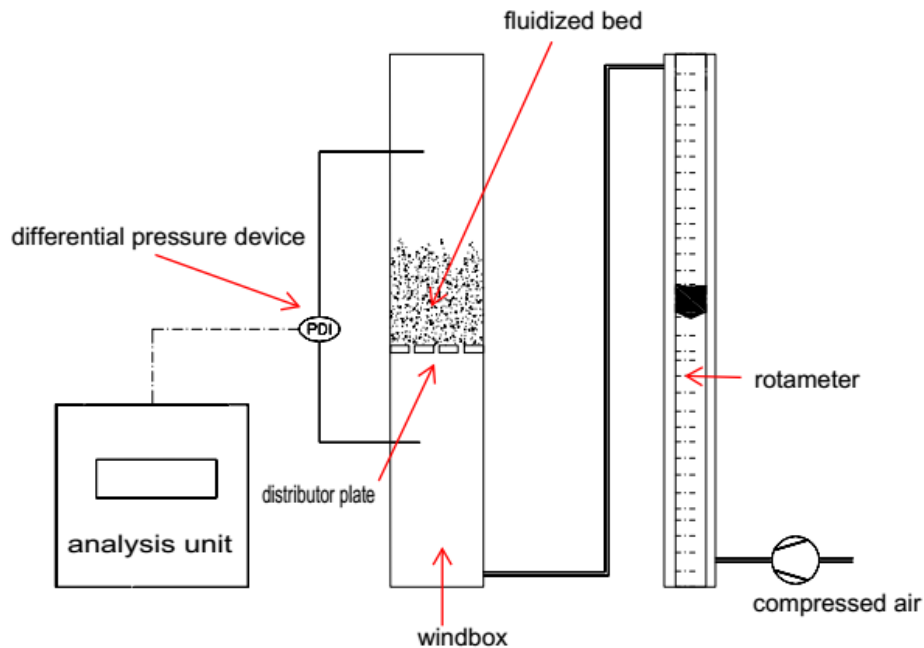


Figure 3.7. Measurement equipment- Determination of the minimum fluidized velocity

As shown in *Figure 3.7*, a sample tube with a distributor plate was filled with bed material until a layer about 2 cm high was present. As already shown in Chapter 2.1.6., the minimum fluidization velocity nearly independent of mass. Subsequently, the bed material was fluidized with air, and the volume flow was gradually controlled by means of a rotameter in the same steps, till a volume flow of $0.40\text{Nm}^3/\text{h}$, then vice versa from the maximum possible volume flow downwards in order to avoid measurement errors. The differential pressure device measures the pressure drop across the distributor plate and the fluidized bed. In order to obtain the pressure drop across the fluidized bed, the pressure drop across the distribution plate was first measured and then subtracted from the total pressure drop in the calculation.

The volume flow was converted into the superficial velocity by considering the cross area of the empty tube. Using the measured and acquired data, *Figure 3.8* was plotted, whereby the superficial gas velocity is plotted on the abscissa and the bed pressure drop on the ordinate.

By dividing the graph, into a linear course of the pressure drop in the fixed bed, and an almost constant course in the fluidized bed, a typical correlation between both parameters is obtained. Both ranges are expressed by their linear equation. If the straight lines are extended to an intersection point, both linear equations must be equal at the intersection point. By solving the equation for x , the minimum fluidization velocity is obtained, with a value of $U_{mf} = 0.025$ m/s.

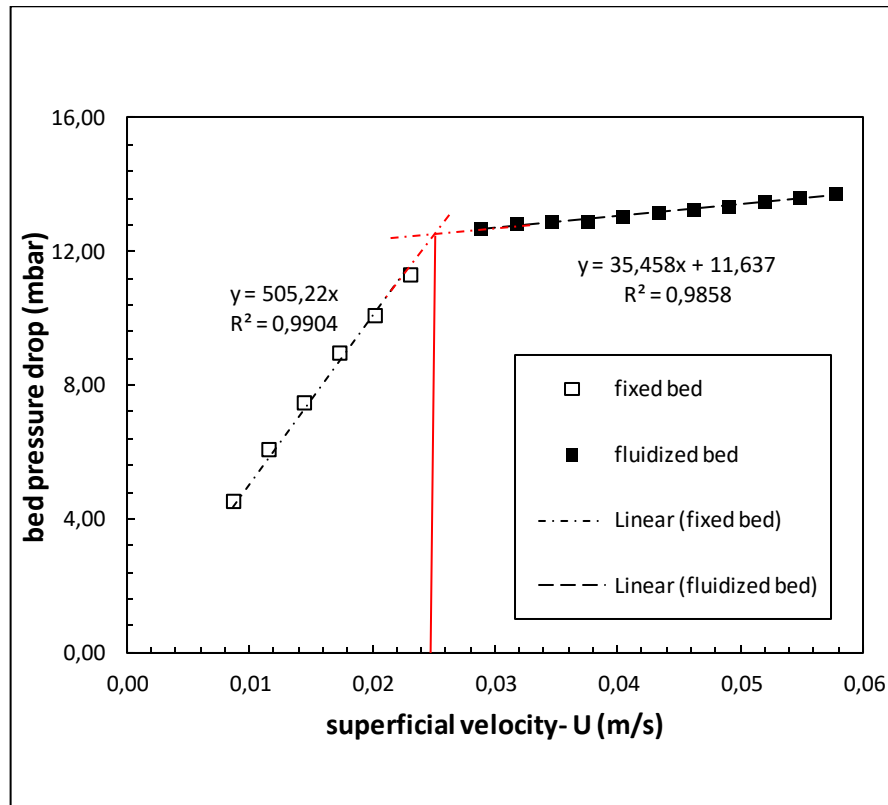


Figure 3.8. U_{mf} glas beads 100-200µm as recieved

In order to compare to the result, the following calculation is based on the equation according to Grace (Eq. 2.1.22., Chapter 2.1.6):

Table 3.3. Results - U_{mf} glas beads 100-200µm as recieved

Glas beads as Received

$$U_{mf} = \frac{\mu}{d_p \cdot \rho_g} \cdot \left(\sqrt{27.2^2 + 0.0408 \cdot Ar} - 27.2 \right) \quad \text{with} \quad Ar = \frac{d_p^3 \cdot (\rho_p - \rho_g) \cdot \rho_g \cdot g}{\mu^2}$$

$$d_p \approx d_{sv} = 149.67 \mu\text{m} \quad \mu_g = 18.1078 \times 10^{-6} \text{ Pa}\cdot\text{s} (20^\circ\text{C})$$

$$\rho_p \approx 2500 \text{ kg/m}^3 \quad Ar = 312.95$$

$$\rho_g = 1.2485 \text{ kg/m}^3 (20^\circ\text{C}/50\text{mbar}) \quad U_{mf,c} = 0.02264 \text{ m/s}$$

By comparing both results, both the experimentally determined value and the theoretically calculated value, a deviation of 8.6% is obtained.

After an operating time of 100 hours the glass beads were measured again, with the test report and the data in the appendix. The data was plotted in Figure 3.7 and a minimum fluidization velocity of 0.0184m/s resulted. According to Grace's equation, the theoretical value was also calculated and there is a deviation of 6.3% based on the experimentally determined value.

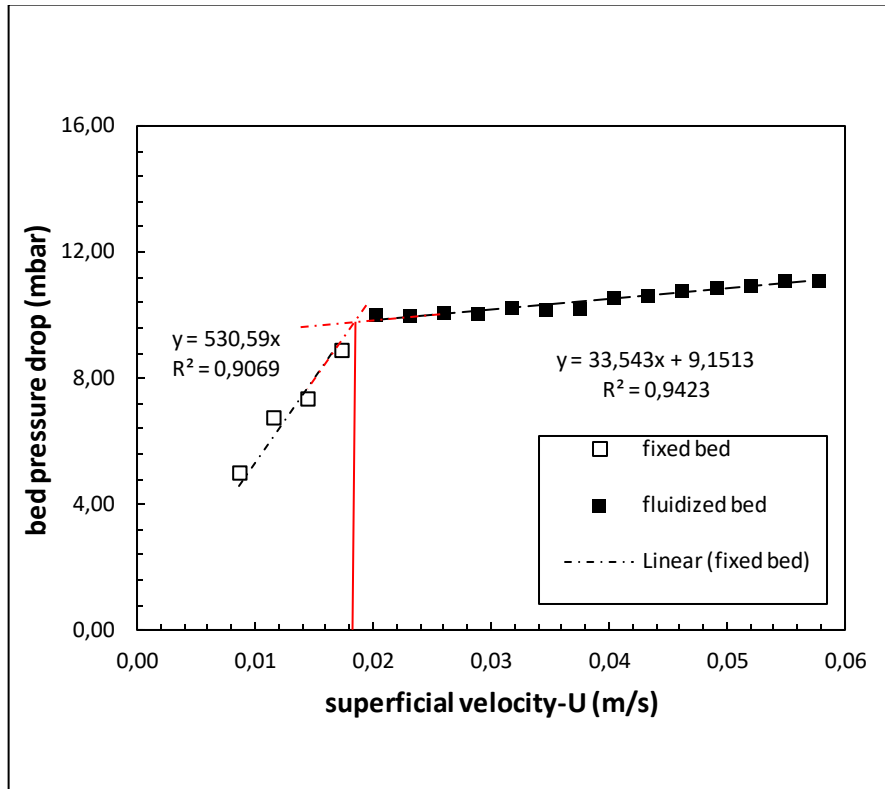


Figure 3.9. Umf glas beads 100-200µm used

Table 3.4. Results - Umf glas beads 100-200µm used

Glas beads used

$U_{mf} = \frac{\mu}{d_p \cdot \rho_g} \cdot \left(\sqrt{27.2^2 + 0.0408 \cdot Ar} - 27.2 \right)$		$Ar = \frac{d_p^3 \cdot (\rho_p - \rho_g) \cdot \rho_g \cdot g}{\mu^2}$	
with			
$d_p \approx d_{sv} =$	130.488µm	$\mu_g =$	18.1078 x 10 ⁻⁶ Pa.s (20°C)
$\rho_p \approx$	2500 kg/m ³	Ar =	207.38
$\rho_g =$	1.2485 kg/m ³ (20°C/50mbar)	U_{mf,c} =	0.01724 m/s

It should be noted, that the minimum fluidization velocity of 0.0172 m / s was always used for the estimation of the fluidizing number. In order to investigate the operation for a broad range of gas velocities, the fluidization numbers were defined as:

6- 8- 10- 12- 14

By considering the cross section area of the column:

$$A = LxH = 0,22m * 0,22m = 0,0484m^2 \quad (Eq. 3.2.3)$$

one obtains a required air volume flow in the column of,

$$\dot{V} = A * U = 0,0484m^2 * \left[\frac{m}{s}\right] * 3600 = m^3/h \quad (Eq. 3.2.4)$$

which must be adjusted by means of the rotameters which are available. The required volumetric flows, as well as the gas velocities from equation Eq.3.2.4 and the fluidization numbers are listed below in Table 3.5. The experiments were carried out on the basis of these volume flows.

Table 3.5. Fluidization numbers and required volume flow

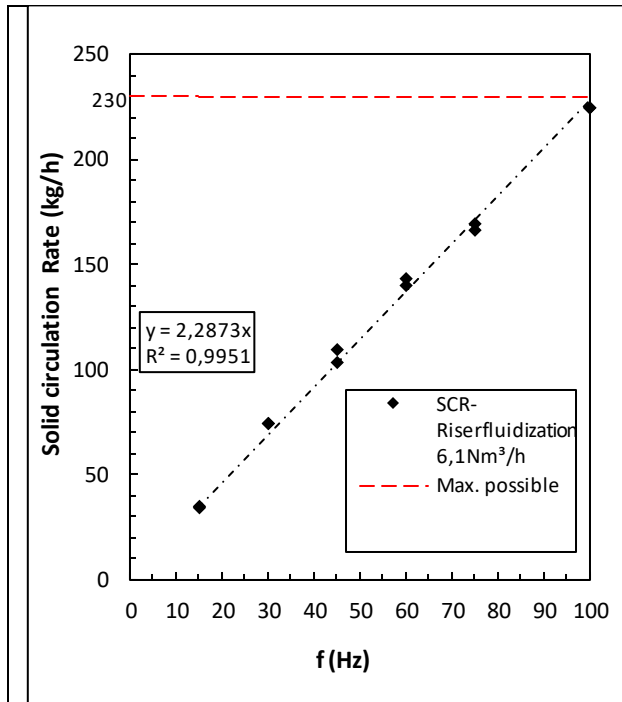
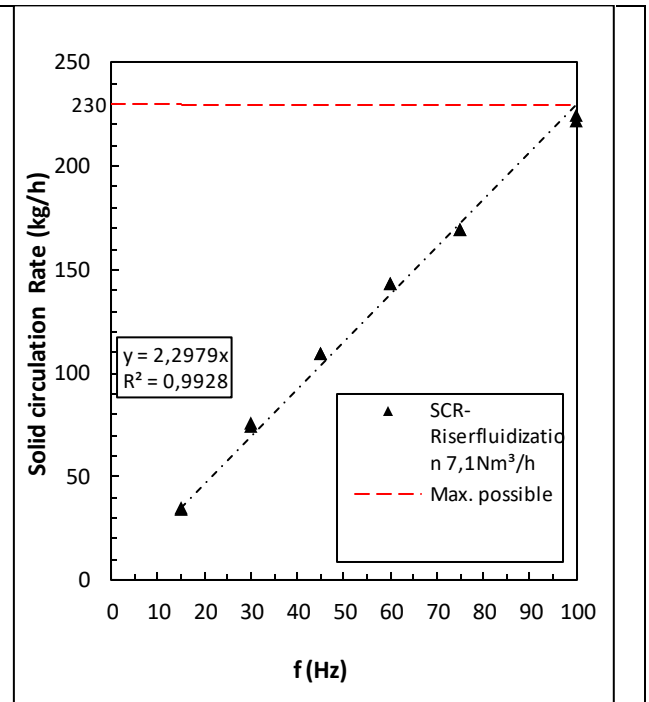
Fluidization number (U/U _{mf})	Superficial velocity U	U _{mf}	Required Volume flow
6	0.1033 m/s	0.0172 m/s	18 Nm ³ /h
8	0.1377 m/s	0.0172 m/s	24 Nm ³ /h
10	0.1722 m/s	0.0172 m/s	30 Nm ³ /h
12	0.2066 m/s	0.0172 m/s	36 Nm ³ /h
14	0.241 m/s	0.0172 m/s	42 Nm ³ /h

3.2.3. Determination of the solid circulation rate

The solid circulation rate (SCR) was determined by means of the vessel from [Figure 3.2 (10)], which has a known volume of 360mL. The column was started, and the frequency of the screw conveyor was adjusted via the frequency converter. After a certain time, when a stable operation was ensured (see Chapter 3.3.2), the valve was closed under the vessel and the time was measured until the vessel was completely filled with bed material. The required time at a certain frequency was listed and the SCR was calculated from the known bulk density of the bed material.

$$SCR = \frac{V_{vessel} * \rho_b}{t_{required}} * 3600 = kg/h \quad (Eq. 3.2.5)$$

The results are shown in Table 3.6., where two different gas velocities were set in the riser. As can be seen in Figure 3.10. and 3.11., the solid circulation rate is independent of the set volume flow (below u_c), so the SCR is only limited by the screw conveyer with a maximum value of approx. 230kg/h. This value is defined as the *maximum possible solid circulation rate* of the system.

Figure 3.10. SCR at Riserfluidization $6.1 \text{ Nm}^3/\text{h}$ Figure 3.11. SCR at Riserfluidization $7.1 \text{ Nm}^3/\text{h}$ Table 3.6. SCR at Riserfluidization $6.1 \text{ Nm}^3/\text{h}$ and $7.1 \text{ Nm}^3/\text{h}$

Measured f (Hz)	6.1 Nm ³ /h Riserfluidization		7.1 Nm ³ /h Riserfluidization	
	time (s)	SCR (kg/h)	time (s)	SCR (kg/h)
15	54	34,56	54	34,56
15	53	35,21	53	35,21
30	25	74,65	25	74,65
30	25	74,65	24,5	76,17
45	17	109,78	17	109,78
45	18	103,68	17	109,78
60	13,3	140,32	13	143,56
60	13	143,56	13	143,56
75	11,2	166,63	11	169,66
75	11	169,66	11	169,66
100	8,3	224,85	8,4	222,17
100	8,3	224,85	8,3	224,85

3.3. Experimental procedure

3.3.1. Cold flow model start up

General start up

The start up of the cold flow model (CFM) was always carried out using a certain procedure. First of all, the data acquisition program is started and all acquired pressure values are set to zero. Normally, all stages are empty, except for stage 1 where the entire bed material is located, since it trickles through the holes of the perforated plates if the fluidization is turned off. At this point, a low fluidization, below U_{mf} , of the column was set via the rotameters and the riser fluidization was adjusted. The screw conveyor is then started at a low frequency and the riser pneumatically feeds the bed material into the separator. Stage 4 started to fill with bed material, but only if the fluidization in the column was high enough to support the weight of the particle layer. Otherwise, the bed material would trickle through the holes in the distribution plates, since the holes have a diameter of 2.3 mm. When the first stage (stage 4) is completely filled, the bed material begins to fall over the weir in the downcomer DC₄₋₃ and starts to fill it followed by a material transport to stage 3.

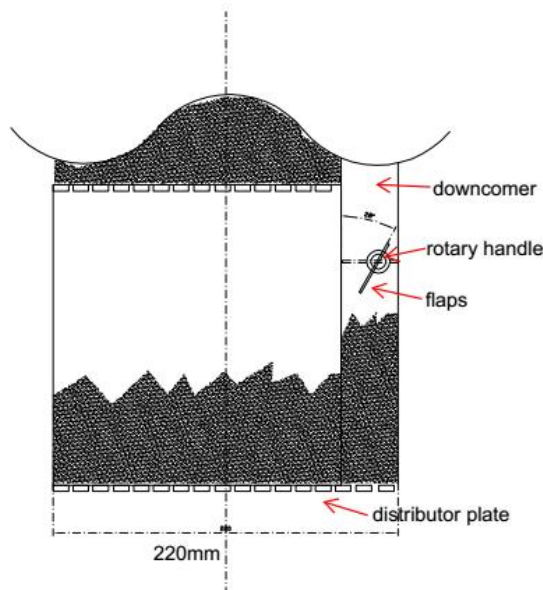


Figure 3.12. Side view-Downcomer with flaps

Internal downcomers

The first experiments were carried out with the flaps inside the downcomer (Figure 3.12). The flaps were closed to generate a pressure drop across the downcomers. The closed flaps cause the fluidization gas to flow through the distributor plates, rather than the downcomer section. Once the downcomer was completely filled, the flap was quickly opened so that the material could slip

into the underlying stage. According to the principle of minimum resistance, the gas tries to flow through the downcomer, since this has been emptied and now provides the lowest pressure drop. For this reason, the flap is closed again and the process is repeated until the stage beneath is appropriately filled with bed material. A stable transport is reached when the solids height in the downcomer reaches a constant value. In this case, the flap can be left open. This step must be repeated for all stages until a stable fluidized bed has formed in each stage.

Later, a method without flaps was developed and applied, but would have a great additional expense, since this method requires a continuous monitoring during start up.

As soon as the first stage (stage 4) was filled, the volume flow was manually reduced so that the bed material began to trickle through the holes of the distributor plate of the fourth stage, but still left high enough that the bed material could not trickle through the distributor plate of the third stage. The higher pressure in the Stage 3 supports the weight of the particles, while the pressure in stage 4 is insufficient to hold up the solids. When the bed material reached the height of the weir, the fluidization was increased again and a fluidized bed was formed in stage 3, which blocked the flow of the gas through the downcomers, but only if enough material was collected in the downcomer before. This procedure had to be carried out repeatedly for all stages, until stable fluidized beds were formed in each stage of the column.

As already mentioned, this method without flaps would be difficult in larger units, since the method requires a constant visual observation.

External downcomers

For experiments with external downcomers the procedure was easier compared to internal downcomers. Through the construction of the bottom section of the downcomers (Chapter 2.2), material remains even after a shutdown in the horizontal section of the downcomer and thus seals the downcomer. In case of the first start up, where they are completely empty, the downcomers can be filled with bed material by a nozzle. As soon as the first stage was filled, the aeration of the downcomers was started at a low aeration. The L-Valve (or lance) enables a transport of the bed material from stage 4 to stage 3. However, a too strong aeration of the downcomers would result in a fast transport. This had to be carried out manually at all stages, under constant observation, until stable fluidized beds were formed in each stage of the column.

After the column had reached a stable operating point, more precisely, if there is a fully formed fluidized bed in each stage, the experiments can be started with different fluidization numbers and a gradually increasing solid circulation rate.

3.3.2. Stable operation

Once the start-up procedure is complete, the tests can be carried out. In the beginning, it is important to define a nomenclature of the experiments since this is used in Chapter 4 below. The basic scheme of the nomenclature is as follows:

1. The first term describes the effective DC- cross area (*Figure 3.14.*) and is defined by its dimensions: length and width (LxW). (see also *Figure 4.1*)
2. The second term describes the material entrance height into the lower stage (*Figure 3.13*)

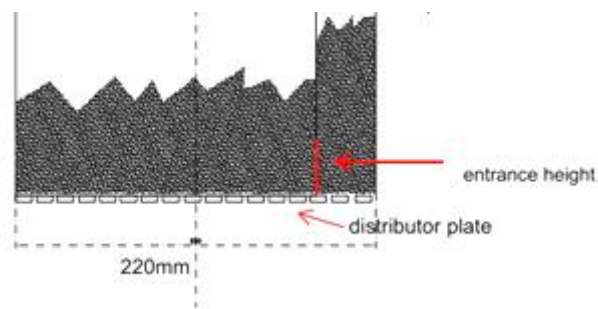


Figure 3.13. Side view of a stage-entrance height

3. The third term describes the gas distributor configuration below the downcomer. As shown in *Figure 3.14*, three different fluidization conditions of the downcomers were investigated:
 - all holes were opened (short description: o, *Figure 3.14*)
 - 50% of the holes were closed, to enable a part fluidization (short description: p, *Figure 3.14*)
 - All holes were closed in order to prevent a primary fluidization of the downcomer (short description: c, *Figure 3.14*)

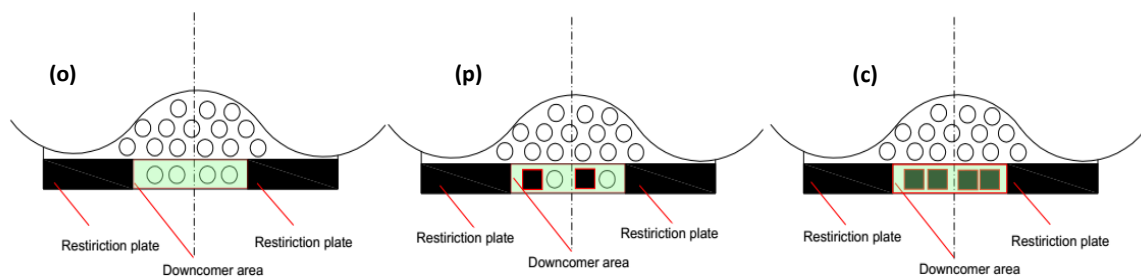


Figure 3.14. Top View of a stage-fluidization conditions

All three terms are interlinked via an underline ().

Table 3.7. Scheme of the nomenclature

1. term	2. term	3. term
DC- Area LxW (mm x mm)	entrance height (mm)	o.... open/p.... part closed/ cclosed
Ex. : 11x66	_30	_o

In this work a stable operation was assumed if a constant course of the pressure drops was recorded over a span of at least 5 minutes, and also only this data was used for the evaluation. The example in *Figure 3.15.(a)* is the actual course of the measurement of the downcomer with the designation 11x66_30_o, with different fluidization numbers and different solid circulation rates. In *Figure 3.15.(a)* typical course of the pressure drop in all 4 Stages can be seen. The jumps in the course indicate a change in the fluidization rate (black vertical lines), the strong increase indicates overfilling of stage 4 at 10:39 when a stable operation at the set SCR was not possible. *Figure 3.15.(b)*, shows an optimal constant course of the pressure drop in all stages at a solid circulation rate of 230kg/h and a set fluidization number of 6. Small fluctuations can be seen, but are negligible. On other hand *Figure 3.15.(c)* shows an example of an unstable operation at a fluidization number of 12 and a solid circulation rate of 200kg/h. If one follows the course of the pressure drop in stage 4, one can see that the downcomer cannot convey the bed material to stage 3, which results in a rapid increase in the pressure drop caused by increase of the solids hold-up in stage 4. Since no bed material is transported, the lower stages are slowly, but proportionally, emptied. At time 10:44 the fluidization was reduced and the circulation stopped which led to emptying of all stages, except stage 1, which now started to fill as the bed material.

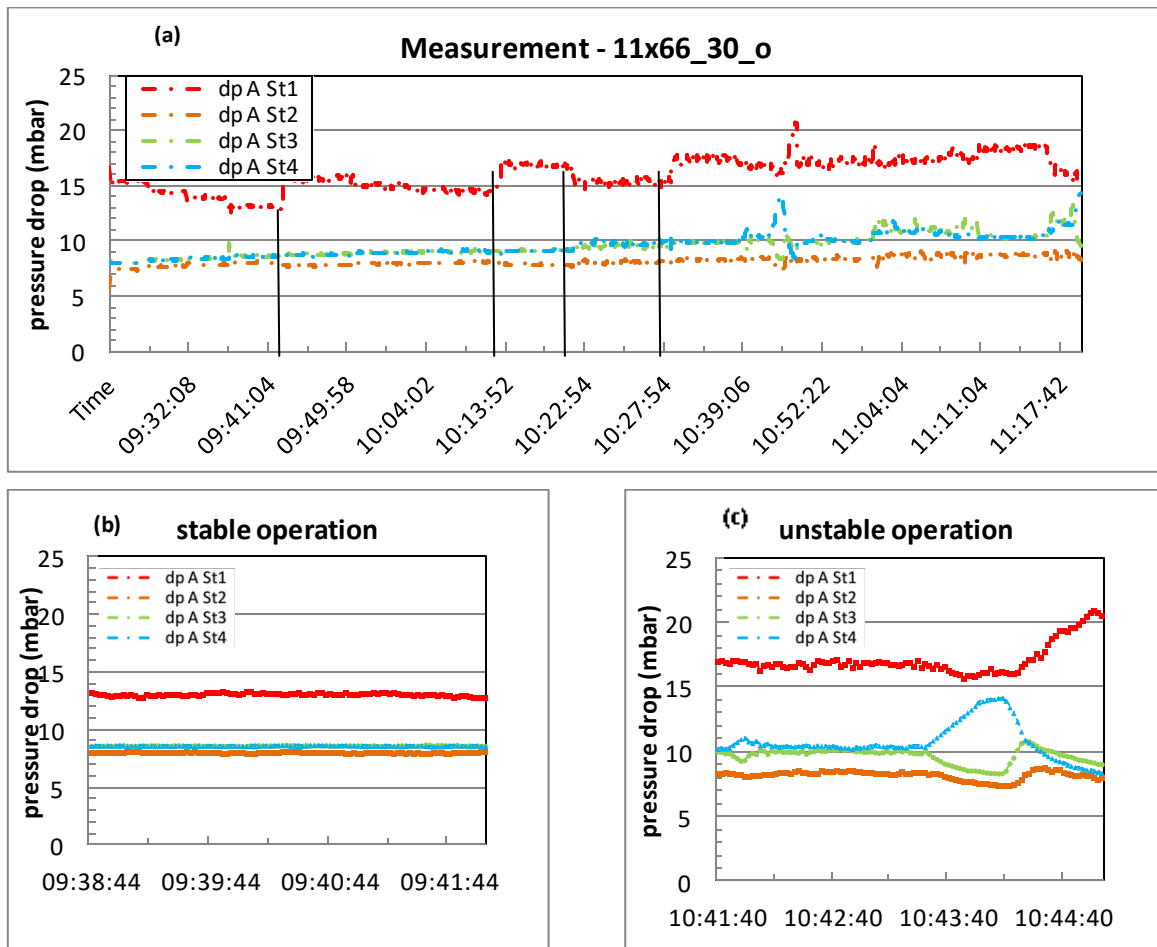


Figure 3.15. Definition of a stable operation point (a) actual course (b) stable (c) unstable operation

3.3.3. Shut down

After the experiment was carried out, and all data stored, the shutdown process could be performed. First, the screw conveyor was stopped as well as the fluidization of the column. The riser was further fluidized for a short time. The bed material started to trickle through the column to the lowest stage. From then on, the bed material was fed from the column into the storage hopper by means of the screw conveyor and the riser until the column was completely emptied. This step was necessary almost every time, as the column was modified often.

After the power supply and air supply were turned off, the modification of the column could be carried out.

4. Results

This chapter is divided into two subchapters, since two different methods of downcomers were tested and discusses the results of the experiments. Chapter 4.1 includes the results of the design variation of internal downcomers and further Chapter 4.2, includes the results of the external downcomers tests. As can be seen, a vast variety of operating conditions and modifications were tested. Hence, a greater understanding of the unit operation conditions was gained.

The focus was on determining the maximum solid flux through the internal downcomers. Since the flux is related to an area, the same area has always been used as a reference, namely, the downcomer cross section. The flux is determined using the measured solid circulation rate at stable operation conditions, by means of the equation:

$$flux = \frac{\dot{m}}{A_{Dc}} = \frac{\overline{SCR}}{A_{Dc}} = \frac{kg}{s * m^2} \quad (Eq. 4.1.)$$

One should consider that this formula was used in all calculations and is the general one for the flux in this work.

4.1. Internal downcomer

As already mentioned in Chapter 2 and in Figure 4.1 below, an internal downcomer requires a significant amount of the fluidized bed area. The tests of internal downcomers were carried out with the basic idea of minimizing the required downcomer area, still maintaining high solid circulation rates, since this result into a high solid flux. For this reason, the downcomer area has been constantly reduced by means of restriction plates and the geometry has also been adapted. Starting from an area ratio of 10% of the fluidized bed area, it was reduced to an area ratio of 0.625%. Furthermore, the immersion depths of the downcomers and thus the height of the solid inlet slot, as well as different distributor designs were investigated. In Table 4.1., an overview of the downcomer areas, as well as the downcomer to bed ratio, is given. Thereby the bed area was defined as the cross area of the column with $4.84 * 10^{-2} m^2$.

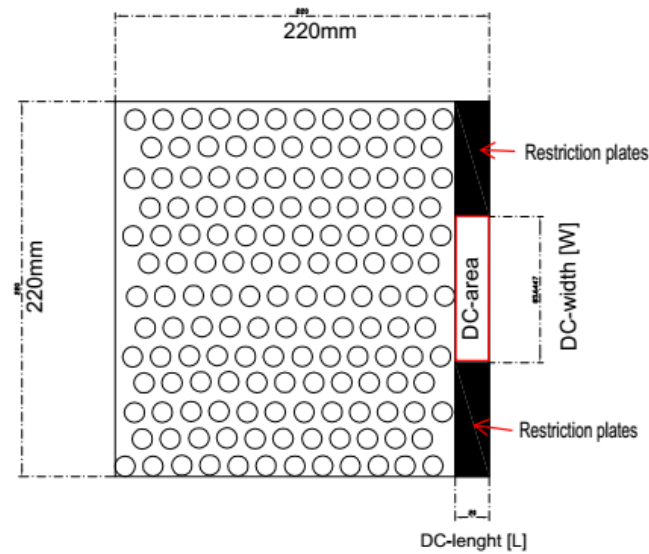


Figure 4.1. Top View of the stage

Table 4.1. Areas of internal downcomers

	Downcomer area (m^2)	Proportion to bed area (%)
22x220_30_o	$4.84 \cdot 10^{-3}$	10
16.5x220_30_o	$3.63 \cdot 10^{-3}$	7.5
11x220_30_o	$2.42 \cdot 10^{-3}$	5
11x66_30_o	$7.2 \cdot 10^{-4}$	1.5
11x66_15_o	$7.2 \cdot 10^{-4}$	1.5
11x55_30_o	$6.05 \cdot 10^{-4}$	1.25
11x55_30_p	$6.05 \cdot 10^{-4}$	1.25
11x55_30_c	$6.05 \cdot 10^{-4}$	1.25
11x27.5_30_c	$3.025 \cdot 10^{-4}$	0.625
22x27.5_30_o	$6.05 \cdot 10^{-4}$	1.25

The first experiments were carried out with internal downcomers and flaps. Starting with the downcomer 22x220_30_o, which has a DC to bed ratio of 10%, followed by 7.5% and 5%. The results of the first three experiments were always the same, namely that the bed material could flow through the downcomers at any solid circulation rate. Therefore, these rates are limited only by the maximum feed rate of the screw conveyor. The results of the first three measurements are listed in Table 4.2. Taking into account the investigated DC- areas from Table 4.1, the flux is determined using the measured solid circulation rate at stable operation conditions, according to equation (Eq.4.1.). As can be seen in Table 4.2, a stable operation with these downcomers is possible; however the maximum possible solid flux reaches 26 kg/m²s.

Table 4.2. Results of measurements :22x220_30_o/16.5x220_30_o/ 11x220_30_o

Operation point U/U _{mf}	Superficial velocity (m/s)	Solid circulation rate (kg/h)	Flux (kg/m ² s)
22x220_30_o			
6	0.1	230	13
8	0.14	230	13
10	0.17	230	13
12	0.21	230	13
14	0.24	230	13
16.5x220_30_o			
6	0.1	230	18
8	0.14	230	18
10	0.17	230	18
12	0.21	230	18
14	0.24	230	18
11x220_30_o			
6	0.1	230	26
8	0.14	230	26
10	0.17	230	26
12	0.21	230	26
14	0.24	230	26

- **11x66_30_o**

In the next step, the downcomer area was reduced. As can be seen in Figure 4.2., below a fluidization number of 12 at a stable operation point, the maximum possible solid circulation rate could be achieved. At a fluidization number of 12, the maximum possible solid flux decreased by 25%, compared to lower fluidization numbers, to a value of 171.5 kg/h. Higher SC-rates led to an unstable operation point due to overfilling of the downcomer. At a fluidization number of 14, which corresponds to a superficial velocity of 0.24 m/s, only a flux of 48.1 kg/m²s was possible. Further increases of the SC- rate lead to unstable operation conditions.

In Figure 4.2 the average recorded data is plotted, whereby the fluidization number is plotted on the abscissa and the Solid circulation rate on the ordinate of the diagram. In Table 4.3, the average recorded data and the results, which have been calculated according to equation Eq.4.1, can be seen.

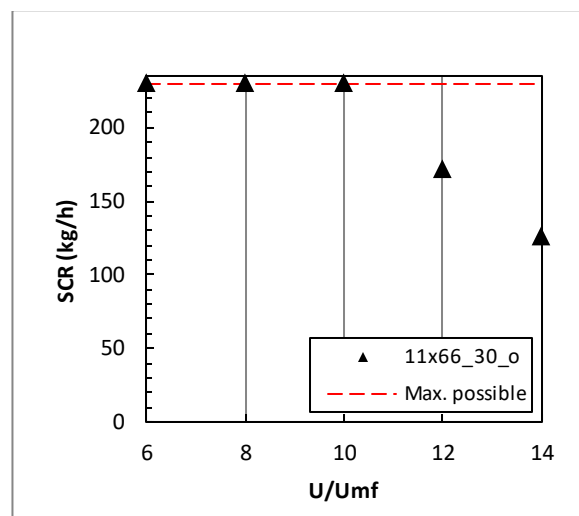


Figure 4.2. Measurement-11x66_30_o

Table 4.3. Measurement-11x66_30_o

Operation point U/Umf	Superficial velocity (m/s)	Solid circulation rate (kg/h)	Flux (kg/m ² s)
6	0.1	230	88
8	0.14	230	88
10	0.17	230	88
12	0.21	171.5	66
14	0.24	125.8	48.5

- **11x66_15_o**

Subsequently, the entrance height between the downcomer to lower stage was reduced. The entrance height was reduced from 30mm to 15mm. Since the adjusted outlet opening of the downcomer functioned as a higher flow resistance for the solid flow into the lower stage, the bed material within the downcomer started to accumulate, which results in a moving bed regime inside the downcomer.. First, the fluidization within the downcomer stopped, followed by a steady rise of the solid bed height, until it reached the actual downcomer height of 260mm. Further increase of the fluidization, from a fluidization number of 6 up to 8, favored the solid transport through the downcomer.

In theory, the solid heights in all downcomers should be at the same level. However, at an operation point, with a fluidization number of 8 and a SCR of 35kg/h, the solid bed height within the downcomer DC₄₋₃ was 14.5cm while the solid bed height within the DC₃₋₂ was 12.8cm. From a fluidization number of 8 onwards, the solid flux decreased, because of higher superficial velocities occasionally cause bubbles to occur within the downcomer. These bubbles support the material bridge formation, which can lead to slugging phenomena. As can be seen in *Figurer 4.3.*, the maximum possible solid flux was determined at a stable operation point at a fluidization number of 8 with a value of 39.7 kg/m²s, whereby at a fluidization number of 12 only a maximum possible flux of 30.8kg/m²s was obtained. Despite the fluidization increase, the solid flux decreased by 22%.

Further increase of the fluidization, up to a fluidization number of 14, led to a faster bubble formation, but had the positive effect that the more turbulent bubble movement prevented the material from bridging, therefore a slightly higher flux was possible as can be seen in Table 4.4.

In conclusion, the immersion depth of the downcomer has a great impact. The entrance depth of 15mm, from the downcomer to the lower stage, led to a decrease of the maximum solid circulation rate as well as the flux. For this reason, the experiments have been continued with a constant entrance height of 30mm.

In Figure 4.3 the average recorded data is plotted, whereby the fluidization number is plotted on the abscissa and the solid circulation rate on the ordinate of the diagram. In Table 4.4, the average recorded data and the results, which have been calculated according to equation Eq.4.1, can be seen.

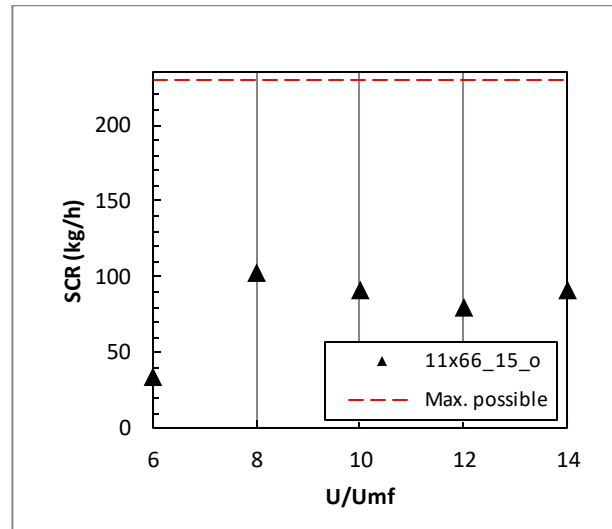


Figure 4.3. Measurement-11x66_15_o

Table 4.4. Measurement-11x66_15_o

Operation U/Umf	point	Superficial velocity (m/s)	Solid circulation rate (kg/h)	Flux (kg/m ² s)
6		0.1	34.3	13.1
8		0.14	103	39.7
10		0.17	91.5	35
12		0.21	80	30.8
14		0.24	91.5	35

- **11x55_30_o**

With decreasing width of the downcomer, while maintaining the fluidization of the downcomer, the slugging problem increases. This experiment provides only one stable operation point, namely, at a fluidization number of 6 the maximal solid circulation rate was determined, with approximately 95 kg/h. Any further increase of the fluidization led to an unstable operation point. Thereby, no further data could be gained, since no transport of solids was possible

Table 4.5. Measurement-11x55_30_o

Operation U/Umf	point	Superficial velocity (m/s)	Solid circulation rate (kg/h)	Flux (kg/m ² s)
6		0.1	95	44

Addition:

Since the bubble formation, and the resulting slugging phenomena, has become the ever-increasing problem, an estimate of the maximum bubble size was performed according to the formula of Darton et al.[11]:

$$D_{eq} = 0.54 * (U - U_{mf})^{0.4} * (h + \sqrt[4]{A_0})^{0.8} * g^{-0.2} \quad (Eq. 4.2.)$$

The results are shown in *Figure 4.4.*, resulting in a maximum bubble diameter, at a fluidization number of 14, of around 75mm at the downcomer height of 260mm. A typical slugging trend was documented with a camera, and is illustrated in *Figure 4.5.*, from left to right. As one can see, the bubbles start to formate at the gas distributor and rise upwards, while the bubble diameter increases through bubble coalescence [11]. The down flowing particles flow smoothly by the wall, to avoid the uprising bubble. Once the bubble diameter is greater than the downcomer width, the material flow downwards is impaired and this results in an overflow of the upper stage. Afterwards the bubble push the formed bed above away and immediately particles rain down into the downcomer. It should be noted that about this time another slug forms and the unstable motion is repeated. At higher gas velocities or rough walls, the rising slugs tend to adhere to the wall [37]. To counteract the slugging, mechanical vibrators could prevent the material from bridging at the wall as well as the reduction of aeration inside the downcomer. The first countermeasure taken was to close two of four orifices inside the downcomer, primarily to reduce the gas flow through the downcomer and thus the bubble formation.

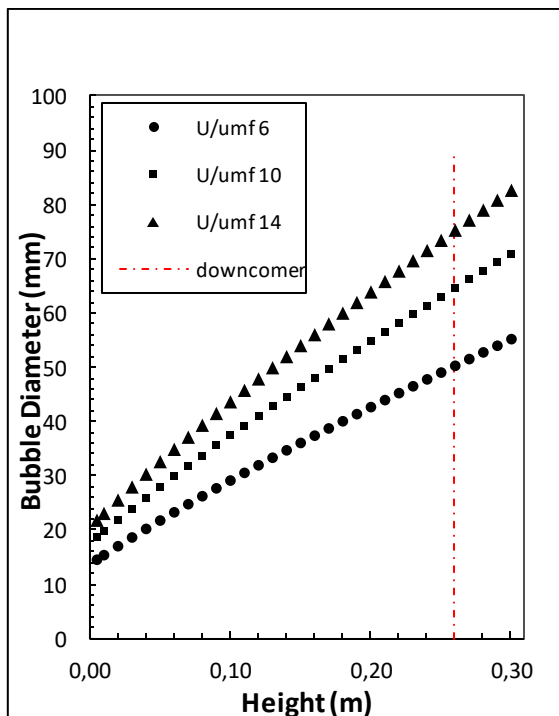


Figure 4.4. Bubble diameter according to Darton

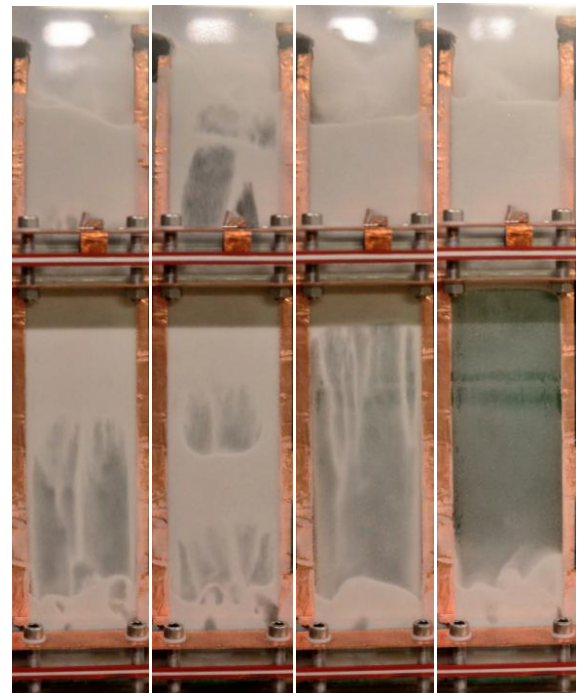


Figure 4.5. slugging trend from left to right

- **11x55_30_p**

As already mentioned, a typical countermeasure is the reduction of gas flow, thereby reduce the bubble formation. Therefore, two of four orifices below the downcomers were closed, with the aim of reducing fluidization in the downcomer. This countermeasure had the result that the maximum solid circulation at a fluidization number of 6 increased by over 60%. In addition, a solid circulation was possible for all other fluidization numbers. However, as can be seen in Figure 4.6., the solid flux decreases with further increase of the fluidization, since consequently also more bubbles form.

In Figure 4.6 the average recorded data is plotted, whereby the fluidization number is plotted on the abscissa and the solid circulation rate on the ordinate of the diagram. In Table 4.6, the average recorded data and the results, which have been calculated according to equation Eq.4.1, can be seen.

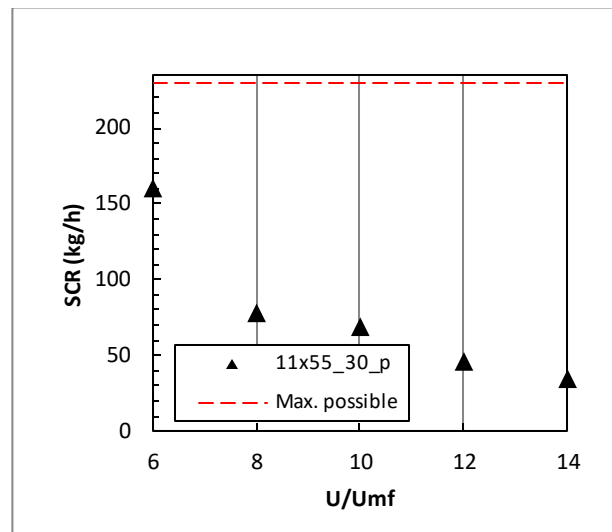


Figure 4.6. Measurement-11x55_30_p

Table 4.6. Measurement-11x55_30_p

Operation U/Umf	point	Superficial velocity (m/s)	Solid circulation rate (kg/h)	Flux (kg/m ² s)
6		0.1	160	73.5
8		0.14	78	35.8
10		0.17	69	31.7
12		0.21	45.8	21
14		0.24	34.3	15.8

- **11x55_30_c**

In order to show the influence of the aeration within a downcomer, four of four holes were completely closed. As mentioned in the experiment above, the countermeasure had provided notable improvement. At the start of this experiment only a SCR of 109 kg/h was possible, while at a partially fluidization, experiment 11x55_30_p, the SCR was determined with a value of 160 kg/h at a column fluidization number of 6. However, at higher fluidization numbers of 8 to 14, the reduced aeration within the downcomer shows a significant enhancement. By using this countermeasure,

it was possible to reach the maximal possible SCR at a fluidization number of 10, whereas with a partially fluidization only a rate of 69 kg/h were possible. It is worth to note that starting from a fluidization number of 10, a moving bed regime is noticeably within the downcomers, even if according to the regime map of Grace, the regime is in bubbling fluidization at a superficial gas velocity of 0.17m/s. (Chapter 2.1.7)

In Figure 4.7 the average recorded data is plotted, whereby the fluidization number is plotted on the abscissa and the Solid circulation rate on the ordinate of the diagram. In Table 4.7, the average recorded data and the results, which have been calculated according to equation Eq.4.1, can be seen.

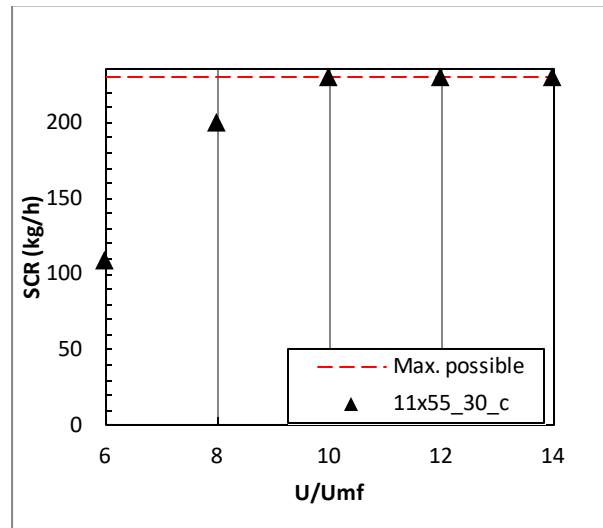


Figure 4.7. Measurement-11x55_30_c

Table 4.7. Measurement-11x55_30_c

Operation point	U/Umf	Superficial velocity (m/s)	Solid circulation rate (kg/h)	Flux (kg/m ² s)
6	0.1	0.1	109	50
8	0.14	0.14	200	92
10	0.17	0.17	230	105
12	0.21	0.21	230	105
14	0.24	0.24	230	105

- **11x27.5_30_c**

Since a stable operation was possible due to the constructive countermeasures, in the next step the area was further reduced to a DC to bed ratio of 0.625 %. Due to the decreasing area, the wall friction effects increase. A moving bed regime was recognized in all operation points, but nevertheless allowed a stable solid circulation within the MStFB-system. At a fluidization number of 6, a stable operation was possible with a SCR at a low value of 20.7 kg/h. By increasing the fluidization of the column, also the flux increased to 75.6 kg/m²s at a fluidization number of 14. Thus, it was shown that a low downcomer area can also ensure a stable operation. However, the question arises whether this low flux is practically useful.

In Figure 4.8 the average recorded data is plotted, whereby the fluidization number is plotted on the abscissa and the Solid circulation rate on the ordinate of the diagram. In Table 4.8, the average recorded data and the results, which have been calculated according to equation Eq.4.1, can be seen.

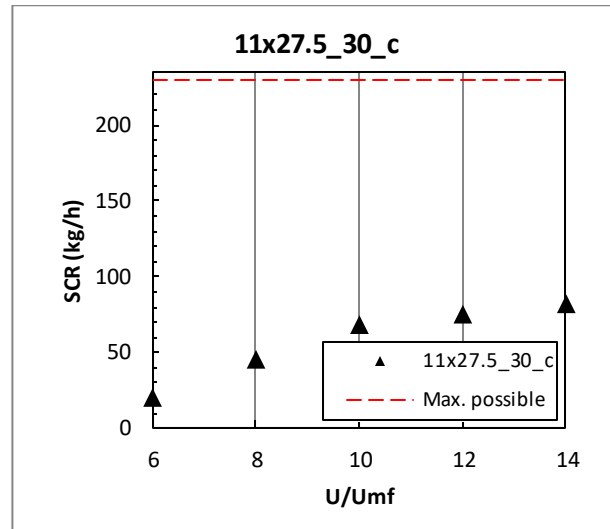


Figure 4.8. Measurement-11x27.5_30_c

Table 4.8. Measurement-11x27.5_30_c

Operation U/Umf	point	Superficial velocity (m/s)	Solid circulation rate (kg/h)	Flux (kg/m ² s)
6		0.1	20.7	19
8		0.14	45.8	42
10		0.17	69	63.3
12		0.21	75.5	69.3
14		0.24	82.3	75.6

- **22x27.5_30_o**

After it has been shown that stable operation is also possible for small areas, and the main influencing factor for internal downcomers is apparently the fluidization inside the downcomers, the area was increased again to 1.25% but the geometry was changed, with the basic idea to prevent slugging regime by increasing the width of the DC to a value exceeding the expected max. bubble diameter.

To make comparison to the downcomer 11x55_30_o, which has the same area, the holes in the downcomer were opened again, to ensure a fluidization within the downcomer. As mentioned, the experiments 11x55_30_o led to no stable operation point, except at a fluidization number of 6. The wall surface in the downcomer was reduced by approximately 25%, while remaining the same downcomer area.

	Area (m^2)	Proportion to the total area (%)	Wall surface in the DC (m^2)
11x55_30_o	$6.05 * 10^{-4}$	1.25	0.03432
22x27.5_30_o	$6.05 * 10^{-4}$	1.25	0.02574

As can be seen, it was possible to carry out all operation points, even if a moving bed regime was observed. Conclusively, this experiment shows that the geometry of the downcomer has a considerable influence on the maximum solid flux due to the fact that the wall friction effects were reduced by reducing the total wall surface in a downcomer.

In Figure 4.9 the average recorded data is plotted, whereby the fluidization number is plotted on the abscissa and the solid circulation rate on the ordinate of the diagram. In Table 4.9, the average recorded data and the results, which have been calculated according to equation Eq.4.1, can be seen.

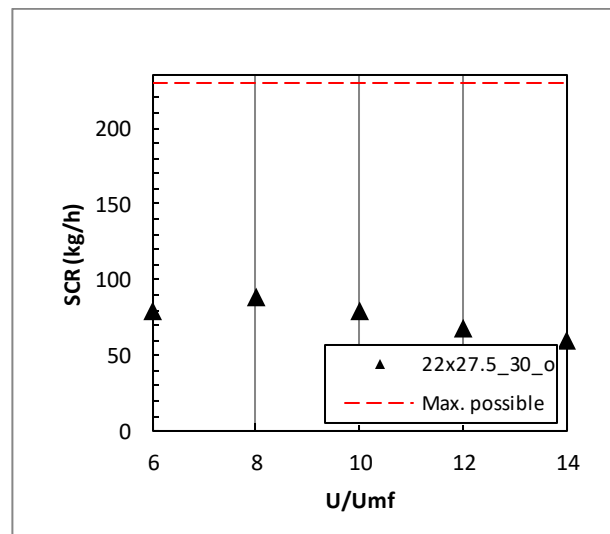


Figure 4.9. Measurement-22x27.5_30_o

Table 4.9. Measurement-22x27.5_30_o

Operation U/Umf	point	Superficial velocity (m/s)	velocity	Solid circulation rate (kg/h)	Flux (kg/m^2s)
6		0.1		80	36.7
8		0.14		89.2	40.96
10		0.17		80	36.7
12		0.21		68.6	31.4
14		0.24		60.61	27.83

4.2. External downcomer

Due to the constructive advantage of the external downcomers, the maximum solid circulation rate could be achieved at all operation points. The cross section of external downcomers is $4.9 \cdot 10^{-4} \text{ m}^2$. The diameter of the pipes, used as external downcomers, is 25mm. This results in a solid flux of $130.15 \text{ kg/m}^2\text{s}$ for all tests with external downcomers. It was then examined which conveyance principle is more suitable in the downcomers with regard to the minimum aeration required. The two applied principles were, on the one hand, an L-valve and, on the other hand, a lance, which was perforated with holes in order to completely fluidize the horizontal part of the downcomers. In *Figure 4.10.*, the average recorded data is plotted. In *Table 4.10.*, the average recorded results can be seen. Upon closer examination one can see that both have almost identical values, however, the lance required on average less fluidization agent than the L-Valve. The L-Valve reached the operating limit at a fluidization number of 14 and at maximum solid circulation, while the lance conveys the bed material without problems. As can be seen in *Table 4.10.*, at a fluidization number of 14 and the maximum possible SCR, it was impossible to determine the minimum aeration of the L-Valve. The high fluidization led to slugging phenomena and an extreme ballistic movement of solids. These phenomena were observed in the downcomers, but a stable operation point at any SC-rate was possible.

Table 4.10. Measurement-Minimal aeration at operating point -external downcomers

Operation point								
U/U _{mf}	Fluidization Column (Nm ³ /h)	75 kg/h	150 kg/h	230 kg/h	75 kg/h	150 kg/h	230 kg/h	
		Min. aeration L-valve (NI/h)			Min. aeration lance (NI/h)			
6	18	65	75	85	60	70	85	
8	24	65	75	85	60	70	80	
10	30	60	75	85	60	75	80	
12	36	70	85	95	75	85	95	
14	42	80	95	-	85	95	105	

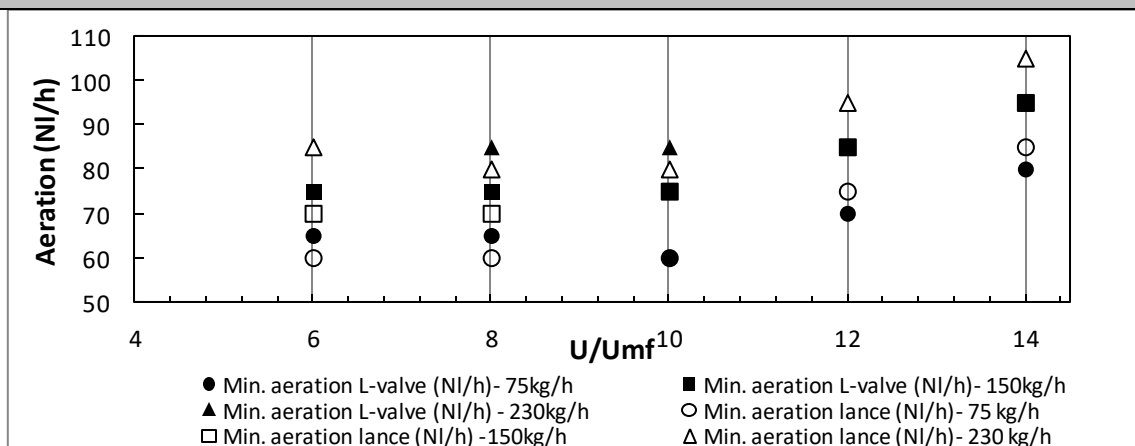


Figure 4.10. Measurement-minimal aeration at operating point- external downcomers

5. Summary & conclusion

The MstFB-CFM study performed with internal and external downcomers, proved the fluid dynamic feasibility of the adsorber column of the planned TSA-pilot scale unit. The results have led to many statements about the optimization of downcomers. The chosen designs show a stable and robust operability also for the planed PSU. The full operational capability is ensured. Since two different designs were studied, namely, internal and external downcomers, these are also discussed separately below.

Internal downcomers

Table 5.1, shows the summarized results of the experiments at the corresponding fluidization numbers. The colored fields are the flux values at the maximum possible solid circulation rate. Therefore, these values are limited only by the conveyed volume of the screw conveyor. Furthermore the fields with a moving bed regime in the downcomer have been marked with a (*)

Table 5.1. Summary of Results of the study of internal downcomers

		Fluidization number				
		6	8	10	12	14
		superficial velocity (m/s)				
		0.1	0.14	0.17	0.21	0.24
22x220_30_o	Solid flux (kg/m ² s)	13	13	13	13	13
16.5x220_30_o		18	18	18	18	18
11x220_30_o		26	26	26	26	26
11x66_30_o		88	88	88	66	48.5
11x66_15_o		13*	40*	35*	31*	35*
11x55_30_o		44	0	0	0	0
11x55_30_p		74	36	32	21	16
11x55_30_c		50*	92*	105	105	105
11x27.5_30_c		19*	42*	63*	69*	76*
22x27.5_30_o		37*	41*	37*	32*	28*

(*) moving bed regime at maximum flux

Max. SCR

External downcomers

A solid flux of 130.15kg/m²s was determined for external downcomers at any stable operating point. The cross section of external downcomers is 4.9 *10⁻⁴ m² (diameter: 25mm). The DC cross section to fluidized bed ratio is 1%. Nevertheless, the maximum solid circulation rate could be achieved at all operation points. The examination of which conveyance principle is more suitable

in the downcomers with regard to the minimum aeration required, the lance has a slightly lower aeration demand than the L-Valve. The L-Valve reached the range of application at a fluidization number of 14 and at maximum solid circulation, while the lance conveys the bed material without problems.

Conclusion

The first tests, with internal downcomers, already showed that by increasing the entrance height of the downcomer to the lower stage, the solid flux at same condition increased too. In conclusion, the immersion depth of the downcomer should enable a formation of a fluidized bed in the lower stage, but nevertheless, enable a practical useful solid flux through the downcomer. Comparing experiments 11x66_30_o and 11x66_15_o with each other, one can see that the depth of immersion of the downcomer was the only parameter which varied. However, the obtained results differed greatly from each other. The first test, with an entrance height of 30mm, established a steady stable operation, and even for the first fluidization numbers of 6 and 8 a maximum solid flux of 88 kg/m²s was reached. On other hand an entrance height of 15mm supplies only a maximum solid flux of 35 kg/m²s in a moving bed regime at a fluidization number of 8 up to 14.

The second interesting conclusion can be seen by comparing the experiments 11x55_30_o, 11x55_30_p and 11x55_30_c. Even though the design of the distributor plates within the downcomers was the only parameter which were varied, significant differences in results can be found between those three experiments. These result in the assumption that at decreasing gas flow rates within the downcomer, the maximum solid flux increase.

The third conclusion can be seen by comparing the experiments 11x55_30_o and 22x27.5_30_o. Even though both downcomers exhibit the same cross area, experiments with 22x27.5_30_o result in higher maximum possible solid flux compared to experiment with the downcomer 11x55_30_o. More specifically, this experiment provides only one stable operation point, namely, at a fluidization number of 6 the maximal solid circulation rate was determined, with approximately 95 kg/h. Any further increase of the fluidization led to an unstable operation point.

Comparing between the two different downcomer designs, it is clear to see that the choice of the used downcomer design leading to both, advantages and disadvantages. Using internal downcomers in reactors goes hand in hand with the resulting loss of fluidized bed area. While the difficult construction and required downcomer aeration of external downcomers should be mentioned as a disadvantage, the additional fluidized bed area should be considered too.

Furthermore, the start up of the CFM with external downcomers turned out easier than with internal downcomers, since bed material remain inside after shut down. The filled downcomer have a higher pressure drop and seal the downcomer while start up, whereas internal downcomers require an active control of the empty downcomer pressure drop by means of flaps or continuous observation. Without an active control, the fluidization agent was preferably flowing through the empty downcomers. This phenomenon finally led to defluidization of the stages.

One of the important aspects that should be considered, is the heat loss in external downcomers while desorption in the TSA- process. Therefore, reactors with internal downcomers seem more reasonable despite the worse performance compared to external downcomers, since external downcomers require a better insulation.

Which downcomer design is finally used in the PSU depends on many factors: costs, space requirements, handling and implementation. With external downcomers, the regulation solids hold-up in each stage is possible. Furthermore, flue gas can be used as the aeration agent in external downcomers. Therefore, external downcomers can be used in the adsorber column of the PSU. In the case of the desorber column, external downcomers need steam as the aeration agent. Due to the extensive insulation, internal downcomers seem to be the better choice.

The maximum possible solid flux within the process changes in the following way relative to the mentioned operating parameters:

- Reducing the fluidization within the downcomer result in an increase of the maximum possible solid flux.
- A higher entrance height between DC and lower stage, results in a higher maximum possible solid flux.
- Through reduction of the wall friction effects, by adapting the length and width of the downcomer, a higher maximum possible solid flux is reached.

List of Figures

Fig 1.1.	Map of the observed surface temperature change from 1901 to 2012 derived from temperature trends determined by linear regression from one dataset.	[33]
Fig 1.2.	Atmospheric concentrations of carbon dioxide (CO ₂) from Mauna Loa (19°32'N, 155°34'W – red) and South Pole (89°59'S, 24°48'W – black) since 1958	[33]
Fig 1.3.	Average monthly Arctic sea Ice Extent from 1978-2016	[66]
Fig 1.4.	CO ₂ Capture Systems - flowsheet	[31]
Fig 1.5.	Example for temperature swing adsorption	[57]
Fig 1.6.	Basic scheme of a double loop staged fluidized bed system for continuous TSA	[67]
Fig 2.1.	(a) The Winkler gas Generator and the (b) first large scale pilot plant for fluid catalytic cracking	[37]
Fig 2.2.	Pressure drop induced by a gas flowing through a bed	[63]
Fig 2.3.	Schematic representation showing the appearance of flow regime relevant to gas solid fluidization	[37]
Fig 2.4.	Solid distribution in bubbling fluidized bed reactors	[63]
Fig 2.5.	Geldart classification of particles for air at ambient conditions	[19]
Fig 2.6.	Pressure drop induced by a gas flowing through a bed, adopted from	[24]
Fig 2.7.	Pressure drop across a bed of solid particle as a function of gas velocity	[37]
Fig 2.8.	The equilibrium of forces	
Fig 2.9.	Development of the drag coefficient for a sphere with the Reynolds number	[35]
Fig 2.10.	Fluidization regime map according to Reh	[21]
Fig 2.11.	Fluidization regime map according to Grace	[5]
Fig 2.12.	Heat transfer coefficient dependency on fluidization number	[37]
Fig 2.13.	Flows in a single-stage fluidized bed with a single-size feed.	[37]

Fig 2.14.	Multistage fluidized bed operations, counter- and crossflow operations.	[37]
Fig 2.15.	Exit age distribution (RTD) for solids in ideal multistaged fluidized beds,	[37]
Fig 2.16.	Variations of fluidized bed reactor configurations. (a) multi-stage bed, (b) multi-stage with countercurrent solid flow (c) multi-stage with external solid circulation (d) multi-cell bubbling bed	[65]
Fig 2.17.	perforated plate	[51]
Fig 2.18.	bubble caps	[51]
Fig 2.19.	sparger	[51]
Fig 2.20.	conical grids	[51]
Fig 2.21.	Grid hole discharge coefficient design chart	[51]
Fig 2.22.	The relationship between hole density and grid hole pitch for triangular and square pitch	[51]
Fig 2.23.	Downcomer designs configuration of the top and ends of downcomers	[51]
Fig 3.1.	Scale up procedure to establish an industrial full-scale catalytic fluidized bed reactor.	[60]
Fig 3.2.	Basic scheme of the cold flow model	
Fig 3.3.	Relationship between humidity and static charge	[29]
Fig 3.4.	Basic scheme of the lance and L-Valve	[60]
Fig 3.5.	Picture of the cold flow model	
Fig 3.6.	P&ID scheme of the CFM with (a) internal downcomers and (b) external downcomers	
Fig 3.7.	Measurement equipment- Determination of the minimum fluidized velocity	
Fig 3.8.	Umf glas beads 100-200 μ m as recieved	
Fig 3.9.	Umf glas beads 100-200 μ m used	
Fig 3.10.	SCR at Riserfluidization 6.1 Nm ³ /h	

- Fig 3.11.** SCR at Riserfluidization 7.1 Nm³/h
- Fig 3.12.** Side view-Downcomer with flaps
- Fig 3.13.** Side view of a stage- entrance height
- Fig 3.14.** Top View of a stage-fluidization conditions
- Fig 3.15.** Definition of a stable operation point (a) actual course (b) stable (c) unstable operation
- Fig 4.1.** Top View of a stage
- Fig 4.2.** Measurement-11x66_30_o
- Fig 4.3.** Measurement-11x66_15_o
- Fig 4.4.** Bubble diameter according to Darton
- Fig 4.5.** slugging trend from left to right
- Fig 4.6.** Measurement-11x55_30_p
- Fig 4.7.** Measurement-11x55_30_c
- Fig 4.8.** Measurement-11x27.5_30_c
- Fig 4.9.** Measurement-22x27.5_30_o
- Fig 4.10.** Measurement-Minimal Aeration at Operating Point External downcomers

List of Tables

Tab 1.1 .	Table of construction design parameter of the BSU adopted from	[48] and [13]
Tab 2.1.	Table of several diameters for particle size definition	[52]
Tab 2.2.	Table of sphericity of technical relevant materials	[52]
Tab 2.3.	Table of drag coefficient in 3 areas	[24]
Tab 3.1.	simplified set of Scaling laws by Glicksman- Dimensionless numbers with equation	[20]
Tab 3.2.	Measuring Units of the cold flow model	
Tab 3.3.	Results and calculation- Umf glass beads 100-200 μm as received	
Tab 3.4.	Results and calculation- Umf glass beads 100-200 μm used	
Tab 3.5.	Fluidization numbers and required volume flow	
Tab 3.6.	SCR at Riserfluidization 6.1 Nm^3/h and 7.1 Nm^3/h	
Tab 3.7.	Scheme of the nomenclature	
Tab 4.1.	Areas of internal downcomers	
Tab 4.2.	Results of measurements :22x220_30_o/16.5x220_30_o/ 11x220_30_o	
Tab 4.3.	Measurement-11x66_30_o	
Tab 4.4.	Measurement-11x66_15_o	
Tab 4.5.	Measurement-11x55_30_o	
Tab 4.6.	Measurement-11x55_30_p	
Tab 4.7.	Measurement-11x55_30_c	
Tab 4.8.	Measurement-11x27.5_30_c	

Tab 4.9. Measurement-22x27.5_30_o

Tab 4.10. Measurement-Minimal Aeration at Operating Point External downcomers

Tab 5.1. Summary of Results of the study of internal downcomers

Notation

List of Abbreviations

Abbreviations	Meaning
<i>BSU</i>	<i>bench scale unit</i>
<i>PSU</i>	<i>pilot scale unit</i>
<i>TSA</i>	<i>temperature swing adsorption</i>
<i>CFM</i>	<i>cold flow model</i>
<i>MStFB</i>	<i>multistage- fluidized bed</i>
<i>SCR</i>	<i>solid circulation rate</i>

List of Symbols

Symbol	Unit	Meaning
<i>A</i>	m^2	<i>Area</i>
<i>a</i>	m/s^2	<i>acceleration</i>
<i>A₀ or (A/N)</i>	m^2	<i>distributor cross area / number of orifice</i>
<i>Ar</i>	-	<i>Archimedes number</i>
<i>b'</i>	-	<i>dimensionless factor according to Eq. X</i>
<i>c</i>	$Mole/m^3$	<i>Concentration</i>
<i>Cd</i>	-	<i>drag coefficient</i>
<i>d</i>	m	<i>Diameter</i>
<i>DC</i>	-	<i>Downcomer</i>
<i>d_p*</i>	-	<i>dimensionless particle diameter</i>
<i>f</i>	Hz	<i>Frequency</i>
<i>F</i>	N	<i>Force</i>
<i>F_F</i>	N/m^3	<i>Friction force</i>
<i>Fr</i>	-	<i>Froude number</i>
<i>Fr</i>	-	<i>Froude number</i>
<i>g</i>	$9,81 m/s^2$	<i>Gravitational acceleration</i>
<i>G</i>	N/m^3	<i>Gravitational force</i>
<i>H</i>	m	<i>height</i>
<i>L</i>	m	<i>Characteristic Length</i>
<i>L_H</i>	m	<i>grid hole pitch</i>
<i>M</i>	kg	<i>Mass</i>
<i>\dot{m}</i>	kg/h	<i>mass flow</i>
<i>N</i>	-	<i>Number</i>
<i>N_d</i>	$1/m^2$	<i>number hole density</i>
<i>p</i>	$mbar$	<i>Pressure</i>
<i>q</i>	mol/g	<i>Specific loading</i>
<i>Re</i>	-	<i>Reynolds number</i>
<i>SCR</i>	kg/h	<i>Solid circulation rate</i>
<i>T</i>	K	<i>Temperature</i>
<i>t</i>	s	<i>time</i>
<i>U</i>	m/s	<i>Velocity</i>
<i>u*</i>	-	<i>dimensionless superficial gas velocity</i>

U/U_{mf}	-	Dimensionless fluidization number
u_t	m/s	freefall or terminal velocity
V	m^3	volume
\dot{V}	Nm^3/h	flow rate at standard temperature and pressure [293,15K ; 1 atm]
W	kg	Weight
Δp	mbar	Pressure drop

List of Greek symbols

Greek symbol	Unit	Meaning
μ	Pa *s	dynamic viscosity
α	W/m^2K	heat transfer coefficient
ε	0-1	porosity/ voidage
ζ	-	resistance factor
π	3,14159...	Pi
ρ	kg/m^3	density
τ	s	residence time /contact time
φ	0-1	Sphericity
Ω	-	Litaschenko number
δb		bubble fraction

List of Indices

symbol	Meaning
# - #	refers to stage number to stage number
b	refers to bulk
bed	refers to bed
c	calculated
dc	refers to downcomer
$distr$	refers to distributor
f	refers to fluid
FB	refers to fluidized bed
Fix	refers to fixed bed
g	refers to gas
max	maximum possible
mf	at minimum fluidization conditions
or	refers to orifice
p	refers to particle
s	refers to solid
$St\#$	refers to Stage number (top=4; bottom=1)
t	refers to terminal conditions
W	refers to weir
eq	refers to sphere with equivalent size/diameter

References/ Bibliography

- [1] ACS ; (2016). American Chemical Society - National Historic Chemical Landmarks: *The Fluid Bed Reactor*,
<https://www.acs.org/content/acs/en/education/whatischemistry/landmarks/fluidbedreactor.html>
(25.08.2016)
- [2] Agarwal, J. C., Davis, W. L., King, D. T., (1962). " *Fluidized-bed coal dryer*". Chem. Eng. Prog. 58, 85-90.
- [3] APCC, (2014). *Summary for Policymakers (SPM)*. In: Österreichischer Sachstandsbericht Klimawandel (AAR14), Asutrian Panel on Climate Change (APCC), Verlag der Österreichischen Akademien der Wissenschaften, Vienna, Austria.
- [4] Beránek, J.; Rose, K.; Winterstein, G.; (1975). *Grundlagen der Wirbelschicht-Technik*. Leipzig: Krausskopf.
- [5] Bi, H. T.; Grace, J. R.; (1995). *Flow regime diagrams for gas-solid fluidization and upward transport*. Int. J. Multiphase Flow 21 (6), pp. 1229-1236
- [6] Bottoms, R. R., (1930). *Process for separating acidic gases*. Girdler Corp., U.S. patent 1783901.
- [7] IPCC, (2014). *Climate Change 2014: Impacts, Adaptation, and Vulnerability*;
<http://www.ipcc.ch/report/ar5/wg2/>
- [8] Briggs, Helen (December 1, 2007). "50 years on: *The Keeling Curve legacy*". BBC News.
- [9] Cheng-Hsiu Yu, Chih-Hung Huang, Chung-Sung Tan (2012); "A Review of CO₂ Capture by Absorption and Adsorption"; *Aerosol and Air Quality Research*, 12: 745–769, 2012
- [10] Bailey, D. W., Feron, P. H. M., (2005). *Post-Combustion Decarbonisation Processes*. Oil Gas Sci. Technol. 60 (3), 461-474.
- [11] Darton, R.C; LaNauze, R.D.; Davidson, J.F.; Harrison, D.; (1977). *Bubble Growth Due To Coalescence in Fluidized Beds*. Trans IChemE, Vol 55, 1977, pp. 274-280
- [12] Notz, D., Stroeve, J. ; *Observed Arctic sea-ice loss directly follows anthropogenic CO₂ emission*, Science, 03 Nov 2016: DOI: 10.1126/science.aag2345
- [13] Dietrich F. "A novel system for continuous temperature swing adsorption: parameter study at bench scale" Master Thesis, TU Vienna. 2014

- [14] Carlos A. Grande; (2012). "Advances in Pressure Swing Adsorption for Gas Separation" International Scholarly Research Network, ISRN Chemical Engineering Volume 2012, Article ID 982934, 13 pages doi:10.5402/2012/982934
- [15] Eleftheriades, C. M.; Judd, M. R.; (1978). *The design of downcomers joining gas-fluidized beds in multistage systems*. Powder Technology 21 (2), pp. 217-225
- [16] Ergun, S.; (1952). *Fluid flow through packed columns*. Chemical Engineering Progress 48, pp. 89-94
- [17] Fan, L. S., Zhu, C., "Principles of Gas-Solid Flows", Cambridge University Press, Cambridge, United Kingdom, First Edition, 1998
- [18] GCCSI (2012). Global Carbon Capture and Storage Institute: *CO₂ Capture Technologies - Post Combustion Capture (PCC)*
- [19] Geldart, D.; (1973). *Types of Gas Fluidization*. Powder Technology 7, pp. 494-502.
- [20] GLICKSMAN, L. R., "SCALING RELATIONSHIPS FOR FLUIDIZED BEDS", Chemical Engineering Science Vol. 39, No.9, 1984, pp. 1373-1379
- [21] Schmid, J. C., Pröll, T., Pfeifer, C., Rauch, R., Hofbauer, H., "COLD FLOW MODEL INVESTIGATION ON A MODIFIED RISER WITH ENHANCED GAS-SOLID CONTACT LOCATING THE REGIONS OF OPERATION IN A FLUIDIZATION REGIME MAP", Proc. 21st International Conference on Fluidized Bed Combustion (FBC), Naples, Italy, 2012, pp. 80-87
- [22] Grace, J. R., (1986). *Contacting Modes and Behaviour Classification of Gas-Solid and Other Two-Phase Suspensions*. Can. J. Chem. Eng. 64, 353-363.
- [23] Guío-Pérez, D. C., (2013). *Cold flow model assisted evaluation of an improved dual circulating fluidized bed design for chemical looping processes including solids residence time measurements*. PhD Thesis, Institute of Chemical Engineering, Vienna University of Technology, Vienna, Austria
- [24] Hofbauer, H.; (2016). "Unterlagen zur Vorlesung 159.220 Wirbelschichttechnik SS2016" ; TU Wien; 6. Auflage
- [25] Grace, J. R., "Circulating Fluidized Beds", BLACKIE ACADEMIC and PROFESSIONAL, London, United Kingdom, First Edition, 1997
- [26] Hsiung, T. H., Thodos, G., (1977). *Expansion characteristics of gas-fluidized beds*. Canadian Journal of Chemical Engineering 55 (2), 221-224.
- [27] http://unfccc.int/meetings/paris_nov_2015/meeting/8926.php

- [28] <http://www.ccsassociation.org/what-is-ccs/capture/> 10.11.2016
- [29] <http://www.keyence.com/products/static/electrostatic/sk/features/feature-02.jsp> 04.12.2016
- [30] IPCC (1990); "*Climate Change: The IPCC Scientific Assessment*" Report Prepared for IPCC by Working Group 1
- [31] IPCC, (2005). IPCC Special Report on Carbon Dioxide Capture and Storage. Prepared by Working Group III of the Intergovernmental Panel on Climate Change. Cambridge University Press, Cambridge, United Kingdom and New York, NY, USA.
- [32] IPCC, (2014). Climate Change 2014: Synthesis Report of the Fifth Assessment Report of the Intergovernmental Panel on Climate Change.
http://www.ipcc.ch/publications_and_data/publications_and_data_reports.shtml
- [33] IPCC, 2013: *Summary for Policymakers. In: Climate Change 2013: The Physical Science Basis. Contribution of Working Group I to the Fifth Assessment Report of the Intergovernmental Panel on Climate Change*, Stocker, T.F., D. Qin, G.-K. Plattner, M. Tignor, S.K. Allen, J. Boschung, A. Nauels, Y. Xia, V. Bex and P.M. Midgley. Cambridge University Press, Cambridge, United Kingdom and New York, NY, USA
- [34] Serna-Guerrero, R. and Sayari, A. (2010). Modeling Adsorption of CO₂ on Amine Functionalized Mesoporous Silica. 2: Kinetics and Breakthrough Curves. Chem. Eng. J. 161: 182–190
- [35] Munson, B. R., Young, D. F., and Okiishi, T. H., Fundamentals of Fluid Mechanics, Wiley, NY, 1990.
- [36] Krishnaiah, K.; Varma, Y. G.; (1982). *Pressure Drop, Solids Concentration and Mean Holding Time in Multistage Fluidisation*. The Canadian Journal of Chemical Engineering 60, pp. 346-352.
- [37] Kunii, D., Levenspiel, O., (1991). *Fluidization Engineering*. Butterworth-Heinemann, USA, 2nd Ed., 491.
- [38] Kuo, H.P; Cheng, C.Y.; (2006). *Investigation of the bed types and particle residence time in a staged fluidised bed*. Powder Technology 169 , pp. 1–9
- [39] M. Traoré, O. Dufaud, L. Perrin, S. Chazelet, D. Thomas "*Dust explosions: How should the influence of humidity be taken into account?*" CNRS - Laboratoire des Sciences du Génie Chimique, UHP-INPL – ENSIC, 1 rue Grandville, BP 20451, 54001 Nancy, France
- [40] Martín-Gullón, I.; Marcilla, A.; Font, R.; Asensio, M.; (1995). *Stable operating velocity range for multi-stage fluidized bed reactors with downcomers*. Powder Technology 85, pp. 193-201

- [41] Matthew E. Boot-Handford et al (2013), "*Carbon capture and storage update*". Energy & Environmental Science. Cite this: DOI: 10.1039/c3ee42350f
- [42] Michael Stollhof, "*Detailed fluid dynamic investigations of the fuel reactor of a novel DUAL FLUID reactor concept for Chemical Looping Combustion for solid fuels*" Master Thesis, TU Vienna 2014
- [43] Mohanty, C. R.; Meikap, B. C.; (2009). *Pressure drop characteristics of a multi-stage counter-current fluidized bed reactor for control of gaseous pollutants*. Chemical Engineering and Processing 48, pp. 209-216
- [44] Mohanty, C. R.; Meikap, B. C.; (2011). *Modeling the operation of a three-stage fluidized bed reactor for removing CO₂ from flue gases*. Journal of Hazardous Materials 187, pp.113–121
- [45] Mohanty, C.R.; Rajmohan, B.; Meikap, B.C.; (2010). *Identification of stable operating ranges of a counter-current multistage fluidized bed reactor with downcomer*. Chemical Engineering and Processing 49, pp. 104-112.
- [46] Molerus, O.; (1982). *Interpretation of Geldart's type A, B, C and D powders by taking into account interparticle cohesion forces*. Powder Technology 33 (1), pp. 81-87
- [47] Plaza, M.G., Pevida, C., Arenillas, A., Rubiera, F. and Pis, J.J. (2007). *CO₂ Capture by Adsorption with Nitrogen Enriched Carbons*. Fuel 86: 2204–2212.
- [48] Pröll, T.; Schöny, G.; Sprachmann, G.; Hofbauer, H. ; (2016). "*Introduction and evaluation of a double loop staged fluidized bed system for post-combustion CO₂ capture using solid sorbents in a continuous temperature swing adsorption process*". Chemical Engineering Science 141, pp. 166-174.
- [49] Rochelle, G. T., (2009). "*Amine Scrubbing for CO₂ capture*". Science 235, 1652-1654.
- [50] Royal Society,(2014) "*Climate Change Evidence & Causes*" An overview from the Royal Society and the US National Academy of Sciences
- [51] S.B. Reddy Karri and Ted M. Knowlton, "*Gas Distributor and Plenum Design in Fluidized Beds*"
- [52] Scala, Fabrizio ;(2013). *Fluidized bed technologies for near-zero emissions combustion and gasification* ; Woodhead Publishing Series in Energy; 59
- [54] Schöny,G.; Zehetner, E.; Fuchs, J.; Pröll, T.; Sprachmann, G.; Hofbauer, H.; (2016) *Design of a bench scale unit for continuous CO₂ capture via temperature swing adsorption- Fluid-dynamic feasibility study* .Chemical Engineering Research and Design 106, pp. 155-167
- [55] Sing, K. S. W.; Everett, D. H.; Haul, R. A. W.; Moscou, L.; Pierotti, R. A.; Roquérol, J.; Siemieniowska, T.; (1985). *Reporting physisorption data for gas/solid systems with special reference to the determination of surface area and porosity*. IUPAC, Pure & Appl. Chem. Vol. 57 No. 4, pp. 603-619.

- [56] <https://climate.nasa.gov/news/916/for-first-time-earths-single-day-co2-tops-400-ppm/>
- [57] Suzuki, M. (1990). *Adsorption Engineering* . pages 35- 37.
- [58] T. J. Fitzgerald, S. D. Crane, in: *Proc. of 5th Int. Conf. on Fluidized Bed Combustion*, volume III, Atlanta, GA, USA, 1980, pp. 815–820.
- [59] T.B. Anderson, R. Jackson, *Industrial and Engineering Chemistry Fundamentals* 6 (1967) pp. 527–539.
- [60] V.V. Kelkar, K.M. Ng, *AIChE Journal* 48 (2002) 1498–1518
- [61] Wang, M.; Stephenson, L. P.; Sidders, J.; Ramshaw, C.; and Yeung, H. (2011). " *Post-combustion CO₂ Capture with Chemical Absorption: A State-of-the art Review* " . *Chemical Engineering Research and Design*, 8(9), pp. 1609 1624.
- [62] Wen, C. Y., Yu, Y. H., (1966). *A generalized method for predicting the minimum fluidization velocity*. *AIChE Journal* 12 (3), 610-612.
- [63] Werther, J.; (2007). *Fluidized-Bed Reactors*. Ullmann's Encyclopedia of Industrial Chemistry
- [64] Winkler, F; (1922). *Verfahren zum Herstellen von Wassergas*. Deutsches Reich, Patent DE437970: Angemeldet am 28. September 1922, veröffentlicht am 2. Dezember 1926, Anmelder: IG Farbenindustrie AG, Erfinder: Fritz Winkler.
- [65] Yang, W.C; (2003). "*Handbook of Fluidization and Fluid-particle Systems*". Marcel Dekker Inc.
- [66] <http://nsidc.org/arcticseaicenews/2016/12/arctic-and-antarctic-at-record-low-levels/>
- [67] Schöny,G.; Dietrich F.; Fuchs, J.; Pröll, T.; Hofbauer, H.; (2016) *A multi-stage fluidized bed system for continuous CO₂ capture by means of temperature swing adsorption-First result from bench scale experiments*. *Powder Technology*

Appendix

1. Interpolation of the Solid circulation Rate

Interpolation						$y = 2,2873 * f(\text{Hz})$	
f (Hz)	SCR (kg/h)	f (Hz)	SCR (kg/h)	f (Hz)	SCR (kg/h)	f (Hz)	SCR (kg/h)
10	22,87	33	75,48	56	128,09	79	180,70
11	25,16	34	77,77	57	130,38	80	182,98
12	27,45	35	80,06	58	132,66	81	185,27
13	29,73	36	82,34	59	134,95	82	187,56
14	32,02	37	84,63	60	137,24	83	189,85
15	34,31	38	86,92	61	139,53	84	192,13
16	36,60	39	89,20	62	141,81	85	194,42
17	38,88	40	91,49	63	144,10	86	196,71
18	41,17	41	93,78	64	146,39	87	199,00
19	43,46	42	96,07	65	148,67	88	201,28
20	45,75	43	98,35	66	150,96	89	203,57
21	48,03	44	100,64	67	153,25	90	205,86
22	50,32	45	102,93	68	155,54	91	208,14
23	52,61	46	105,22	69	157,82	92	210,43
24	54,90	47	107,50	70	160,11	93	212,72
25	57,18	48	109,79	71	162,40	94	215,01
26	59,47	49	112,08	72	164,69	95	217,29
27	61,76	50	114,37	73	166,97	96	219,58
28	64,04	51	116,65	74	169,26	97	221,87
29	66,33	52	118,94	75	171,55	98	224,16
30	68,62	53	121,23	76	173,83	99	226,44
31	70,91	54	123,51	77	176,12	100	228,73
32	73,19	55	125,80	78	178,41		

2. Measured values - Umf

a. Quartz as received

Volume flow $\text{Nm}^3/\text{h}(\text{Nm}^3/\text{h})$	dp- distributor (mbar)	volume flow (Nm^3/h)	velocity (m/s)	dp-total (mbar)	dp-adj. (mbar) as rece
0,40	2,03	0,40	0,05774	15,75	13,72
0,38	1,84	0,38	0,05485	15,45	13,61
0,36	1,67	0,36	0,05196	15,15	13,48
0,34	1,50	0,34	0,04908	14,85	13,35
0,32	1,34	0,32	0,04619	14,60	13,26
0,30	1,19	0,30	0,04330	14,35	13,16
0,28	1,06	0,28	0,04042	14,10	13,04
0,26	0,92	0,26	0,03753	13,80	12,88
0,24	0,80	0,24	0,03464	13,70	12,90
0,22	0,68	0,22	0,03176	13,50	12,82
0,20	0,57	0,20	0,02887	13,25	12,68
0,18	0,48	0,18	0,02598	12,90	12,42

0,16	0,39	0,16	0,02309	11,70	11,31
0,14	0,31	0,14	0,02021	10,40	10,09
0,12	0,23	0,12	0,01732	9,20	8,97
0,10	0,17	0,10	0,01443	7,65	7,48
0,08	0,12	0,08	0,01155	6,20	6,08
0,06	0,07	0,06	0,00866	4,60	4,53

b. Quartz used

volme flow (Nm ³ /h)	dp- distributor (mbar)	volume flow (Nm ³ /h)	velocity (m/s)	dp-total (mbar)	dp-adj. (mbar) used
0,40	2,03	0,40	0,05774	13,10	11,07
0,38	1,84	0,38	0,05485	12,90	11,06
0,36	1,67	0,36	0,05196	12,60	10,93
0,34	1,50	0,34	0,04908	12,35	10,85
0,32	1,34	0,32	0,04619	12,10	10,76
0,30	1,19	0,30	0,04330	11,80	10,61
0,28	1,06	0,28	0,04042	11,60	10,54
0,26	0,92	0,26	0,03753	11,10	10,18
0,24	0,80	0,24	0,03464	10,95	10,15
0,22	0,68	0,22	0,03176	10,90	10,22
0,20	0,57	0,20	0,02887	10,60	10,03
0,18	0,48	0,18	0,02598	10,55	10,07
0,16	0,39	0,16	0,02309	10,35	9,96
0,14	0,31	0,14	0,02021	10,30	9,99
0,12	0,23	0,12	0,01732	9,10	8,87
0,10	0,17	0,10	0,01443	7,50	7,33
0,08	0,12	0,08	0,01155	6,85	6,73
0,06	0,07	0,06	0,00866	5,05	4,98



MASTERSIZER 2000

Analyse Report

Probenname: Glasperlen as reviewed **SOP:** Glasperlen Microrinne **Gemessen:** Tuesday, February 23, 2016 10:33:18 AM
Probenherkunft: Factory **Operator:** tlamingner **Berechnet:** Tuesday, February 23, 2016 10:33:18 AM
Probenreferenz: **Datenursprung:** Gemittelt

Probenmaterial: Glass beads (typical) **Dispergiermodul:** Scirocco 2000 (B) **Abschattung:** 0.59 %
Partikel RI: 1.520 **Absorption:** 0 **Analysemodell:** Monomodale Verteilung (fein)
Dispergierfluid: **Meßbereich:** 0.020 to 2000.0... um **Fit(gewichtet):** 0.986 %
Fluid RI: 1.000 **Emulatio...:** Aus

Konzentration: 0.0031 %Vol **Vol. Mittelwert D[4,3]:** 160.145 um **Spezifische Oberfläche:** 0.0164 m²/g
Breite : 0.567 **Gleichförmigkeit:** 0.184 **D[3,2]:** 149.646 um

Verteilungsart: Volumen

d(0.1): 119.064 um

d(0.5): 157.423 um

d(0.9): 208.255 um



Größen	Häufigkeit (%)	Größen	Häufigkeit (%)	Größen	Häufigkeit (%)						
0.020	0.00	0.142	0.00	1.002	0.00	7.096	0.00	50.238	0.08	355.656	0.00
0.022	0.00	0.159	0.00	1.125	0.00	7.962	0.00	56.368	0.06	399.052	0.00
0.025	0.00	0.178	0.00	1.262	0.00	8.934	0.00	63.246	0.06	447.744	0.00
0.028	0.00	0.200	0.00	1.416	0.00	10.024	0.00	70.963	0.09	502.377	0.00
0.032	0.00	0.224	0.00	1.589	0.00	11.247	0.00	79.621	0.07	563.677	0.00
0.036	0.00	0.252	0.00	1.783	0.00	12.619	0.00	89.337	0.00	632.456	0.00
0.040	0.00	0.283	0.00	2.000	0.00	14.159	0.00	100.237	0.95	709.627	0.00
0.045	0.00	0.317	0.00	2.244	0.00	15.887	0.00	112.468	4.06	796.214	0.00
0.050	0.00	0.356	0.00	2.518	0.00	17.825	0.00	126.191	9.82	893.367	0.00
0.056	0.00	0.399	0.00	2.825	0.00	20.000	0.00	141.589	16.22	1002.374	0.00
0.063	0.00	0.448	0.00	3.170	0.00	22.440	0.00	158.866	19.32	1124.683	0.00
0.071	0.00	0.502	0.00	3.557	0.00	25.179	0.00	178.250	19.36	1261.915	0.00
0.080	0.00	0.564	0.00	3.991	0.00	28.251	0.00	200.000	15.53	1415.882	0.00
0.089	0.00	0.632	0.00	4.477	0.00	31.698	0.10	224.404	8.53	1568.656	0.00
0.100	0.00	0.710	0.00	5.024	0.00	35.586	0.20	251.785	4.52	1762.502	0.00
0.112	0.00	0.796	0.00	5.637	0.00	39.905	0.21	282.508	0.46	2000.000	0.00
0.126	0.00	0.893	0.00	6.325	0.00	44.774	0.21	316.979	0.00		
0.142	0.00	1.002	0.00	7.096	0.00	50.238	0.12	355.656	0.00		

Kommentar: Mittelwert



MASTERSIZER 2000

Analyse Report

Probenname: Gasperlen used **SOP Name:** Gasperlen Microrinne **Gemessen:** Tuesday, February 23, 2016 10:39:35 AM
Probenherkunft: Factory **Operator:** flaminger **Berechnet:** Tuesday, February 23, 2016 10:39:35 AM
Probenreferenz: **Datenursprung:** Gemittelt

Probenmaterial: Glass beads (typical) **Dispergiertmodul:** Scirocco 2000 (B) **Abschattung:** 0.58 %
Partikel RI: 1.520 **Absorption:** 0 **Analysemodell:** Monomodale Verteilung (fein)
Dispergiertfluid: **Meßbereich:** 0.020 to 2000.000 µm **Fit(gewichtet):** 0.704 %
Fluid RI: 1.000 **Emulation:** Aus

Konzentration: 0.0025 %Vol **Vol. Mittelwert D[4,3]:** 145.035 µm **Spezifische Oberfläche:** 0.0188 m²/g
Breite : 0.716 **Gleichförmigkeit:** 0.226 **D[3,2]:** 130.488 µm
Verteilungsart: Volumen

d(0.1): 97.556 µm **d(0.5):** 141.952 µm **d(0.9):** 199.220 µm



Größen-	Häufigkeit (%)	Größen-	Häufigkeit (%)								
0.020	0.00	0.142	0.00	1.002	0.00	7.096	0.00	50.238	0.54	355.656	0.00
0.022	0.00	0.159	0.00	1.125	0.00	7.962	0.00	56.368	0.46	399.052	0.00
0.025	0.00	0.178	0.00	1.262	0.00	8.934	0.00	63.246	0.40	447.744	0.00
0.028	0.00	0.200	0.00	1.416	0.00	10.024	0.00	70.963	0.79	502.377	0.00
0.032	0.00	0.224	0.00	1.589	0.00	11.247	0.00	79.621	0.79	563.677	0.00
0.036	0.00	0.252	0.00	1.783	0.00	12.619	0.00	89.337	2.80	632.456	0.00
0.040	0.00	0.283	0.00	2.000	0.00	14.159	0.00	100.237	4.94	709.627	0.00
0.045	0.00	0.317	0.00	2.244	0.00	15.887	0.00	112.468	9.44	796.214	0.00
0.050	0.00	0.356	0.00	2.518	0.00	17.825	0.00	126.191	13.16	893.307	0.00
0.056	0.00	0.399	0.00	2.825	0.00	20.000	0.00	141.589	15.57	1002.374	0.00
0.063	0.00	0.448	0.00	3.170	0.00	22.440	0.02	158.800	15.91	1124.683	0.00
0.071	0.00	0.502	0.00	3.557	0.00	25.179	0.07	178.250	14.09	1261.915	0.00
0.080	0.00	0.564	0.00	3.991	0.00	28.251	0.08	200.000	10.65	1415.862	0.00
0.089	0.00	0.632	0.00	4.477	0.00	31.698	0.11	224.404	5.86	1588.656	0.00
0.100	0.00	0.710	0.00	5.024	0.00	35.566	0.16	251.785	3.29	1782.502	0.00
0.112	0.00	0.796	0.00	5.637	0.00	39.905	0.24	282.508	0.57	2000.000	0.00
0.126	0.00	0.893	0.00	6.325	0.00	44.774	0.37	316.979	0.00		
0.142	0.00	1.002	0.00	7.096	0.00	50.238	0.51	355.656	0.00		

Kommentar:

Mittelwert

